Blind Estimation of Sonar Images from Diverse Speckle-Scene Models

Thesis submitted to
COCHIN UNIVERSITY OF SCIENCE AND TECHNOLOGY
in partial fulfillment of the requirements
for the award of the degree of
DOCTOR OF PHILOSOPHY

RITHU JAMES

Under the Guidance of
Prof.(Dr.) Supriya M.H.

Department of Electronics
Faculty of Technology
Cochin University of Science and Technology
Cochin-682022, India

August 2017

Blind Estimation of Sonar Images from Diverse Speckle-Scene Models

Ph.D thesis in the field of Signal Processing

Author:
Rithu James
ASPIRE
Department of Electronics
Cochin University of Science and Technology
Cochin-682022, India.
E-mail: *rithujames@gmail.com*

Supervisor:
Dr. Supriya M.H.
Professor & Head
Department of Electronics
Cochin University of Science and Technology
Cochin-682022, India.
E-mail: *supriyadoe@gmail.com*

Dedicated to.....

My Husband & ***Son***

COCHIN UNIVERSITY OF SCIENCE AND TECHNOLOGY
DEPARTMENT OF ELCTRONICS
Thrikkakara, Cochin-682022

Certificate

Certified that this thesis entitled ***Blind Estimation of Sonar Images from Diverse Speckle-Scene Models*** is a bonafide record of the research work carried by Ms.Rithu James under my supervision in the ASPIRE, Department of Electronics, Cochin University of Science and Technology. The results presented in this thesis or part of it has not been presented for the award of any other degree.

Prof.(Dr.) Supriya M.H.
Department of Electronics
Cochin University of Science and Technology
Cochin, India-682022

Declaration

I hereby declare that the work presented in the thesis entitled ***Blind Estimation of Sonar Images from Diverse Speckle-Scene Models*** is a bonafide record of the research work done by me under the supervision of Prof.(Dr.) Supriya M.H., Department of Electronics, Cochin University of Science and Technology, India and that no part thereof has been presented for the award of any other degree.

Rithu James
Department of Electronics
Cochin University of Science and Technology
Cochin, India-682022

COCHIN UNIVERSITY OF SCIENCE AND TECHNOLOGY
DEPARTMENT OF ELCTRONICS
Thrikkakara, Cochin-682022

Certificate

This is to certify that this thesis entitled ***Blind Estimation of Sonar Images from Diverse Speckle-Scene Models*** has been modified to effect all the relevant corrections suggested by the Doctoral Committee and the audience during the Pre-synopsis Seminar.

Prof.(Dr.) Supriya M.H.
Department of Electronics
Cochin University of Science and Technology
Cochin, India-682022

Acknowledgments

First of all I thank the **God** Almighty for His grace and mercy that enabled me in the completion of the thesis work.

I take this opportunity to express my sincere gratitude to my guide **Dr.Supriya M.H.** for her guidance, encouragement and support during the course of this work.

My sincere thanks to the Doctoral Committee members for their suggestions and support. I am also thankful to the Chairman and members of the Departmental Research Committee for their support.

I thank from the bottom of my heart **Dr.C.K.Aanandan**, **Dr.P.Mohanan**, **Dr.P.R.S.Pillai**, **Dr.K. Vasudevan**, **Dr. Tessamma Thomas** and **Dr. James Kurian** for their support and goodwill through all my years in the Department. I thank all the other teaching faculty of Department of Electronics, CUSAT for their support.

I take this opportunity to thank Suraj Kamal, Sherin B.M, Alex Raj, Satheesh Chandran, Mohankumar K, Prasanth P.P, Shameer K. Muhammed, Sabna N and all my fellow research scholars of the Department of Electronics for all their support.

I thank all the non-teaching staff and technical staff of the Department of Electronics.

I thank all all my RSET family members for their support.

I remember my husband **Bijesh Paul**, my son **Paul**, parents, teachers and all family members and friends for their prayers and moral support.

Rithu James

Abstract

Sonar utilizes underwater sound propagation to explore the presence, location or nature of artifacts in the sea in order to navigate, communicate, or detect other vessels or targets of interest. Acoustics is the best known modality to investigate the water column and sea bed efficiently and accurately. Sonar systems are used for the generation of acoustic images and sea bottom profiling. The sonar image is a low frequency image with less details and hard to be recognized. Owing to the complexity of the channel and the manners of the sound spreading, the sonar images are not easily interpreted by inexpert human operators, and applications like automatic object detection and recognition can turn out to be rather difficult compared to the optical image. There are many disadvantages to a purely visual interpretation of such images as it is subjective, qualitative and time consuming. Due to the imaging sonar limitations, straight forward image processing is not enough to detect the obstacles and computer-assisted information brings an objective and quantitative assessment to help the interpreter. Computer-assisted interpretation of sonar images aims at enhancing the visibility of objects, relations between objects and in some cases, it can also bring information that was invisible to the human eye for physiological reasons like texture-oriented analysis. In the study of acoustic imaging, the need arises to classify objects located on or near the sea bottom. The classification process can be related to various areas of interest, such as sea-bottom profiling, mine hunting, under sea navigation and target tracking.

Images formed with coherent energy, such as sonar images, suffer from speckle noise, which reduces spatial resolution by giving a variance to the intensity of each pixel. While Gaussian noise can be modeled by random values added to an image, speckle noise can be modeled by random values multiplied by pixel values and hence called as multiplicative noise. Because speckle is difficult to distinguish from the real signals at the limit of resolution of the sonar, it proves hard to remove without

affecting significantly the image. Prior to attempting to segmentation and feature extraction in the image, the speckle noise must be removed.

The thesis entitled 'Blind Estimation of Sonar Images from Diverse Speckle-Scene Models' proposes different speckle-scene models for the sonar image estimation and analyses the models in both the transform domain and spatial domain. The report presents objectives of the research work, review of past works reported in open literature related to various techniques used for denoising of sonar images for computer assisted interpretations. Among the different models investigated, the work considers two different speckle-scene models *vis-a-vis* the signal independent additive noise model and the multiplicative noise model. For the signal-independent additive model, in the transform domain a mutiresolution analysis method and the sparsity of the natural sonar images are exploited for the denoising and in the spatial domain a kalman filter based estimation method is used to denoise the side scan sonar image. For the mutiplicative noise model, in the transform domain a mixed noise removal based on probabilistic patch based processing is employed and in the spatial domain, the fractional integral mask based method and an unscented kalman filter based estimation method is adopted. The image enhancement done on a despeckled sonar image emphasizes the importance of despeckling before further processing. The non-refernce metric value comparisons and visual comparisons highlights the superior performance of the different proposed methods compared with the existing ones.

Contents

List of Figures

List of Tables

Abbreviations

AUV	Autonomous Underwater Vehicles
CC	Correlation Coefficient
COV	Coefficient of Variance
DWT	Discrete Wavelet Transform
EKF	Extended Kalman filter
ENL	Equivalent Number of Look
FIM	Fractional Integral Masks
GGD	Generalized Gaussian Distribution
LMMSE	Least Mean Square
MAP	Maximum A-Posteriori
MMSE	Minimum Mean Square Error
MSE	Mean Square Error
NL	Non Local
PCA	Principal Component Analysis
PDF	Probability Density Function
PSNR	Peak SignalâtoâNoise Ratio
ROI	Region of Interest
SMPI	Speckle Suppression and Mean Preservation Index
SNR	Signal-To-Noise Ratio
SRAD	Speckle Reducing Anisotropic Diffusion
SSI	Speckle Suppression Index
SSS	Side Scan Sonar
SVD	Singular Value Decomposition
TV	Total Variation
UDWT	Undecimated Wavelet Transform
UKF	Unscented Kalman Filter
UT	Unscented Transformation
WMLE	Weighted Maximum Likelihood Estimation
WT	Wavelet Transform

Chapter 1

Introduction

The study of underwater images, has gained considerable significance due to its strategic as well as commercial importance. Many regions of the ocean and the seafloor remain unexplored due to the limitations of underwater imaging. Being a turbid medium, water scatters light leading to absorption by suspended sediments in it. This severe attenuation as well as limitation in the distance of propagation makes light an unsuitable entity in the underwater studies leading to the use of SONAR for underwater imaging.

This chapter deals with the area of research work undertaken, and the reason for and significance of the work. It elaborates the image characteristics and the types of noise affecting sonar images, as well as the characteristics of typical sonar images affected with noise. The applications of sonar images, with an emphasis on the need for denoising, are detailed. The chapter concludes with details of the organization of the present thesis.

1.1 Sonar Imaging

The term "SONAR" is an acronym for "SOund NAvigation and Ranging". SONAR uses sound propagation underwater, to navigate, communicate, and detect other vessels or targets of interest. The operation of a sonar system is based on the propagation of sound waves between a target and a receiver underwater. They are classified into passive sonars or active sonars. Passive sonars record the sounds emitted by other underwater objects. Active sonars, the system of choice for sonar imaging, can be modeled as an acoustic plane wave (with frequency typically in the $100kHz$ to

$2MHz$ range) emanating from a point source. SONAR then listens for the echoes of these emitted sound signals returned by remote underwater objects. Electro-acoustic transducers are used for the transmission and reception of these acoustic waves. As the plane wave travels through a medium such as the ocean, many factors like temperature, depth, pressure, salinity and surface weather conditions influence it. As it strikes the target, part of the energy is reflected back towards the sonar, whereas the remaining energy passes through the target and strikes the seabed. Depending on the nature of the seabed, part of the incident energy is reflected, and the remaining energy is transmitted into the bottom sediment layer. The energy transmitted within the bottom sediment layer further undergoes transmission and reflection, depending on the characteristic impedance of the local material present. The local characteristic impedance varies depending on whether the bottom is composed of mud, mud and sand, or sand and rock.

Today, sonar systems provide near-photographic high-resolution images of underwater areas, even in water with zero visibility to the human eye. The characterization of these high-resolution sonar images is important for a number of practical applications such as marine geology, commercial fishing, offshore oil prospecting, and drilling.

1.2 Sonar Image Characteristics

In sonar images, there are fewer gray degree classes in the object, because of the complexity of the underwater environment. The intensity is related to the changes in acoustic pressure, as measured by the hydrophone arrays on the sonar system, and can easily span several orders of magnitude and hence a logarithmic scale, in decibels, is used.

The properties of acoustic transmission, and the subsequent method of generation of sonar images, produces images that are of poor visual quality. These do not provide a direct representation of the seabed. As a result of the relatively low velocity of propagation, the time taken for the acoustic signal to travel from the source to the seabed and return is significant with respect to the capture time of the signal; the sonar therefore displays the returned signal as echo intensity against time. The images are further distorted because of this time-based display and the motion of the transducer during the capture process. The actual resolution of features on the seabed determinable from the images is dependent on the sonar operating

characteristics, in particular the frequency, pulse length and directivity. In addition, the images are not unique as completely different features on the seabed can appear similar on the sonar record.

Three types of regions [1] usually have to be identified in high-resolution sonar images such as highlight, shadow, and seafloor reverberation as shown in Fig.1.1. Due to the relatively high density of objects like rocks, or man-made items, the return intensity from the front surface point A is much stronger than the background. There are also multiple returns from points just in front of the object. The sonar shadow points $B - C$ after the object due to the majority of the energy being reflected is a very useful marker for the object.

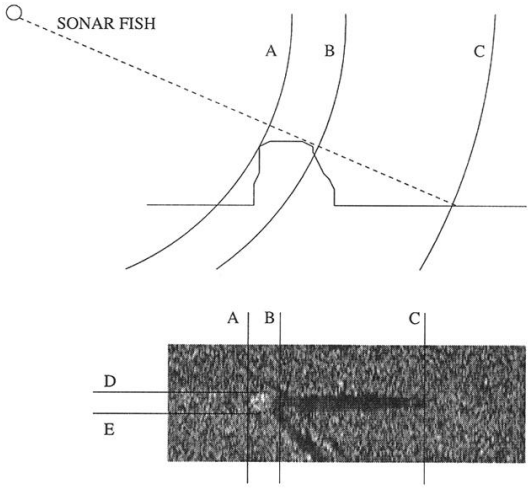

Fig. 1.1: The formation of an object in side scan sonar images

The highlight area originates from reflection of an acoustic wave from the object, whereas the shadow zone is due to a lack of acoustic reverberation behind the object. The region of interest is usually the highlight or the shadow area because the highlight features are generally less discriminable than the shadow shapes for the classification of objects on the seafloor. The seafloor reverberation region is more difficult to differentiate as it contains a large amount of speckle noise. The gray values associated with some substances, such as rocks, animals, and impurities, are close to those of the highlight and shadow regions.

While sonars allow large portions of the seabed to be scanned at once, the objects of interest in these images are usually very difficult to detect. These objects, camouflaged by the sea floor, are often difficult to notice except for the faint trace

of a characteristic shadow adjacent to a bright highlight region. Additionally sonar images are very sensitive to the grazing angle, which can make the same underwater object appear completely different depending on its surroundings. The factors like texture of the object and characteristics of the medium cause significant differences in patterns within the class.

1.2.1 Speckle Effect on Sonar Images

Images formed with coherent imaging such as laser imaging, radar, and ultrasonic imaging, suffer from high frequency speckle noise. This reduces spatial resolution by giving a variance to the intensity of each pixel. In sonar imaging, the acoustic waves are no longer in phase after interaction with the seafloor, and constructive or destructive interferences may occur, producing anomalously high or low returns.

Speckle is described as one of the more complex image noise models and it is signal-dependent, non-Gaussian, and spatially-dependent. Each speckle image is an image of the scene corrupted by some random phase-error. Speckle-noise appears as a particularly strong multiplicative noise where the variance of a point is identical to its mean. While Gaussian noise can be modeled by random values added to an image, speckle noise can be modeled by random values multiplied by pixel value. Hence, it is also called multiplicative noise.

Despite the large range advantage over the standard vision, sonar imaging suffers from several drawbacks like having lower Signal-to-Noise Ratios (SNR), due to acoustic wave interference, and containing almost homogeneous and textured regions with relatively rare edges [2]. The acoustic waves reflected from the sea-bottom can have greater energy than the ones reflected from the obstacles, leading to false obstacle detection or to undetected ones. The other drawbacks include the limitation of transducer size, resulting in a lower number of pixels, lower resolution, and the range-resolution dependency i.e. using long sound waves results in larger range imaging, but with limitations in detecting small objects.

1.2.2 Sonar Image Heterogeneity

The sonar image despeckling filters can be adjusted to the heterogeneity of sonar images [3]. The rationale is that in true sonar images at least three statistical classes can be recognized: homogeneous, textured, and strong, or persistent, scatterer. The first class is characterized by a spatially constant reflectivity and in this case the

best estimator is a plain average of intensity pixel values in a neighbourhood. Pixels belonging to the third class should be detected and left unprocessed, as they are intrinsically noise-free and are used for calibration, registration, etc. The intermediate class affected with speckle noise can be processed through the desired despeckling filter. In Lopes*et.al.* [4], the coefficient of variation is used to discriminate among the three classes.

1.2.3 Purpose of Noise Removal in Sonar Images

Sonar is a valuable tool for imaging the bottom of the sea to obtain information for detecting and classifying targets or bottom types of interest [5]. Owing to the complexity of the signal channel and the manners of the sound spreading, the characteristics of the sonar image are different from the optical. Sonar image of an object will closely resemble the optical image of the same, but will have less resolution than the optical image.

Some regions on the sonar images are analyzed by the experts by simple observations of such images. This observation process is disturbed by the speckle noise. Speckle reduction filters are very important in the initial phase to increase the detection or classification performances. Such a filter must realize a great speckle reduction in the regions where the reflectivity is constant, while preserving the details in other regions. Also, Speckle removal is a pre-processing step required in applications like segmentation or registration. The use of speckle reduction filters is necessary to optimize image exploitation procedures.

Speckle noise causes a fragmentation of objects, and poor spatial directivity and resolution, which results in blurring effects around objects and hinders the interpretation of the image content. As speckle is difficult to distinguish from the real signals at the limit of resolution of the sonar, it proves hard to remove without significantly affecting the image. Prior to attempting for segmentation and feature extraction in the sonar image, the speckle noise must be removed.

1.2.4 Denoising of Sonar Images

Image restoration is the removal or reduction of degradations that are incurred while the image is being obtained. If a speckle-scene model can be developed for the degradation process, then the inverse process can be applied to the image to restore it back to the original form. The basic idea behind this is the estimation of the

uncorrupted image from the distorted or noisy image, and is also referred to as image "denoising". Denoising methods tend to be problem specific. Selecting the appropriate method plays a major role in getting the desired image.

Denoising is required in sonar images to distinguish different regions by analyzing the image. Two common approaches exist for despeckling of images.

The first approach is to average several images acquired from the same scene, which is called multi-look processing or super-resolution and uses the local statistics computed on several images. In that way the speckle noise will be reduced due to its random nature, while the observed scene will not be degraded. The mean filter averages the speckle in the data but lowers the resolution. Local distributions of gray levels are approximated by Gaussian or gamma statistics. Mean and variance are computed on small moving windows, and pixels with mean and variance too far from the image mean are considered as speckle, and averaged. The results vary from one sensor and one wavelength to another, and no generic despeckling algorithm has yet been found.

The second technique is based on filtering the speckle noise based on a single image using a two-dimensional filter such as standard low-pass and median filters or adaptive ones. The non-linear median filter was chosen since active sonar images suffer from coherent speckle with a negative exponential probability distribution function for the image magnitude. Linear filters change only the speckle size but do not remove the speckle.

1.3 Computer Assisted Interpretation of Sonar Images

Traditionally, the visual interpretation of sonar imagery, a skilled procedure, has been performed by trained interpreters. Urick [6] presents the distinct advantage of using the skill of the interpreter to the limits, often unattainable by computers. Since purely visual interpretation of sonar image is subjective, qualitative, and time consuming, a computer-assisted interpretation technique is the choice today. Computer assisted interpretation include image enhancement, contour-oriented analyses, texture-oriented analyses, data fusion and geographic information systems, neural networks and genetic algorithms, and image compression. It aims at enhancing the visibility of objects, relations between objects, and can also bring information that was invisible to the human eye for physiological reasons. Most importantly, computer-assisted information brings an objective and quantitative assessment to

help the interpreter [7].

The human interpretation, the accuracy of computer-assisted methods, and the effective application of automated computer aided analysis on sonar images are limited by the image degradation due to speckle. Speckle effect often makes feature extraction, analysis, recognition, and quantitative measurements problematic and unreliable on sonar images.

1.3.1 Signal Conditioning

The proliferation of sonar images produced by different equipments: multibeam echosounders, side scan sonar, forward looking imaging sonar [8], and the large number of processing methods, created the necessity for expert systems for assisting the decision making process. The basic functionality of such an expert system is the representation and the analysis of sonar data, organized as a "multilayer" structure defined by its various attributes like bathymetry, image, angles, and raw data from auxiliary sensors. These data can be represented and processed using various techniques either classical signal and/or image processing or techniques specific to sonar.

The goal of an expert system for sonar images is to achieve three main tasks: quality control, data processing and data interpretation. There are two classes of signal processing techniques used in an expert system for sonar images. The first one represents the so-called image conditioning methods. The second class of signal processing methods applied in sonar expert systems is represented by the so called intelligent image processing techniques: segmentation, textures analysis, classification.

For correction or alleviating the recorded sonar data flaws, a number of image processing techniques, such as noise filtering, radiometric corrections, contrast enhancement, deblurring through constrained iterative deconvolution, and navigation corrections in computer mosaics of multiple swaths, have been implemented. Initial signal conditioning include all the instruments and techniques that can improve the signal before the sonar image formation.

The distinct stages in the transformation of raw sonar data into usable images are as in Fig.1.2.

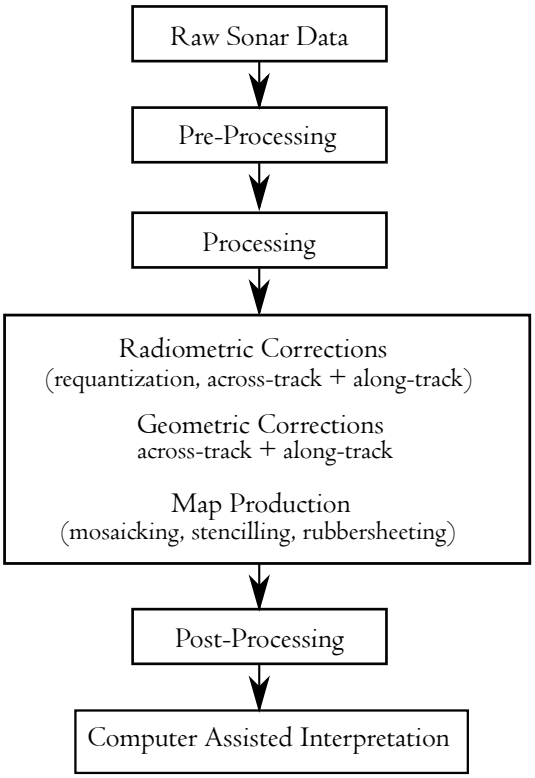

Fig. 1.2: Typical data processing chain

1.3.2 Pre-processing

For the preparation of the raw sonar data for processing, first step is the conversion between the format delivered by the data acquisition system and the format (.xtf format) of the processing software, and further merging these disparate files into a consistent data set.

1.3.2.1 Navigation and Attitude

In order to accurately locate the different sonar echoes on the seabed, knowledge about the location of the sonar (navigation), the direction of imaging (attitude), and the area of the seafloor being ensonified is required. The above said information is provided by the combination of position information (latitude, longitude, altitude above a reference datum), heading, speed, and attitude information. The features on the seafloor can be arbitrarily merged, distorted, or truncated if navigation pre-processing and attitude pre-processing are not done.

The attitude information which consists of the four types of movements heave, roll, pitch, and yaw is shown in Fig.1.3. Heave corresponds to the small-scale variations in the altitude of the sonar platform (in the YZ plane). Roll is the lateral movement of the towfish around its longitudinal axis (in the YZ plane). Pitch is the side-to-side movement of the nose and tail of the towfish around its horizontal axis (in the XZ plane). Yaw is the side-to-side movement of the towfish around its vertical axis (in the XY Plane).

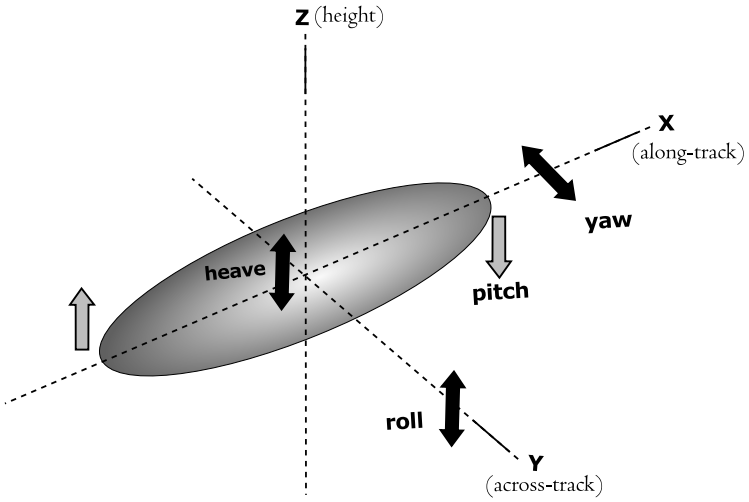

Fig. 1.3: The attitude variations of the surveying platform

1.3.3 Processing

The radiometrically and geometrically correct representation of the seafloor is obtained after the processing step, which transforms raw swath data to usable images or grids. This step includes map production process like mosaicking/stencilling and grid interpolation/rubbersheeting. Radiometric corrections include requantization, across-track corrections, and along-track corrections. Geometric corrections include slant range correction and anamorphosis.

1.3.3.1 The Along-track and Across-track Resolution

Resolution is decided by the acoustic beamwidth, and the pulse length, which define the size of the acoustic footprint. Limits on the range (swath width) are set by the

intensity of the received signal, which must be significantly above the system noise level, together with insonification geometry and time.

One of the factors influencing the across-track resolution of the sonar image is the length of the pulse of acoustical energy emitted by the transducer. The pulse has a physical extent in the water which is determined by the sound speed. By the time the trailing edge of the sonar pulse has left the plate of the transducer the leading edge travels a distance equal to the pulse length in seconds multiplied by the sound speed. The outgoing pulse in the water is thus an expanding wavefront of finite extent. The length of the pulse affects the range resolution and determines the theoretical minimum separation at which two objects on the seabed can be detected. This minimum separation is half the physical length of the pulse. A longer pulse length will encompass the two objects and the returning echo will resemble a single target. A shorter pulse will correctly record the two targets separately. The higher frequency $500kHz$ sonars with typical pulse lengths of $0.0lms$ therefore have a theoretical resolution a factor of ten greater than the medium frequency $100kHz$ systems with pulse lengths of $0.lms$.

The along-track, or transverse, resolution of the sonar is influenced by the finite dimensions of the transducer directivity in the horizontal dimension. The resolution of the images clearly degrades with increasing horizontal beam widths, and this can result in the inability to distinguish two targets which are spaced closely together in the along-track direction. The transverse resolution also degrades with increasing range from the transducer due to the beam spreading. The along-track resolution is a function not only of the horizontal beam width but also of the tow speed and the pulse repetition rate. The latter two factors are operator controllable and their effect on the image can be minimised or at least quantified.

The directivity of the sonar will be a function of the shape and dimensions of the transducer array, as well as the frequency used. The beam pattern needs to be narrow along-track and wide across-track. Sidelobes are generally inevitable, but use of the right frequency, or the right technology, should ensure they are pointing in directions from which reflections are unlikely to be recorded.

1.3.3.2 Mosaicking/Stencilling

The next processing involves placing each pixel in a geographic reference frame to assemble a mosaic of the various survey segments considered. To this end, the

acoustic backscatter data are merged with navigation data (time, latitude, longitude, and heading), in real-time during data acquisition or in post-processing by matching recording times. Pixels are then mapped from the rectangular frame used for filtering to a new rectangular grid of geographic coordinates computed according to standard map projections. The choice of cell size for the geographic grid depends on the spatial resolution of the sonar data available. However, depending on the resolution and scale of the geographic grid, there might be gaps between these remapped pixels. Between adjacent pings, such gaps form polygons that need to be filled before the image is displayed. Subsequent conversion from computer memory to a physical image will alter this resolution depending on the plotting device and its internal algorithm. The processed sonar imagery is composed of picture elements or pixels located by relative coordinates.

In order to produce large-scale classified maps of the seabed, it is necessary to register the individual sonar images [9]. Given the position of the sensor in the world for each side-scan beam, produce a geo-referenced image of the seabed. Georeferencing, also known as geocoding, is the transformation of these relative coordinates into absolute coordinates such as latitude and longitude and is the first step toward the merging of images and the production of maps. The geo-referencing process sometimes stretches or contracts pixels from the individual input images to allow mosaics creation of the correct resolution.

The merging of different images are decomposed into two parts: mosaicking and stencilling [10] as shown in Fig.1.4 and Fig.1.5. When the boundary between two overlapping images is linear, or when overlapping pixel values is averaged, mosaicking merges them into a single data set. Stencilling happens when the border between these images is more complex or when averaging of pixel value is to be avoided, the boundary need to be defined by hand. Stencilling is used particularly when two side scan swaths imaged with opposed directions are overlapping.

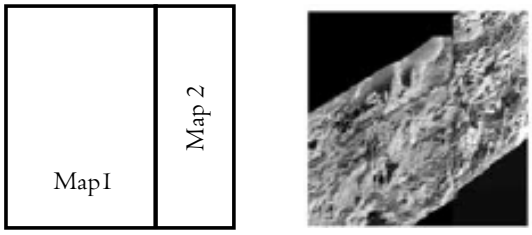

Fig. 1.4: Overlapping images merged by mosaicking

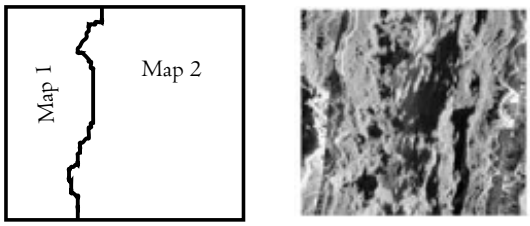

Fig. 1.5: Overlapping images merged by stencilling

1.3.3.3 Interpolation/Rubbersheeting

Simple interpolation schemes average overlapping pixels with the mean or median values. More complex interpolation methods are available such as krigeing, polynomial or spline-fitting, or finite element techniques. The accuracy of interpolation depends on the original spacings and trends of the points. The most elaborate interpolation schemes are used to "tie" an image with inaccurate or imprecise positioning to another precisely located image or series of points. The last process, called rubbersheeting, is most often used to co-register a sonar image to a bathymetric map.

1.3.3.4 Range normalization

Range normalization is a signal amplitude correction designed to conserve the across-track signal dynamic. Signal amplitudes decrease with time or distance from the sonar because of attenuation in the water column. Range normalization using the second order statistics of the signal like mean and standard deviation improve the efficiency of the process across the entire signal range.

A normalization process based on the average signal intensity for each grazing angle [11] is used to correct the sonar beam pattern across the swath. The changes in the attitude of the towfish cause a noise along the track. Assuming that the total back-scattered energy from each ping is similar to that of adjacent pings in the time series, this noise can be eliminated, following which smooth and clear waterfall display can be produced.

1.3.4 Post-processing

Post processing includes the computation of statistics, histogram manipulations, speckle removal, cosmetic operations like contrast enhancement, removal of the survey-scale noise, and multiple reflections.

1.3.4.1 Despeckling for Object Classification

In the study of acoustic imaging, the need arises to classify objects located on or near the sea bottom. The classification process can be related to various areas of interest, such as sea-bottom profiling, mine hunting, under sea navigation and target tracking. Due to the imaging sonar limitations, straight forward image processing is not enough to detect the obstacles, and therefore advanced approaches as in Fig.1.6 are used.

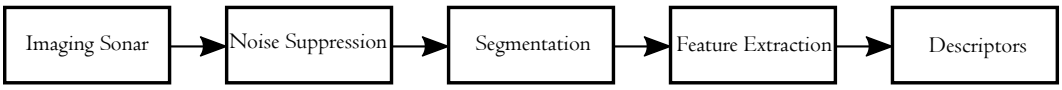

Fig. 1.6: Sonar image processing

Although sonars display many features similar to an optical sensor from a purely image processing point of view, the basics of the physics and formation of the images are crucial for understanding the difficulties found when detecting and classifying mine like objects (MLO's) in sonar images. The classification and detection of MLO's is traditionally carried out by a skilled human operator. This analysis is difficult due to the large variability in the appearance of the sonar images as well as the high levels of noise usually present in the images. With the advances of AUV automatic techniques, computer aided detection/classification (CAD/CAC) of mines, are required to replace a human operator.

The interpretation of the side scan sonar data is performed in two stages [12]. The first stage, pre-processing and target detection, uses an adaptive thresholding algorithm coupled with an adaptive averaging technique to locate objects of interest in the sonar image. The detection strategy incorporates two principal algorithms, adaptive thresholding and shadow analysis on data smoothed by adaptive averaging. The technique presented in [13] is based on the hypothesis that variations in backscatter of sound energy from different ocean bottoms may be described in terms of changes in the texture and tone of sonar images. Measures of texture and tone are derived from the first order statistics of the spatial variation of bottom returns. This textured areas will be affected with speckle noise and will have to be despeckled before shadow analysis.

The second stage, classification, performs a binary classification of whether each detected object is, or is not, a mine. The classification is achieved using an attribute-

based decision tree. The input to this algorithm is a set of objects of interest determined by the detection stage. Classification is performed in four steps: locating the downrange end of the shadow, computing the ratio of object to shadow average intensity, computing the diameter of the object, and classifying based upon these two measured attributes.

Langner *et.al.* [14] explains the required resolution for the detection, classification and identification process of objects in side scan sonar images. It also describes the preprocessing including normalization, height estimation plus slant range correction and georeferencing need before applying different detection algorithms.

The method applied to extract and investigate the power spectral density was developed by Pace *et.al.* [15], [16], [17] for the classification of sediment types from side scan sonar images. Their classification technique involves the definition of features to classify the spectral response of the sediments.

1.4 Computer Assisted Analysis - Applications

The sonar systems generate high resolution images using acoustic transducers, operating at sound or ultrasound frequencies. They exploit techniques developed in the radar field and the capabilities of the high resolution imagery in a great number of applications such as marine geology, commercial fishing, offshore oil prospecting and drilling, cable and pipeline laying and maintenance and underwater warfare. The other applications of imaging sonars include remote sensing and classification of the seabed, inspection of fisheries and channel observation for dredging purposes, as well as object detection.

The marine geology application includes the study of geological structures and detection of sediment distribution. Sonars give scientists the ability to perform large scale geological and biological surveys in search of the most interesting areas of the seabed. During a typical mission, sending sonar images back to the surface ship, rather than simply storing them on the autonomous underwater vehicles (AUV), allows end-users to follow the progress of the survey and redirect the vehicle, if required. This gives rise to the question of efficiently sending data from the sonar back to the surface ship, over a low bandwidth (typically less than 10kbps) acoustic communication channel. In such scenarios, compressing side scan sonar images become an essential task.

The coastal engineering applications include the monitoring of sand transport,

site inspection for gravity structures, pipe lines inspection and detection of man-made objects. There are numerous applications of sonar image in addition to surveying the topographic features of the seafloor like to examine or search for objects on the seabed or in the water column. Such applications include pipeline inspection, where the pipeline on the seabed is examined for underlying spans due to erosion; or mine counter measures applications where channels are surveyed to detect and classify objects on the seabed. The objects in both these cases are man-made and as such have a regular shape.

The hydrographic surveying applications include the detection of wrecks and of other obstructions to navigation, and qualitative topographic information as guidance to completeness of soundings coverage and to depth contouring from sounding lines.

In military applications, due to mission specific time constraints, a computer aided or even autonomous analysis of the huge amount of data is desired. Mines placed on the sea floor are a threat in civil and military shipping. It is suitable for identifying regions of interest in sonar images, in particular the detection of anomalies on the sea floor with focus on proud ground mines.

1.5 Data Base

The techniques presented in the thesis have been developed mostly with the data gathered by the $EDGETECH$ bathymetric side scan sonar system. The methods developed can be applied to different sonar images from different sources. The dynamic range of the recorded data is assumed to span 256 levels, i.e., 8 bits per datum. In its normal mode of operation this sonar is usually towed at about $8-9knots$. It transmits a $1ms$ pulse of $11kHz$ on port and $12kHz$ on starboard, and the seafloor echoes received are displayed to create an image whose width corresponds to a swath about $10km$ wide. The tow speed and ping rate combination decides the along-track spatial sampling interval and the width of this along-trackalong-track filter is set in relation to this. The spatial sampling interval is usually much larger along-track than across-track, decided by the signal bandwidth. In the case of this system, there is an average of $40m$ between pings under normal operating conditions of $8knots$, $10s$ ping rate.

Other short range, high resolution sonars $EGG272$, $Klein422S$ are dual frequency and to improve the across-track resolution, it can be switched from frequen-

cies around $100kHz$ to $500kHz$ in the vicinity of targets or areas of interest. With the pulse repetition rate increased, the along-track resolution is simultaneously upgraded. For imaging larger ranges, lower frequencies and longer pulse lengths are used. The low frequency sonars like $GLORTA$ produce lower resolution images of larger areas of the seabed, with typical resolution cell dimensions of $50m$ by $500m$ and are used to form images of large areas of the seabed or large scale topographic features such as oceanic ridges and sea-mounts.

A shallow-towed side scan sonar system such as $SeaMARC11$, requires the relief fluctuations be at least an order of magnitude smaller than the local water depth. The backscatter images are made of contiguous across-track line segments, with each segment constituting a quasi-continuous element of information. As side scan sonars gather information on a ping by ping basis, to correct the erratic signal amplitude variations between adjacent pings, make a 1-D spectral analysis of each line or ping and then the spectral components are processed in the perpendicular direction along-track. The signals from the vehicle are reconstituted and recorded onto magneto-optical disk on board ship. The pulse repetition period is set to $4s$. With a $1kHz$ digital sampler, 4000 amplitude samples per side scan array are recorded per ping and each sample is stored in two bytes i.e. $16bits$. This arrangement therefore produces over $16kb$ of data every $4s$, equivalent to about $15Mb$ every hour.

1.6 Organization of the Thesis

The thesis is organized as an initial introduction section of the work, the detailed literature review of sonar imaging technology and the existing despeckling techniques, and the methodology adopted for the sonar image estimation based on the different speckle-scene models. The next two chapters dealt with the denoising based on two of the speckle-scene models chosen, the signal-independent additive noise model and the multiplicative noise model. In the next chaper a sonar image enhancement applied on a despeckled sonar image is illustrated. Finally, the thesis concludes by compiling the overall work and their results along with a brief description on the scope for the future study.

1.7 Summary

This chapter presents a state-of-the-art literature in the characteristics of sonar images affected with noise, and the various data processing steps involved which help in sonar data interpretations. A detailed explanation of the types of noise affecting sonar images, the importance of the denoising in the computer assisted interpretations of sonar images, application of sonar images and the organization of the thesis is also briefed.

Chapter 2

Review of Sonar Imaging and Despeckling

This chapter surveys acoustic features of the sea, types of sonar imaging systems and the imaging of the sea by sound. A detailed review of different speckle-scene models and the existing despeckling methods is also briefed.

2.1 Introduction

The cradle of the sonar imaging is the art of imaging the sea by sound. The recent progress in technical sound imaging the ocean is due to the the high speed computer and data storage capability, the highly refined sonar hardware and the precise global positioning satellite (GPS) navigation. There are three fundamental solutions of imaging the sea floor: The first is the high resolution underwater photography which reaches to some tens of meters but is indispensable for certain applications. Second is the satellite radar echo imaging the sea surface which provides a coarse copy of the sea floor beneath through its gravity anomalies. Third is the echo-imaging by sound which is the solution for range and resolution.

2.2 Acoustic Features of the Sea

The sea is an impermeable screen for the signals of the electromagnetic spectrum with visible light as an exception. The path length in pure sea water in the visible wavebands is limited to few tens of meters towards the blue part of the spectrum

with most of the light traveling into water being absorbed and converted into heat. Acoustic waves by contrast [18], can travel over long distances without attenuating too much and can reach all depths in the ocean, from the deepest ($\geq 11km$) to the most common ($\approx 4km$) and the shallowest (a few centimeters). Acoustic echoes give the information about the depth i.e., the range travelled and the type of seabed or obstacle, based on how the signals are being reflected.

Different modeling process need to be considered for light and sound waves that transmit energy through the medium due to several fundamental differences in the two types of energy. The two types of waves differ in the speed of propagation and the wavelength. Considering light as the medium in air and sound as the medium in water, the propagation of light in air approximately five orders of magnitude faster than that of sound underwater. Due to the fast propagation of light, the temporal nature of the light is not perceived by the eye and so the optical images are presented in the spatial domain. On the other hand, the sonar image is displayed in the time domain as it is generated by the differences in the times of return of the acoustic energy. As sound has a much longer wavelength than light, the resolution of optical images is much greater than that of sonar images. It is also affected by the scattering behavior and the relative roughness of surfaces.

The Sound Velocity Profile (SVP) gives the variation of sound speed with depth of the ocean. For the horizontally stratified environment, the sound velocity profile is independent of range. For simplified calculations majority of the acoustic models assume horizontal stratification, due to the weak horizontal variations in sound speed as compared with the vertical changes. Oceans and lakes are nearly horizontally stratified in local regions because of the fluidity of water and the stability of less dense over more dense water. The dimensions of the stratified region may be several hundred kilometers in the open ocean. In the presence of oceanic fronts and eddies, where the environment is range dependent, the horizontal stratification assumption breaks down.

The broad categorization of the ocean is as deep or shallow water areas, where the velocity profiles differ. That part of the ocean lying over the continental shelf where the water depth is less than $200m$ is arbitrarily defined as the shallow water. The typical velocity profile of deep water is illustrated in Fig.2.1, where below the ocean surface the temperature decreases sharply with depth causing the main thermocline. Beneath the thermocline there is a region of constant temperature, which results in an increasing velocity profile, as the speed of sound increases with increasing depth.

A near isothermal water column which results in a linear sound velocity profile with a positive gradient is produced in shallow water by wind induced mixing. Absorption of sound waves occurs when they propagate through the water column and the sediment layers. The absorption results in a loss of energy as the wave propagates and involves the conversion of energy into heat due to the non-ideal nature of the medium. The loss of energy is expressed in terms of the logarithmic absorption coefficient, usually with units of decibels per kilometer and is proportional to the distance traveled in the medium. The three main effects which results in the absorption of acoustic energy by sea water are the shear viscosity, volume viscosity and ionic relaxation.

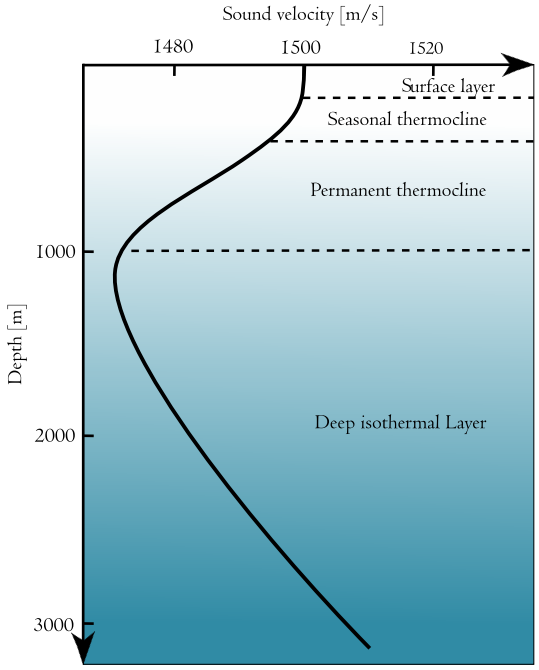

Fig. 2.1: Typical sound speed profile of deep ocean

Under water acoustic transmitters are called projectors and receivers hydrophones. For sonar imaging the narrow band transducers are most suited. At the highest frequencies, the acoustic waves use piezoelectric ceramics or composite ceramics for converting electricity into acoustic pressure for projectors and *vice-versa* for hydrophones. The frequency f of the wave is related to the wavelength λ, the spatial distance between two points in the propagation medium with the same pressure is in eq.2.1,

$$f = \frac{c}{\lambda} \tag{2.1}$$

where c is the velocity of sound in the medium. It ranges between $1,450m/s$ and $1,550m/s$ in sea water, depending on salinity, pressure, and temperature.

Frequencies typically used with sonars range from $1kHz$ to $1MHz$. Comparison of frequencies typically used in under water acoustics with other domains of acoustics is shown in Fig.2.2. For an average sound speed of $1.0m/s$ in sea water, the associated wavelengths range from $1.5m$ at $1kHz$ down to $1.5mm$ at $1MHz$. The wavelength gives the scale of features that can be detected on the seabed.

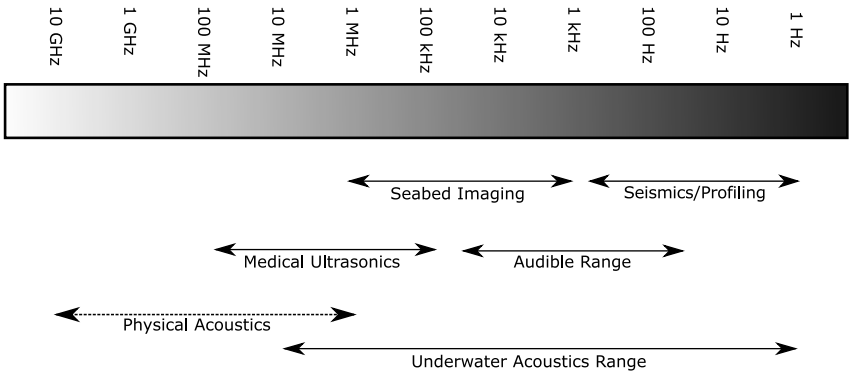

Fig. 2.2: Under water acoustic range

2.3 Types of Sonar Imaging Systems

Attempts are made during the recent years to achieve the best resolution of acoustic imaging under the prevailing conditions at sea with the development of underwater acoustic techniques. The successor to the classical echo sounder is the multi-beam or Fan echo-sounder for imaging the sea floor relief and other objects. For imaging the small scale morphology of the sea floor and the shape of structures, the side scan echo sounder is used. The Sediment Penetrating Sonar for imaging the internal structure of layers and to detect buried objects and the acoustic doppler current profiler for monitoring ocean currents. An Autonomous Underwater Vehicle can be equipped with two types of sonar, a side scan sonar that is mounted on the sides of the AUV and enables sea-floor exploration and bathymetry, and a Forward Looking Sonar that covers a sector in front of the AUV and helps in detection of the obstacles

and path planning.

The three broad categories of the sonar mapping systems are the single-beam echo-sounder, the multi-beam echo-sounder and the side scan sonar system as in Fig.2.3.

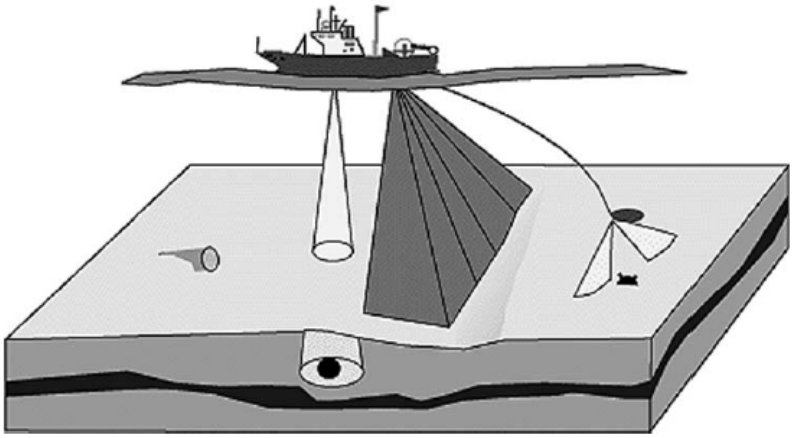

Fig. 2.3: Sonar mapping systems

The single-beam echo-sounder, aims straight below the survey vessel and a wide portion of seabed and sub-seabed is imaged at once. Mostly the information on the seabed immediately below the surveying vessel is provided by such single-beam echo-sounders which look directly beneath the supporting vessel. Depending on the water depth and the local slopes, the footprint on the seabed which is generally large varies in size. The multi-beam echo-sounder, maps a wide swath of seabed across the track of surveying vessel are made of narrower beams. They provide mainly bathymetry by looking on both sides of the vessel and sometimes imagery transmits several beams, covering a wide swath on each side of the ship's track. These beams produced by the transducer arrays are narrower than single beams. The systems using the "split aperture" method is able to resolve targets smaller than the footprint. The side scan sonar imaging at grazing angles are often towed separately and close to the sea bed. When side scan sonars are flown closer to the sea floor, they provide mainly imagery which are more detailed and complex and sometimes bathymetry. Tool of choice for high resolution seabed mapping is the side scan sonar which covers a much larger portion of the seabed away from the surveying vessel, from a few tens of meters to $60km$ or more. The coverage is attained by transmitting one beam on each side, broad in the vertical plane and narrow in the horizontal plane. With

varying frequencies from $6.5kHz$ to $1MHz$, side scan sonars achieve resolutions of $60m$ down to $1cm$.

2.3.1 Sea Floor Mapping with Multi-beam Echo-sounders

Multi-beam echo-sounders are commonly used in mapping of the sea floor. The principle of mapping the sea floor with multi-beam echo-sounders is as in Fig.2.4. In the multi-beam echo-sounder a large number of beams are formed for each ping. The beams are in different directions, spanning a fan cross-track of the vehicle. The range calculated from the time delay to the sea floor is estimated along each beam or direction which gives the relative depth of the sea floor relative to the vehicle. This is again transformed into a map of the seafloor along the fan. When the vehicle moves forward, consecutive pings gives a continuous map of the area surveyed. The map resolution is determined by the 2D beam-width and the range resolution. Typical frequencies used are from $12kHz$ for large scale hull mounted systems with full ocean depth range, to $450kHz$ for short range high resolution mapping. The swath width of a multi-beam echo-sounder is typically 4 to 10 times the sonar altitude.

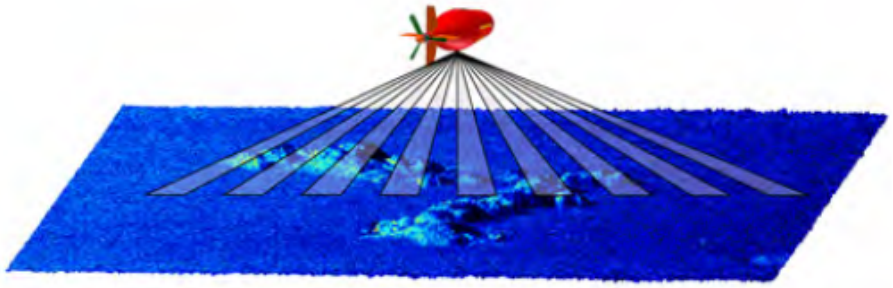

Fig. 2.4: Multi-beam echo-sounder geometry

2.3.2 Sonar Imaging with Side Scan Sonar

Side scan sonar (SSS) is used to produce acoustic images of the seafloor with high resolution. The sonar geometry is sidelooking as illustrated in Fig.2.5. The acoustic image formation principle is by moving the sonar forward and stacking the sonar response from successive pings. The side scan sonar works best when operated fairly close to the seafloor, typically mounted on a towfish, a towed light weight vehicle, or an autonomous underwater vehicle. When operated in shallow waters it can be

mounted on a surface ship hull. The operational frequencies for side scan sonars are typically from $100kHz$ to $1MHz$, with an operational range from $500m$ down to a few tens of metres. The best possible along-track resolution in side scan sonar can be designed by choosing the highest possible frequency for a given range from calculations of absorption.

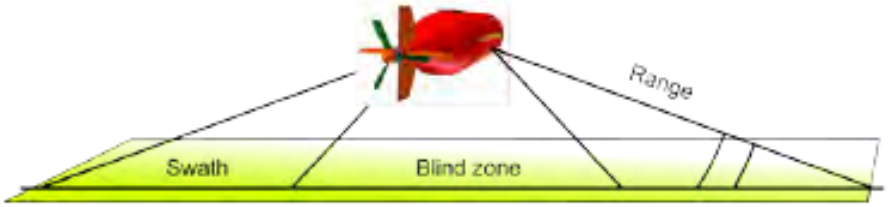

Fig. 2.5: Side scan sonar geometry

A towed active sonar system with the tow vessel, tow cable and tow body is shown in Fig.2.6. The piezo-electric transducers of a side scan sonar mounted onto a separate body which is towed through the water behind the survey vessel provides a more stable platform from which to operate the transducer. This allows the transducer to be decoupled from the motion of the ship. The towed body is called as the towfish, or simply the fish. The transducers when mounted on Remotely Operated Towed Vehicles (ROTV) or Remote Operated Vehicles (ROV) or AUVs, which are "flown" by operators aboard the ship, provides more accurate control of the position and motion of the vehicle, as it is largely divorced from the motion of the survey vessel.

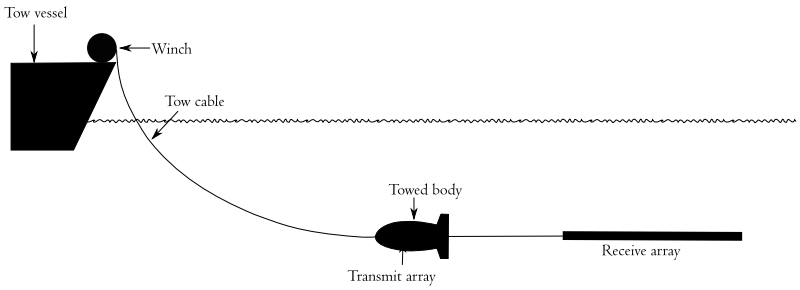

Fig. 2.6: Towed active sonar system

The area covered by a side scan sonar is shown in Fig.2.7. The cross-track coverage is the maximum range of the system, which is related to pulse repetition

interval and the maximum range of the acoustic signals from absorption. The cross-track resolution is the range resolution, given by the pulse length or the bandwidth for coded pulses. The along-track coverage is given by the pulse repetition interval. The along-track resolution is given by the directivity of the sonar antenna and the range.

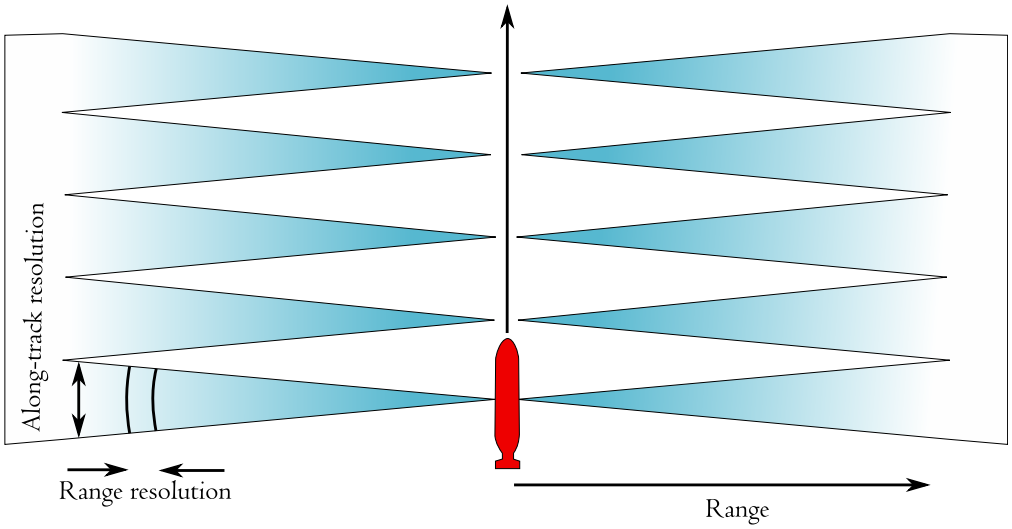

Fig. 2.7: Area coverage and resolution in side scan sonar

Each pulse of acoustic energy emitted causes echoes from an area of the sea bottom perpendicular to the direction of travel of the towfish. The towfish is positioned at an (XYZ) coordinate in space, where Z represents the height of the towfish, the X axis is orientated in the direction of travel of the towfish and Y is the direction perpendicular to the towfish as in Fig.2.8. At this position, the transducer emits a pulse of acoustical energy and the time and intensities of the rays are recorded. The transducer is then moved along the X axis to a new position, to represent the motion of the towfish, and the process is repeated by the transmission of the next pulse, to obtain the next line of the image. The successive lines are then displayed next to one another, as with the real sonar process, to create the image. Each line is displayed as a line of pixels across the image, with the gray scale value of each pixel determined by the intensity returned for that ray, with black representing no returned signal and white representing a high intensity return.

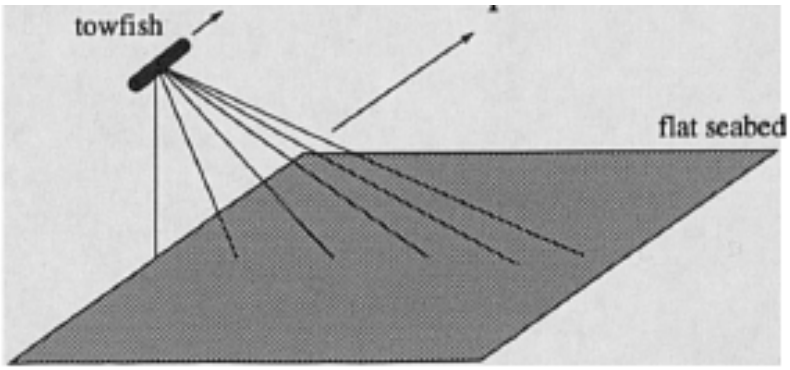

Fig. 2.8: Position of towfish in 3D space

2.3.2.1 SSS Image Formation

For producing the side scan sonar images of the seafloor a series of lines, one per transmission-reception cycle are displayed perpendicularly to the survey track. If the appropriate corrections for refraction and topography have been used, a single line segment represents the echoes received from the seafloor for a given ping as a function of slant range or time, or horizontal range on each side of the track. The formation of an image from a side scan sonar is shown in Fig.2.9.

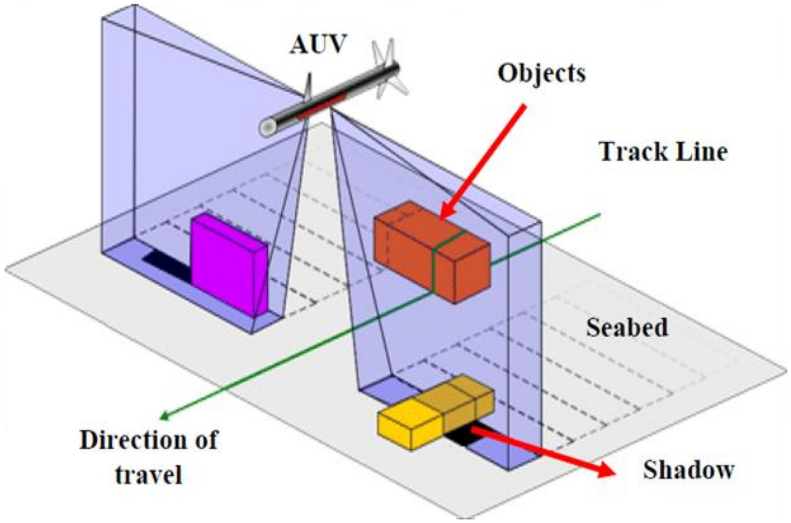

Fig. 2.9: The formation of images from a SSS

The towfish height i.e. the depth of water below a side-scan sonar towfish, is an

important parameter for the collection of side-scan sonar data. The best seafloor coverage can be obtained by having the towfish somewhere near midwater. The sonar towfish too close to the sea-surface gets affected by waves and too close to the seafloor has the chance of striking a prominent object. The reflections from seaweed and other floating objects and reflections from the sea-surface are the interfering echoes. The greatest difficulty is posed by the reflections from the sea-surface since they have a similar appearance to the echo from seafloor below the towfish and when operates in shallow waters these two echoes often intersect. The side scan survey [19]

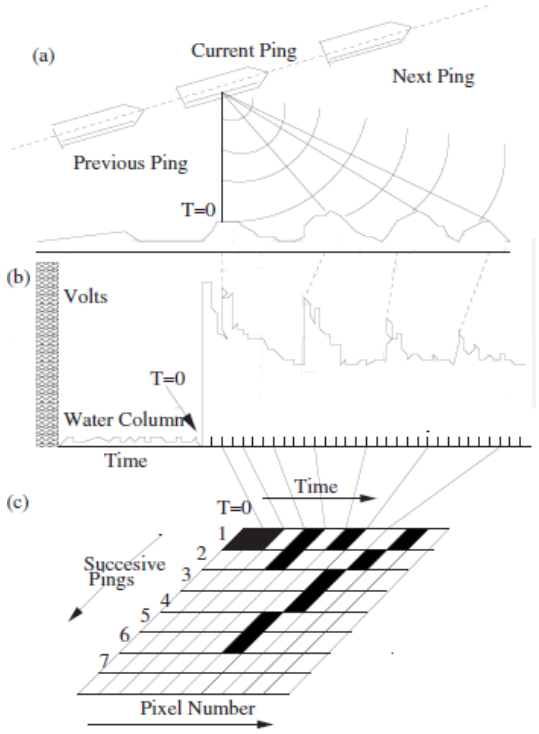

Fig. 2.10: Three-phase diagram showing the process of generating images from a single side-scan sonar ping

provides images which map a visible representation of the strength of acoustic back scattering from the seafloor onto a two-dimensional image medium as illustrated in Fig.2.10 (a) the outgoing pulse from an individual ping is reflected back from the seafloor directly under the fish, and the internal side-scan clock (T=0) is started. (b) The hatched region represents the outgoing pulse, and the low amplitude returns are the time when the pulse is the two-way travel time in the water-column. After the

return of the first bottom bounce, subsequent returns appear as peaks and valleys in the transducer voltage. (c) Peaks and valleys are then integrated and translated into pixels values.

2.3.2.2 SSS Image Interpretation

The acoustic shadow zones appear on the trace as a blank area when the objects which reflect the acoustic energy prevents the energy from ensonifying some part of the seafloor. The position and shape of shadows contain valuable information for the accurate interpretation of the image and shadows are the primary features which provide three dimensional information from the two dimensional sonar image. The shadow zone Fig.2.11 is created by either an object relieved from, or depressed into, the seabed, or by the self shadowing of the seafloor. Depressions create a dark shadow area on the trace succeeded by a lighter area, caused by the reflections from the face of the depression facing back towards the sonar.

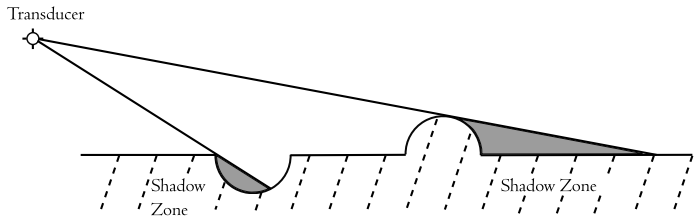

Fig. 2.11: Depressions creating dark shadow zones

2.3.3 Synthetic Aperture sonar

The spatial resolution along-track or azimuth is the fundamental limitation of the traditional side scan sonar. At far ranges, it is usually much worse than the range or cross-track resolution. The array length measured in wavelengths gives the angular resolution. The angular resolution is improved by decreasing the wavelength or increasing the frequency. This limits the practical range, due to the frequency dependent absorption is sea-water. The other approach is to increase the length of the array which requires more hardware, more electronics and more space on the vehicle. But a better approach is to synthesize a larger array by using consecutive pings from the moving sonar which is the principle of Synthetic Aperture Sonar

(SAS) as illustrated in Fig.2.12.

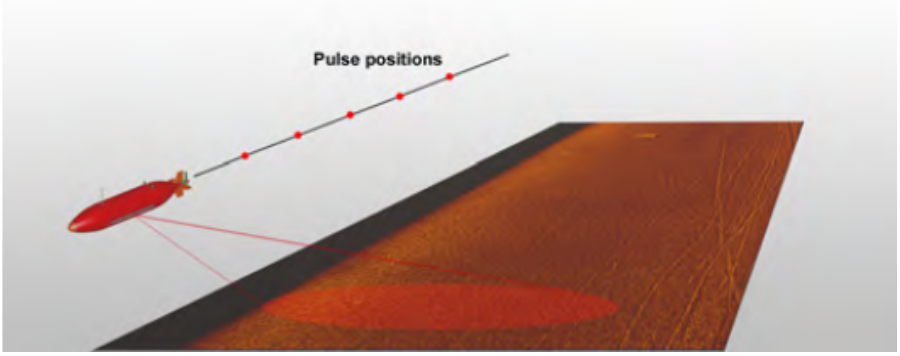

Fig. 2.12: Principle of synthetic aperture sonar

The resolution of a side scan sonar decreases with range away from the sensor which can be increased by using a higher frequency subject to much higher attenuation in water or by using a longer imaging array often far greater than physically feasible. Synthetic Aperture sonar processing could increase the resolution without unduly increasing the size of the transducers. In synthetic aperture technique, whatever the scanning method, the basic idea is to reduce the number of receiver or source elements at the expense of an increased scanning time. However, the scanning rate must be great enough to prevent motion blurring or a loss in signal to noise ratio.

2.4 Imaging the Sea by Sound

Imaging the sea involves transmitting a pulse of acoustical energy into the water medium and receive any returned energy reflected from objects or the seabed. The operation of sonar involves an initial generation of an electrical pulse by the transmitter, with the desired characteristics of frequency, length and energy, by the transmitter. The electrical signal is then applied to the piezo-electric ceramic transducer, which expands and contracts under the application of the electric field to generate an acoustic pulse of oscillating pressure in the water. The seabed or targets reflects and scatters this pulse when the sound waves propagate through the water column. The oscillating pressure vibration converted into an electrical signal by the transducer, which got a portion of the scattered energy reflected back is detected and amplified by the receiver. The control unit regularizes the entire process which synchronizes the operations and controls the timing for the transmission and reception of the

electrical signals. In sonars, it is the time that it takes for the transmitter sonar pulse to travel from the transducer to the target and return is measured and not the depth or distance.

2.4.1 Acoustic Pulses used with Sonars

The ultrasound pulse envelope used by the transducer, insonating a homogeneous medium containing scatterers is approximately Gaussian as in Fig.2.13. If the pulse has a Gaussian shape then so has its spectrum, and for a medium with linear attenuation coefficient this Gaussian shape of the spectrum is maintained while the pulse travels through the medium. A shift of this Gaussian spectrum to lower frequencies occurs while the pulse travels through the medium, because the attenuation increases with the frequency. Upon reception of the reflected signal, the transducer produces an electrical signal that is the algebraic sum of the instantaneous sound pressures originating from the backscattered waves. The depth differences of the scatterers are smaller than the axial size of the resolution volume of the transducer (i.e., the pulse length). The formed pattern is the so-called speckle pattern.

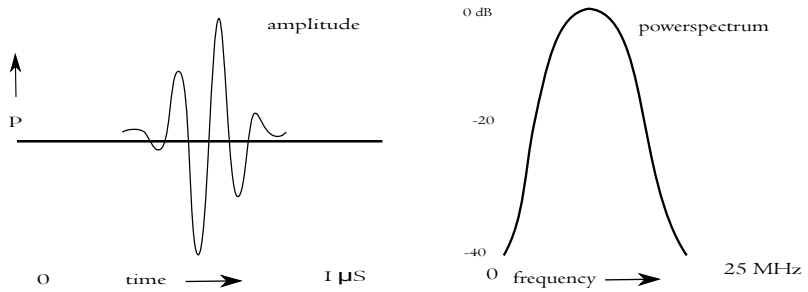

Fig. 2.13: Gaussian shaped sound pulse

Depending on the applications, the type and length of the acoustic pulse uses differs, as it governs the range and resolution of the sonar image. The example pulses like the bursts, chirp and ricker signals used with the sonar are shown in Fig.2.14.

Bursts are narrow band pulses i.e., continuous wave (CW) pulses. They are formed by a sine wave of fixed frequency, transmitted during a limited time T (typically $0.1ms$ to $10ms$). The duration directly impacts on the resolution: two CW pulses of duration T can only be distinguished if they are separated by a time of at least T. After reflection from a target this corresponds to a spatial resolution of $cT/2$ ($0.75m$ for a $1ms$ pulse). Chirp signals are linear swept frequency cosines, also of

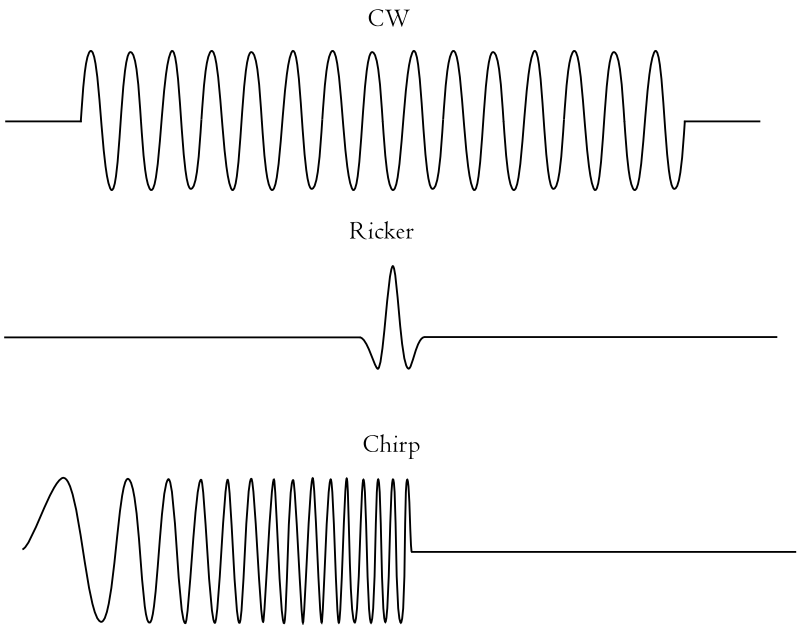

Fig. 2.14: Acoustic pulses used with sonars

limited duration, are used less frequently. They are more advantageous than bursts in noisy environments; for example, to compensate for the very strong attenuation of signal during propagation inside the sea bed, at the detriment of more complex processing. Ricker signals are mostly used for the detection of small targets or for high-resolution sediment profiling. They consists of a single pulse similar to the second derivative of a Gaussian pulse. All side scan sonar surveys are conducted in the far field, defined as given in eq.2.2,

$$R \geq \frac{L^2}{4\lambda} \tag{2.2}$$

Where R is the range. L the length of the array, and λ the wavelength of the signal transmitted.

2.4.2 Frequencies of Acoustic Pulses

The sonar performance is its ability to detect and locate objects of interest on the seabed, to a specific range and at a specific rate. The performance is affected by the generation of the acoustic wave by the sonar transducer, its propagation throughout the water column, its scattering on the seabed, its propagation back to the trans-

ducer, and its subsequent processing. The role of the imaging frequency is extremely important, as it defines both the maximum range achievable and the resolution attainable.

Low frequencies (for e.g., $6.5kHz$) will travel more distances (e.g., $30km$ on each side of the sonar) but give worse resolution (e.g., $60m$ after processing) than high frequency sonars (e.g., $120kHz$) covering a small swath (e.g., $1km$). Taking into account the speed of the imaging platform, lower frequency sonars can be used to map large areas of the seabed in relatively short time, whereas high-frequency sonars will be more suited to detailed studies of smaller areas.

The first maps of the seabed mainly concerned with general areas like the mapping of exclusive economic zones. Covering large areas require large sonar coverage, i.e. with low frequencies, little attenuated over the distances involved. Some sonars prove ideal, yielding swath widths of $60km$ with a resolution of $60m$ after processing.

Higher resolution in sonar images was achieved by using higher frequencies which comes with a cost. The first challenge is technological with the need for faster data acquisition systems and faster processing speeds (high frequency sampling of the backscatter echoes). The second challenge is acoustic: higher frequencies do not propagate as far, and the swath widths achievable decrease quite rapidly. The third challenge is physical: as the frequency decreases, the acoustic wavelength increases, and the resolution of each pixel degrades visibly. The fourth and most important challenge lies in the interpretation of these images, understanding which factor is predominant in the backscattering from the seabed, for each specific wavelength.

2.4.3 Hydrophones and Arrays

Transducers are normally mounted on either side of the towfish for a side scan sonar. It is a sideways looking device and each pulse of acoustic energy emitted causes echoes from the seabed on either side of the towfish from an area of the sea bottom perpendicular to the direction of travel of the towfish. The use of two channels helps to gather information on two channels and allows scanning of a larger area of the seabed at a time. The transducers for each emitted pulse produces a beam, which is narrow in the horizontal direction and wide in the vertical direction. When the transducers are towed along, for each emitted pulse they gather sequential lines of data returned i.e. the returned energy is received from only a thin strip of the seafloor as the horizontal beam is a narrow one.

Acoustic receivers, or hydrophones are organized as arrays and are characterized by their frequency range and directivity pattern. For detecting small range of frequencies which limits the imaging to non-moving targets, or those with no significant doppler shift, narrow-band transducers are used. For detecting a wide range of frequencies broad-band transducers can be used. During data acquisition or processing, those not associated with acoustic backscattering from the seabed can be filtered out. For receiving all the returns from the points that have been imaged and as few returns as possible from points not directly ensonified, the directivity patterns of the arrays should at least match the directivity patterns of the projectors. Due to the internal noise of the receiver and the noise of any attached amplifier electronics called self noise, the receiving arrays record some very small pressure variations. This happens even in the absence of an acoustic signal. The transmitter and receiver need to be accurately synchronized, with an internal or external clock, to ensure the transmitted signal has ample time to be received before the next pulse.

2.4.4 Attenuation

A two way effect will occur on the acoustic waves as they propagate in the water column from the transducer to the target/seabed or from the seabed back to the sonar. Spreading over a large volume will occur as the acoustic wave moves away from the transmitter. After a certain distance in the far field, these waves can be approximated as plane waves. The intensity decreases with a relation $1/R^2$, where R is the distance traveled from the source to the point of measurement which will be the straight distance to the seabed and back for a sonar imaging the seabed.

The acoustic returns becomes weaker and often needs amplifying as the range increases. Acoustic waves follow Snell-Descartes' laws of reflection and refraction at interfaces like the electromagnetic waves and can propagate in the seabed but for shorter distances. The attenuation depends on the type of seabed of orders of magnitude of $100dB/m$ are common at high frequencies.

The dissipation of the acoustic energy viscosity and chemical reactions in the medium are the other factors contributing to the attenuation. The temperature of the water, salinity, and heterogenities like bubbles or suspended sediments in water causes variations in the velocity at which the acoustic waves travel. The influence of sound velocity is more subtle but just as important. The sound speed will vary widely, with values of $1500m/s$ to $2,000m/s$ for some sediments underwater. The

influence of attenuation on sonar imagery is perceived immediately.

The effects of absorption, spreading and scattering decreases the intensity of the returned energy with range. A Time Varying Gain (TVG) is applied to the incoming signal to compensate for the above effects and maintain an even intensity across the image to aid in the correct interpretation as the gain is normally time dependent.

For transmission losses caused by spherical spreading and absorption of sound waves in water, time-varying gain compensation can be used. The resulting images again suffer from various forms of noise or external interferences caused by other acoustic devices operated at the same time. Due to the non straight survey tracks, the attitude of the towfish like roll, pitch and yaw changes with time. The sonar beam patterns are not uniform in the angular sector of interest and their side or back lobes may pick up echoes reflected from the sea surface or may contribute to cross-talk between the two sides. Also the produced sonar images lack contrast.

2.4.5 Sea Surface Reflections

Sonar imagery is affected with the reflections from the sea surface when the swath width is less than the water depth. In shallow-water applications, the wide across-track beam typically interacts with the surface as well as the bottom. The interference from surface scattering or multipath signals that masks the seafloor, adversely affecting sonar images [20] are dependent on the sea state. For a glassy smooth surface, the multipath signals are approximately delayed replicas of the bottom signal. The multipath signals from a rough sea surface produce a grainy effect on the sonar image. If the surface itself is a scatterer because of the presence of boat wake [21], multipath signals gets attenuated and the masking effect is from direct surface scattering. For target detection and bottom classification, image properties like spatial amplitude statistics, shadows, and highlights [22] are used which are obscured or distorted by surface effects. To improve the probability of detection of mines and to avoid any mis-classifications, it is necessary to eliminate surface effects from the sonar image.

2.4.6 Acoustic Array Scattering

The range on both sides of the sonar gives the swath width. Slant range is the distance from the sonar to a point on the seabed as in Fig.2.15. The angle of incidence of the incoming acoustic wave gives information about the scatterring of the acoustic

wave. Specular direction is the direction of maximum energy reflection. Along the scattering angles, distributed along the main reflection angle some energy will be reflected. Loss of some energy in the seabed occur depending on the terrain type. Backscatter i.e. reflection back toward the imaging sonar might happen only for a very small portion. The backscattered energy provides different types of information after the recording of the data. The time offset between the transmission of the initial ping and the reception has a direct dependence on the slant range. For deducing the ground range to the echo, use the sonar's height above the seabed. The Doppler effect i.e. the frequency shift indicates the speed of the target relative to the sensor. The arrival angle of the beam is deduced from the phase shift. The phase difference between neighbouring transducers helps some systems in extracting the bathymetry. Some information about the nature of the point imaged seabed or target can be obtained from the amplitude of the echo.

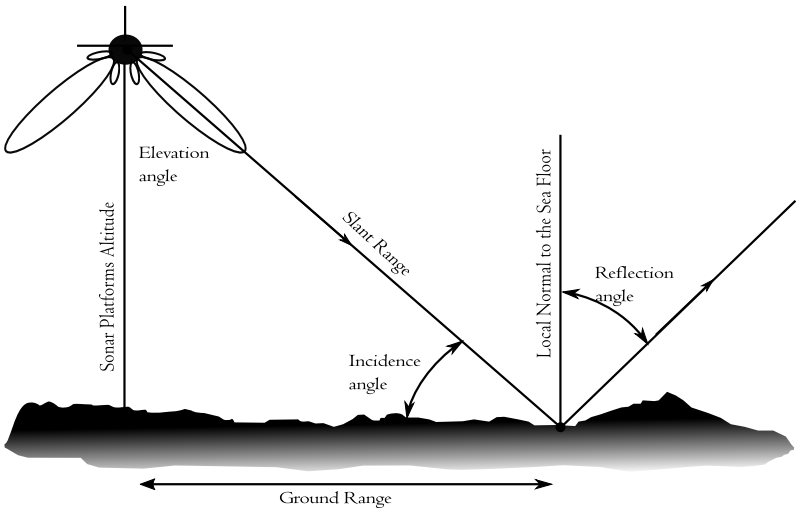

Fig. 2.15: Acoustic scattering

Scatterring will occur mostly along the specular direction and very low backscatter for a surface smooth at the scale of acoustic wavelength. For e.g., $5cm$ for a $30kHz$ frequency. For a rougher surface it is more likely to have small facets facing toward the sonar, this increases the backscatter and scattering in other direction. Gravel patches will appear acoustically brighter than mud patches.

Due to attenuation with distance, the backscattered signals are often weak. Backscatterred signals are very noisy because of the perturbations within the water

column on the way from the sonar to the target and on the way back. Self noise from the transducers themselves or noises from neighbouring instruments like the other acoustic sensors working simultaneously are other additional noises.

2.5 Speckle-Scene Models

Under a statistical signal processing perspective, despeckling filters aim at estimating the noise-free sonar reflectivity from the observed noisy sonar image. Speckle filters' performance depends strongly on the choice of the speckle-scene models used for despeckling. Speckle is not truly a noise in the typical engineering sense, since its texture often carries useful information about the image being viewed. The speckle noise model for sonar images may be approximated as multiplicative.

Sonar is an active acquisition instrument that produces a radiation and captures the signals backscattered from a small area of the imaged scene (resolution cell). The received signal, as output from the in-phase and quadrature channels, is complex. Assuming that the resolution cell contains several scatterers and that none yields a reflected signal much stronger than the others (distributed target), the received signal can be viewed as the incoherent sum of several backscattered waves with amplitudes A_i and phases ϕ_i, as shown in eq.2.3 and Fig. 2.16.

$$A\exp(j\phi) = \sum_i A_i \exp(j\phi_i) \tag{2.3}$$

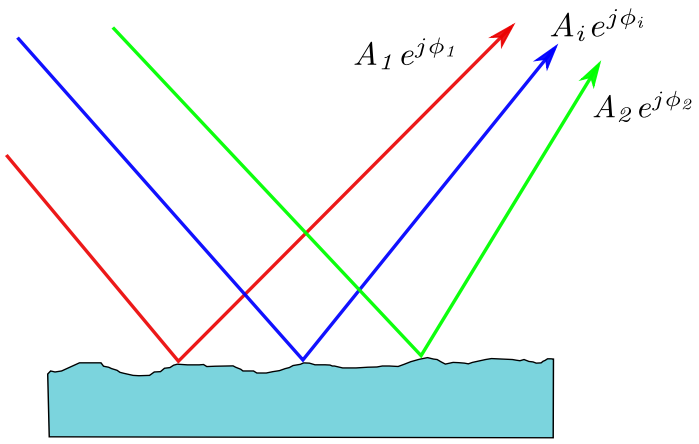

Fig. 2.16: Scattering model for fully developed speckle

Each individual component, cannot be resolved within a resolution cell. If the phases of each path are highly different, they may sum in a constructive or destructive way, then the amplitude of the received signal varies randomly. So, even if the underlying reflectivity field is uniform, it appears as affected by a "granular" noise after the imaging system. For visual inspection and for specific applications that involve visual information retrieval, such as mapping and segmentation, the highly varying nature of the signal may be considered as a disturbance and is commonly denoted as "speckle".

The phases ϕ_i are highly varying since the wavelength is much shorter than the resolution cell size and scatterers distances may be considered as uniformly distributed in $(-\pi, \pi)$ as well as independent of A_i. If the number of scatterers is sufficiently high, the central limit theorem applies [23] and the resulting signal $A \exp j\phi = z_1 + jz_2$ can be seen as a complex signal whose real and imaginary parts (in-phase and quadrature components) are independent and identically distributed zero-mean Gaussian variables with variance $\sigma/2$. When this applies speckle is termed as fully developed [24]. The joint probability density function (pdf) is given by eq.2.4,

$$p_{z_1 z_2}(z_1 z_2) = \frac{1}{\pi\sigma} e^{-\frac{z_1^2 + z_2^2}{\sigma}} \tag{2.4}$$

whereas the amplitude A is distributed as a Rayleigh pdf, that is eq.2.5,

$$p_A(A) = \frac{2A}{\sigma} e^{-\frac{A^2}{\sigma}} \tag{2.5}$$

and the power or intensity $I = A^2$ is distributed according to an exponential pdf, that is eq.2.6,

$$p_I(I) = \frac{1}{\sigma} e^{-\frac{I}{\sigma}} \tag{2.6}$$

so that the mean of the intensity is equal to σ. The received signal pdf can be reformulated as eq.2.7 or eq.2.8,

$$p_{I|\sigma}(I|\sigma) = \frac{1}{\sigma} e^{-\frac{I}{\sigma}} \tag{2.7}$$

or

$$I = \sigma u \tag{2.8}$$

where u is exponentially distributed, as in eq.2.9,

$$p_u(u) = e^{-u} \tag{2.9}$$

is termed the multiplicative model of speckle.

The model shows that the brighter pixels are affected by stronger disturbances than darker ones. A way to improve the estimation of σ is to average L independent intensity values related to the same position. This processing, named "multilooking", maintains the mean intensity σ but reduces the estimator variance to σ^2/L and a spatial resolution loss by a factor L. If the hypothesis of independent intensity measurements holds, the L-look averaged intensity I_L is Γ-distributed. In the presence of a scatterer much stronger than the others like the point target, the received signal pdf becomes a Rice distribution.

The most used model in the literature on despeckling is the following eq.2.10,

$$g = fu \tag{2.10}$$

where f is a possibly autocorrelated random process and represents the noise-free reflectivity, u is a possibly autocorrelated stationary random process, independent of f, and represents the speckle fading term, g is the observed noisy image. All the quantities in eq.2.10 may refer to either intensity or amplitude as well as single-look or multilook images. The fully developed speckle of single-look amplitude has a Rayleigh distribution. This model formulates speckle [25] as a multiplicative modulation of the scene reflectivity. Hence, the speckle effects are more pronounced in a high intensity area than in a low intensity area.

The variable u may be assumed as spatially correlated [26]. The Lapini *et.al* [27] has shown that a pre-processing step that makes speckle uncorrelated, that is "whitens" the complex signal, allows despeckling algorithms designed for uncorrelated speckle to be successfully applied when speckle is autocorrelated.

2.5.1 Sonar Image Spectral Analysis

The presence of speckle noise in ultrasound images has been documented since the early 1970s where researchers such as Burckhardt [28], described the fundamentals and the statistical properties of the speckle noise. Sonar senses and displays the amplitude of the signal reflected from the seabed or objects in the water column.

Although the direct display of the echo amplitude in image format provides a qualitative representation of the seabed, the signal can also be investigated statistically to yield information on the seafloor topography. The acoustic field scattered from a random rough surface, such as the seabed, is the sum of many elementary waves scattered by points along the surface. The field, which is a complex quantity, will possess approximately Gaussian distributions in the limit as the number of scattering events tends to infinity [29]. An analytical study of Gaussian fields arising from wave scattering from random rough surfaces is provided by Beckmann [30]. If the real and imaginary parts of the scattered field are uncorrelated and independent, the amplitude of the field is reduced to a Rayleigh distribution and the phase to a uniform distribution, as a result of the quadrature addition of the complex components.

The side scan sonar image displays the backscattered energy from the seabed. The probability density functions of several side scan sonar images produced by side scan sonar system with different operating characteristics representing a range of sediment types and seafloor structures were observed to follow Rayleigh distributions for isotropic regions of the seabed. A maximum likelihood estimator was employed to determine the parameters of the Rayleigh distribution. The actual distributions were then compared to the fitted Rayleigh distribution using a Chi-Square test. This test is employed to determine the consistency of two distributions, and a low valued result indicates a high probability that the two distributions are consistent.

Wagner [31] showed that the histogram of amplitudes within the resolution cells of the envelope-detected RF-signal backscattered from a uniform area with a sufficiently high scatterer density has a Rayleigh distribution with mean (μ) proportional to the standard deviation (σ), with $\sigma/\mu = 1.91$ which implies that speckle could be modeled as a multiplicative noise.

The distribution of the sonar reverberation has been investigated by Stanton [32] and Alexandrou *et.al.* [33]. Stanton related the probability density function to scattering theory to estimate the seafloor roughness, and noted that the shape of the pdf of the echo amplitude was dependent on the seafloor roughness. The backscattered energy from the seabed will be modified by the medium and transducer characteristics but the signal is dominated by the seabed reverberation, provided the sonar is operated in an environment with low noise and volume reverberation levels. The signal is primarily composed of the diffuse scattered energy, apart from the regions of near normal incidence occurring from the seabed below the towfish. The side scan sonar images can therefore be expected to be approximated by Rayleigh

statistics.

Image histograms are useful for revealing the relative proportions of geological components in a scene, but these proportions are commonly obscured by the variability caused by signal fading like image speckle. This variability can potentially be reduced by deconvolution, because a scene's probability density function is related to the Rayleigh log-pdf and pdf of backscatter strengths via a convolution integral. A simple deconvolution algorithm is demonstrated in [34], by separating a submarine lava flow from its adjacent sediments in a side scan sonar image histogram.

2.5.2 Additive Noise Model

The nonlinear nature of the relationship between the observed and noise-free signals in the model makes the filtering procedure a nontrivial task. For this reason, some manipulations have been introduced to make the observation model simpler. The multiplicative model is often manipulated in order to obtain an additive one as in eq.2.11,

$$g = f + (u-1)f = f + v \tag{2.11}$$

where $v = (u-1)f$ accounts for speckle disturbance in an equivalent additive model, in which v, depending on f, is a signal-dependent noise process.

A second way that allows the multiplicative noise to be transformed into an additive one is using a homomorphic transformation [35], [36]. It consists of taking the logarithm of the observed data, so that the eq.2.12 forms and can be written as eq.2.13

$$logg = logf + logu \tag{2.12}$$

$$g' = f' + u' \tag{2.13}$$

Here the noise component u' is a signal-independent additive noise. Logarithm reduces the contrast in the image and introduces a bias [37] into the denoised image, since an unbiased estimation in the log domain is mapped onto a biased estimation in the spatial domain [38]. The nonlinear mapping of the logarithm introduces a bias for the estimation of the parameters of the signal and noise.

Basic Additive Models of the Denoising Algorithms is shown in Fig 2.17. The block estimator attempts to achieve a speckle free representation of the signal in a specific domain; in the transform domain, as or in the homomorphic transform domain, in which the noise free informative signal is contaminated with additive

signal-dependent or signal-independent noise, respectively.

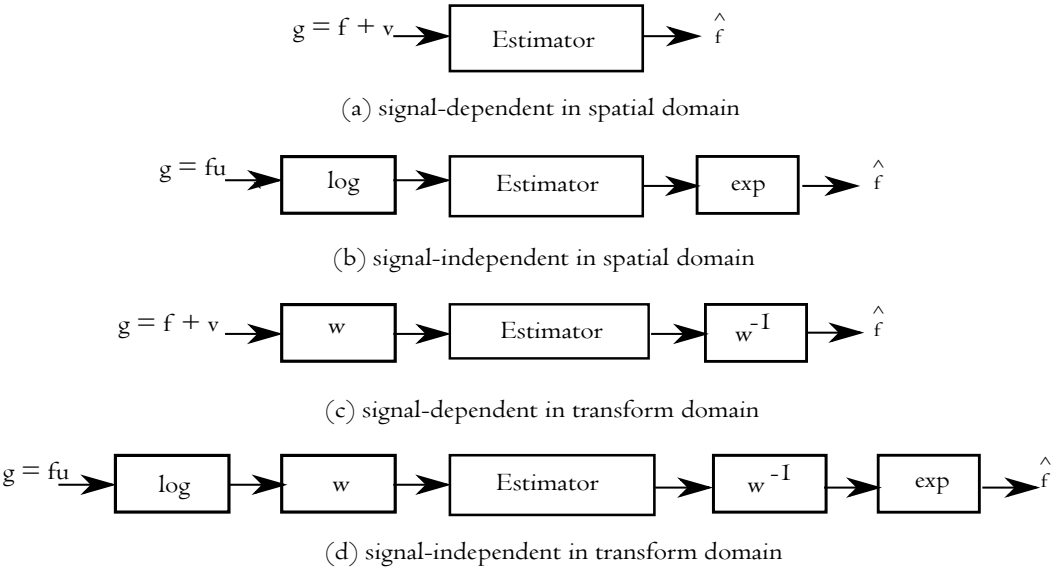

Fig. 2.17: Additive models commonly used in despeckling algorithms

Speckle noise suppression techniques can be divided into two categories. The first approach is to average several looks or images acquired of the same scene, which is called multi-look processing or super-resolution. If several images are acquired from the same scene and then averaged, the speckle noise will be reduced due to its random nature, while the observed scene will not be degraded. The second technique is based on filtering the speckle noise after the images are formed. The simplest filters that can be applied on the speckled image are low-pass and median filters. The low-pass filter locally averages the image and by doing so removes the speckle. It is useful when the areas of interest in the image are homogeneous, but has very poor performance at edges and with high frequency information textures. The mean filter averages the speckle in the data but lowers the resolution. The median filter, on the other hand, preserves the image edges, but can remove small area objects.

Standard filters such as Low-Pass, Gaussian, and Median generally degrade the observed scene. Contrary to the standard filters, the adaptive filters take local image information into consideration while carrying out the filtration process. Adaptive filters can reduce speckle noise in homogeneous areas while preserving texture and high frequency information in heterogeneous areas. Among the best known adaptive

classical speckle filters are the Lee [39], the Frost [40] and the Kuan [41] filters designed primarily for additive noise suppression. These filters use the second-order sample statistics within a minimum mean squared error estimation approach.

An image processing filter for speckle noise removal presented in [42] is a mean filter that numerically realizes a diffusion process. Linear filtering using mean filter and Least Mean Square (LMS) adaptive filter and nonlinear filtering based on median filter [43] does not produce considerable denoising for images corrupted with Gaussian noise or speckle noise. Classical wiener filter [44] is designed primarily for additive noise suppression. The multiplicative speckle noise that disturbs the sonar images can be transformed into an additive noise by obtaining the logarithm of the image and consequently applying the wiener filter. Adaptive weighted filter [45] is another non-linear order filter that aims to smooth the noise and simultaneously enhance edges and preserve thin structures.

2.5.2.1 Signal-Dependent Additive Noise Model

Jong-Sen Lee in 1980 introduced the local-statistics filter, a model-based despeckling filter. The solutions for both additive signal-independent noise and speckle noise was thoroughly developed in [46] and reviewed in [47] together with the sigma filter. By linearizing the multiplicative noise model around the mean of the noisy signal, an Least Minimum Mean Square Error (LMMSE) solution was derived. To overcome the drawback of edge boundaries that are left noisy by Lee filter, the Lee Refined Filter was designed. The algorithm uses the local gradient to estimate its orientation after detecting an edge. Better fitting of the edge orientation is done by estimating the local mean and of the local variance within the local window. Filtering results are quite impressive, particularly on edges and high contrast areas. Some artifacts may occur when the filter processes textured areas that result to be overly segmented.

Lee approximated the multiplicative noise model with a linear one, followed by applying a Minimum Mean Square Error (MMSE) criterion. Then an adaptive filter was formulated as eq.2.14,

$$\hat{R}(x,y) = \overline{I}(x,y)(1 - W(x,y)) + W(x,y)I(x,y) \tag{2.14}$$

where I is the acquired image, $\overline{I}$ is the average of an acquired image in a filter

window, and W is a weighting function given by eq.2.15,

$$W(x,y) = 1 - \frac{(C_u^2)}{(C_I^2(x,y))} \tag{2.15}$$

where $C_u = \frac{\sigma}{\overline{u}}$ and $C_I(x,y) = \frac{\sigma_I(x,y)}{\overline{I}(x,y)}$ are the coefficient of variation the noise and the acquired image, respectively. The σ and $\overline{u}$ is noise standard deviation and mean respectively, $\sigma_I(x,y)$and $\overline{I}(x,y)$ is the image standard deviation and mean respectively in the filter patch area around (x,y).

The Kuan filter is based on a unified approach to designing a noise smoothing filter for a class of signal-dependent observations such as multiplicative noise and Poisson noise. In Kuan's approach the multiplicative noise model is first transformed to a signal-dependent additive noise model, followed by applying the MMSE criterion. Then the original scene estimation can be formulated eq.2.16,

$$\hat{R}(x,y) = \overline{I}(x,y)(1 - W(x,y)) + W(x,y)I(x,y) \tag{2.16}$$

where W is a weighting function defined by eq.2.17,

$$W(x,y) = \frac{(1 - C_u^2/C_I^2(x,y))}{(1 + C_u^2)} \tag{2.17}$$

It can be seen from the equation that the Kuan filter provides more aggressive smoothing than the Lee filter.

Kuan *et.al.* [48] consider the restoration of images with signal-dependent noise. The filter is noise smoothing and adapts to local changes in image statistics based on a nonstationary mean, Non Stationary Mean Variance (NMNV) image model. The filter is able to adapt itself to the non stationary local image statistics in the presence of different types of signal-dependent noise. For multiplicative noise, the adaptive noise smoothing filter is a systematic derivation of Lee's algorithm with some extensions that allow different estimators for the local image variance. The advantage of the derivation is its easy extension to deal with various types of signal-dependent noise. Kuan filter LMMSE solution is referred to as local LMMSE (LLMMSE) to indicate that it contains only local first order statistics, mean and variance.

Frost *et.al.* derived a model for the radar imaging process and a method for smoothing noisy radar images. The imaging model shows that the radar image is corrupted by multiplicative noise. The model leads to the functional form of

an optimum (minimum MSE) filter for smoothing radar images. By using locally estimated parameter values the filter is made adaptive so that it provides MMSE estimates inside homogeneous areas of an image while preserving the edge structure. It is shown that the filter can be easily implemented in the spatial domain and is computationally efficient. The filtered value is a linear combination of pixel values within the local window with a Gaussian weighting function that depends on the local coefficient of variation of the noisy image g, namely C_g, defined as the ratio of local standard deviation to local mean.

The Frost filter is significantly different from the Lee and Kuan filters. It estimates the observed scene by convolution of the acquired image with the impulse response of the imaging system. The imaging system impulse response is obtained by using the MMSE criterion. Then the resulting filtering process can be defined by a convolution of the acquired image with the filter kernel eq.2.18,

$$\hat{R}(x,y) = I(x,y) * m(x,y) \tag{2.18}$$

where the filter kernel $m(x,y)$ is defined by eq.2.19,

$$m(x,y) = Ae^{(-KC_I(x,y)|d|)} \tag{2.19}$$

where K is the dumping factor of the impulse response (with typical values between 0.1 and 1), C_I is the same as in the Lee filter, A is a normalization constant that is the sum of the filter kernel elements, and d is the distance of the pixel from the kernel center defined as $d = x + y$. This is the most computationally complex filter.

Yan *et.al.* [49] proposed a noise filtering scheme that is based on Higher-Order statistics (HOS) for photographic images corrupted by signal-dependent film grain noise. In addition, reliable estimation of the noise parameter using HOS is proposed. This parameter estimation technique can be used to generate film grain noise which has applications in motion picture and television productions.

Despeckling uses the multiresolution signal analysis [50], such as the Discrete Wavelet Transform (DWT). In the non-homomorphic wavelet domain despeckling, the absence of the bias due to the nonlinear mapping of the logarithm is an advantage. The estimation of the signal parameters and the pdfs of noise are more complex in such filters. The noise term is signal-dependent for the non-homomorphic case and the parameters are much more difficult to be estimated. In the seminal paper by

Foucher *et.al.* [51], undecimated wavelet was firstly used for despeckling. Estimation is based on the Maximum A Posteriori (MAP) criterion and the Pearson system of distributions. The wavelet coefficient of the reflectivity is estimated with a Bayesian model, maximizing the *a posteriori* probability density function. The different probability density function is modeled with the Pearson system of distributions. The resulting filter combines the classical adaptive approach with wavelet decomposition where the local variance of high-frequency images is used in order to segment and filter wavelet coefficients.

The Meer's filter [52] and the filter based on the Rational Laplacian pyramid (RLP) [53] employ multiresolution concepts without a formal multiresolution analysis. This work has demonstrated that multiresolution processing is the key to adaptive filtering of signal-dependent noise.

Two novel architectures for real-time and low-power Field-Programmable Gate Array (FPGA) implementation of the Frost speckle filter for underwater imaging sonar are presented in [54]. The proposed architectures have superior performance and power efficiency compared to standard software implementation.

2.5.2.2 Signal-Independent Additive Noise Model

Sonar images are highly affected by speckle noise which reduces spatial resolution. A better denoising can be achieved by multi-resolution analysis utilizing the wavelet transform [55]. In the wavelet domain, the additive noise is uniformly spread throughout the coefficients, while most of the image information is concentrated in the few largest ones. The sparsity or the decorrelation capacity of the wavelet representation of the images is exploited in speckle denoising. The most straightforward way of distinguishing information from noise in the wavelet domain consists of thresholding the wavelet coefficients. The different wavelet denoising approaches differ in the selection of the threshold, time scale levels, and basic wavelet function. The signal denoising via wavelet thresholding or shrinkage have shown that various wavelet thresholding schemes for denoising have near-optimal properties in the *minimax* sense. Denoising using wavelets is quite different from traditional filtering approaches - it is nonlinear [56], due to a thresholding step.

Key problems concerning wavelet based denoising of images are choice of reasonable wavelet function, proper time scale levels, accurate thresholds and thresholding rules. Wavelet shrinkage methods frequently used are hard thresholding and soft

thresholding, have been investigated for speckle reduction of images on a logarithmic scale. The basic shrinking is thresholding [57], where the wavelet coefficient with small magnitudes is set to zero ("hard-thresholding") while keeping or shrinking in magnitude ("soft-thresholding") the remaining ones. The soft-thresholding rule is chosen over hard-thresholding. Bayesshrink rule [58] using a Bayesian mathematical frame work for images to derive subband dependent thresholds are merely optimal for soft thresholding.

Filtering in the wavelet-homomorphic domain has potentially superior performances over conventional spatial filters [59], [60]. In these filters each wavelet subband associated to a speckle contribution can be exactly measured [61] and filtered out. In such cases, the spatially adaptive filtering becomes scale-adaptive. In the classical hard-thresholding and soft-thresholding methods were applied. Thresholding based on nonlinear functions such as the sigmoid functions, adapted for each sub-band, has been used in [62]. To estimate the noise variance σ^2 from the noisy wavelet coefficients [63], a robust median estimator is used from the finest scale wavelet coefficients. It is the Median Absolute Deviation (MAD) of the highest-frequency subband coefficients divided by 0.6745 as given in eq.2.20,

$$\sigma = MAD\,|w_{HH}(x,y)|/0.6745 \tag{2.20}$$

where w_{HH} is wavelet sub-band HH.

The process estimation attempts to achieve a speckle free representation of the signal in a specific domain. If a process having some prior information about the signal to be estimated, a Bayesian estimator [64] tries to achieve an estimate $\hat{f}$ of f. The Bayesian implementation is based directly on Bayes'theorem, which can improve the estimation accuracy compared to the classical approach.

In BayesShrink rule, the threshold is determined for each sub-band by assuming a Generalized Gaussian Distribution (GGD). The threshold T is obtained by minimizing the BayesianRisk, i.e, the expected value of the mean square error. Different Bayesian estimators can be defined according to the choice of the Bayesian "risk", i.e., the function of the estimation error $\varepsilon = f - \hat{f}$ which could be minimized.

The MMSE estimator minimizes the quantity $[\varepsilon^2 = E[(f - \hat{f})^2]$. The solution is given by eq.2.21,

$$\hat{f}^{MMSE} = E_{F|G}(f|g) \tag{2.21}$$

which is the expectation of the noise-free signal f conditional to the noisy observation

g. For the MAP estimator, choose f to maximize the posterior pdf, eq.2.22,

$$\hat{f}^{MAP} = \arg\max_{f} p_{F|G}(f|g) \tag{2.22}$$

It is observed that the threshold value set by eq.2.23,

$$T = \sigma^2/\sigma_X \tag{2.23}$$

is very close to the optimum threshold. Here σ_X is the estimate of image information of the sub-band. The Bayesian risk minimization is subband dependent.

When $\sigma^2/\sigma_X << 1$, the signal is much stronger than the noise, the normalized threshold is chosen to be small in order to preserve most of the signal and remove some of the noise; when $\sigma^2/\sigma_X >> 1$, the noise dominates and the normalized threshold is chosen to be large to remove the noise which has overwhelmed the signal. Thus, this threshold choice adapts to both the signal and the noise characteristics as reflected in the parameters σ_X and σ.

Detection and classification of underwater mines with Synthetic Aperture Sonar images is a challenge that can be performed in studying either the echoes or the shadows of mines. However, SAS images present a strong speckle level due to the construction or the image itself. To reduce this speckle level, filtering methods are generally used but all of them strongly deteriorate either the shadow or the echo of the mine. Chaillan et al. [65] proposed a new speckle reduction method which allows to enhance jointly mines echoes and shadows. This process is based on the marriage between a multiresolution transformation and a filtering method.

Yang *et.al.* [66] proposes an improved image denoising algorithm, which based on wavelets thresholding and uses the Besov norm regularization. Since different parts of an image may have different smoothness properties, and wavelet coefficients denote different frequency sub-bands of an image, the sub images at each wavelets scale level may have distinct smoothness properties. Experimental results show that the method achieves better denoising effect than other methods.

Among the two kinds of WTs, the orthogonal non-redundant wavelet transform used in denoising applications is the DWT. This transform is most commonly used in its maximally decimated form as Mallat's dyadic filter tree. The main disadvantages like lack of shift invariance can be reduced using the Cycle Spinning and the lack of symmetry of the mother wavelets can be eliminated using complex WT or

biorthogonal WT. Unfortunately, the influence of poor directional selectivity where the orthogonality is lost cannot be reduced. The undecimated form of the DWT is named UDWT. This is a very redundant WT, having the last two disadvantages already mentioned. The Dual Tree Complex Wavelet Transform (DTCWT) is a redundant WT, with a redundancy of 4. Its architecture is based on two trees, each implementing a DWT.

Due to the finite support of the wavelet function, a strongly scattering target which is concentrated in space will be spread out after wavelet analysis.In [67] the wavelet analysis is performed after the targets are detected as upper percentiles of the image histogram, removing from the image and storing it. The void pixels formed are smoothly filled by interpolating their neighbours. Point targets are reinserted in their original places after synthesis of the despeckled image. To improve the performances of the other two classes, homogeneous and textured, the multiresolution methods was employed.

The sigma filter [68] developed for additive signal-independent noise and extended to speckle removal [69]. This filter uses the sigma probability of the Gaussian distribution, and it smooths the image noise by averaging only those neighbourhood pixels which have the intensities within a fixed sigma range of the center pixel. The method preserves the image edges and subtle details and thin lines are retained. An enhanced version of Lee's sigma filter [70] is derived and proposed for unbiased filtering of images affected by multiplicative noise with speckle statistics. In [71] the bias problem is solved by redefining the sigma range based on the speckle pdf.

In multiresolution analysis using wavelets [72], the objective was to eliminate the low energy components of the wavelet transform of the image since it is where the noise is contained. Sparsity of the wavelet representation of the images is exploited in speckle denoising in sonar images.

Firoiu *et.al.* [73] presents a new denoising method in the wavelet domain, which tends to reduce the speckle, preserving the structural features and the textural information of the scene. Shift invariance associated with good directional selectivity is important for the use of a Wavelet Transform (WT) in denoising of sonar images. The use of a variant of hyperanalytic WT, which is quasi-shift invariant and has good directional selectivity in association with a maximum *a posteriori* filter named bishrink which makes a very good treatment of the contours. The corresponding denoising algorithm is simple and fast.

Image denoising by the process of reducing or removing the noise from images

while the inpainting procedure involves the reconstruction of missing pixels in sonar images [74] in wavelet domain. Most of the literature available is for the removal of additive noise. So a logarithmic operation on the noisy image which give an additive equation. Then different wavelet shrinkage approaches are employed. Three variants of bishrink filter and a diversified denoising method that takes into consideration the structural and textural features of the image under analysis is proposed in [75].

2.5.3 Multiplicative Noise Model

The multiplicative speckle noise model expresses the observed intensity as the product of the scene signal intensity and speckle noise intensity. The model relates the two entities at each pixel as a function of speckle noise.

A non-linear filter Geometric filter (GF) [76] was developed to reduce speckle in SAR imagery while at the same time preserving spatial information. It is based on geometric concepts. GF iteratively erases noise samples regarded as geometric artifacts of the 3-D shape defined by the 2-D gray-level function. GF is a nonlinear local operator that exploits a morphologic approach to smooth noise. Thicker objects are just slightly smoothed and therefore fairly preserved as filtering is iterated. A decimated version of GF [77] is suitable for spatially correlated noise, including speckle.

The prototype of MAP filters in spatial domain is analyzed in [78]. Assuming a Gamma distribution to both the radar reflectivity and the speckle noise, the filter is designed to smooth out noise while retaining edges or shape features in the image. An optimum filter size selection is crucial in improving the performance. In the gamma MAP filter proposed by Lopes *et.al.*, pure averaging is used when the local coefficient of variation is below a particular threshold and above a particular threshold a strict all pass filtering is performed.

Simulated Annealing (SA) was originally used for image despeckling and segmentation by White [79]. SA is a stochastic optimization method used for finding the global maximum of an *a posteriori* multivariate distribution, or equivalently the global minimum of the energy function. Finding the global maximum of the *a posteriori* distribution or equivalently the global minimum of the energy function is often made difficult by local maxima (minima), which can easily trap the optimization algorithm. SA is iterative and the temperature controls the optimization, and it is decreased throughout the optimization process. Despite its potentiality, the unlikely

cartoon like smoothness produced by SA was noticed in [80].

The bilateral filter (BF), originally introduced in [81] for gray scale images, has been extended to despeckling as in [82]. Since bilateral filters assume an explicit notion of distance in the domain and in the range of the image function, they can be applied to any function for which these two distances can be defined. Bilateral filtering smooths images while preserving edges, by means of a nonlinear combination of nearby image values. The method is non-iterative, local, and simple. In an adaptive version of BF suitable for despeckling [83], the spatial weighting is a Gaussian function, whose span depends on the local coefficient of variation, analogously to the enhanced Frost filter. Despite its elegance and relatively low computational cost, in the presence of strong noise, like for single look images, speckle-oriented BF suffers from limitations given by the finite size spatial function, same as all local spatial filters. A way to overcome such a drawback is adopting a non local filtering approach.

In addition to the classical de-speckling filters, more complex filters developed include the iterative Speckle Reducing Anisotropic Diffusion (SRAD) filter [84], Gamma MAP filter and multi-scale wavelet decomposition [85] based filters using an adaptive soft-threshold of wavelet coefficients, SRAD filtration of wavelet coefficients and the Non Local Mean (NLM) filter [86]. The nonlocal (NL) filtering is a generalization of the concept of data-driven weighted averaging, in which each pixel is weighted according to its similarity with the reference pixel, and is dependent on the selection of reference pixel. The NLM filter is based on the simple idea of estimating the noise free image as a weighted average of noisy pixels given in eq.2.24,

$$\hat{f}(y) = \frac{\sum_x w(y,x)g(x)}{\sum_x w(y,x)} \tag{2.24}$$

where the weights $w(x,y)$ take into account the "similarity" between pixels $g(x)$ and $g(y)$. The key idea of the NLM filter is that the weights $w(x,y)$ are based on the Euclidean distance between local patches centered at $g(y)$ and $g(x)$, according to eq.2.25,

$$w(y,x) = exp(-\frac{1}{h}\sum_k \alpha_k |g(y+k) - g(x+k)|^2) \tag{2.25}$$

where $\alpha_k' s$ define a Gaussian window and h controls the decay of the exponential function.

In anisotropic diffusion [42], the diffusion coefficient is allowed to vary spatially

to encourage intra-region smoothing in preference to inter region smoothing and the diffusion coefficient is assumed to be a constant independent of the space location. The derivation speckle reducing anisotropic diffusion (SRAD) is tailored to coherent images [87]. SRAD is the edge-sensitive extension of the conventional adaptive filters. The SRAD exploits the instantaneous coefficient of variation as the edge detector in speckled imagery., SRAD overcomes traditional speckle removal filters in terms of mean preservation, variance reduction, and edge localization. However, the unrealistic smoothness introduced after iterated processing makes SRAD unsurpassed for cartoon-like images.

Given an image $I_0(x, y)$ having finite power and non-zero valued intensities over the image domain, the output image $I_0(x, y; t)$ evolves according to the Partial Differential Equation (PDE) as in eq.2.26 and eq.2.27,

$$\partial(x, y, t) = div[c(q)\nabla I(x, y; t)] \tag{2.26}$$

$$I(x, y; 0) = I_0(x, y) \ \frac{I(x, y; t)}{\partial\overline{\eta}}|_{\partial\Omega=0} \tag{2.27}$$

Where ∇ is the gradient operator, $I(x, y; t)$ is the intensity image estimated at position (u, v) at time t, $\partial\Omega$ denotes the border of the image support Ω, while $\partial\overline{\eta}$ is the outer normal to $\partial\Omega$; $c(q)$ is the diffusivity function of SRAD defined by eq.2.28,

$$c(q) = \left(1 + \frac{(q^2(x, y; t) - q_0^2(t))}{(q_0^2(t)(1 + q_0^2(t)))}\right)^{-1} \tag{2.28}$$

Where $q(x, y; t)$ is the instantaneous coefficient of variation (ICOV) that serves as the edge detector in speckled images and $q_0(t)$ is the diffusion threshold called the speckle scale function that is computed from a homogeneous region of fully developed speckle as in eq.2.29.

$$q_0(t) = \frac{\sigma_{I_h}(t)}{I_h(t)} \tag{2.29}$$

where $\sigma_{I_h}(t)$ and $I_h(t)$ are the intensity standard deviation and mean over a homogeneous area at time t, respectively.

Another popular denoising approach is based on Total Variation (TV) regularization [88]. The total variation of the image is minimized subject to constraints involving the statistics of the noise. The constraints are imposed using Lagrange multipliers. The solution is obtained using the gradient-projection method. The

proper norm for images is the total variation (TV) norm and not the L2 norm. TV norms are essentially L1 norms of derivatives, hence L1 estimation procedures are more appropriate for the subject of image estimation (restoration). The space of functions of bounded total variation plays an important role when accurate estimation of discontinuities in solutions is required. Several solutions exist to apply TV methods in the case of multiplicative noise [89]. In [90],the authors define the optimization problem in the original intensity domain and apply a data fidelity term based on a maximum *a posteriori* approach, assuming a Gamma distributed speckle and a Gibbs prior. When applying TV regularization in the logarithmic domain, convex TV problems can be obtained by applying different data fidelity terms, including the $L2$ norm [91]. Image denoising through TV regularization can be defined as the solution of a minimization problem given in eq.2.30,

$$\hat{f} = argmin_f J(f, g) \tag{2.30}$$

where the cost function to be optimized can be expressed as eq.2.31,

$$J(f, g) = \varphi(f) + \lambda\psi(f, g) \tag{2.31}$$

In the above equation, $\varphi(f)$ denotes a regularization term including prior information about the noise-free image f, whereas $\psi(f, g)$ denotes a data fidelity term. The regularization term is usually defined as the TV norm of the noise-free image, i.e. eq.2.32

$$\varphi(f) = \sum_y |\nabla f(y)| \tag{2.32}$$

where $|\nabla f(y)|$ denotes the magnitude of the gradient of f and can be computed as eq.2.33

$$|\nabla f(y)| = \sqrt{f_h(y)^2 + f_v(y)^2} \tag{2.33}$$

where $f_h(y)$ and $f_v(y)$ denote horizontal and vertical first order differences evaluated at pixel y, respectively. The minimization of the TV norm tends to promote a piecewise smooth image, which is usually a good prior for natural images, since it preserves important structures like edges. The data fidelity term can be defined according to several different approaches. A popular approach is to set the data fidelity term equal to the negative of the log-likelihood of f given the observed image

g, that is eq.2.34

$$\psi(f,g) = -\log p(f,g) \tag{2.34}$$

Other filters are multi-scale wavelet decomposition [92] based filters, using an adaptive soft-threshold of wavelet coefficients and a 2D Kalman filter implemented on a causal prediction window, the so called Non Symmetric Half Plane (NSHP) for elimination of speckle noise [93] in Synthetic Aperture Radar (SAR) imagery.

When the observation is linearly related to state, and the modeling errors are Gaussian, then the Kalman filter [94], provides an optimal estimate of the state. But in practice, an image sensor as in sonar can possess nonlinear characteristics. Julier *et.al.* [95] describe a new recursive linear estimator for filtering systems with nonlinear process and observation models. This method uses a parameterization of the mean and covariance which can be transformed directly by the system equations to give predictions of the transformed mean and covariance.

The Extended Kalman Filter (EKF) is probably the most widely used estimation algorithm for nonlinear systems. Many of these difficulties arise from its use of linearization. To overcome this limitation, the Unscented Transformation (UT) [96] was developed as a method to propagate mean and covariance information through nonlinear transformations. It is more accurate, easier to implement, and uses the same order of calculations as linearization.

Subrahmanyam *et.al.* [97] presents a novel approach based on the Unscented Kalman Filter (UKF) for image estimation in film-grain noise. The image prior is modeled as non-Gaussian and is incorporated within the UKF frame work using importance sampling. A small carefully chosen deterministic set of sigma points isused to capture the prior and is propagated through film-grain nonlinearity to compute image statistics.

In fact, natural images satisfy a sparse model, that is, the number of measurements can be smaller than size. Sparse models are at the basis of compressed sensing [98], which is the representation of signals with a number of samples at a sub-Nyquist rate. Some despeckling methods based on the compressed sensing paradigm and sparse representations [99], [100], [101] have appeared in literature.

The Non-Local (NL) filtering [102], [103] uses non-local averaging of all pixels in the image. NL filtering is a generalization of the concept of data-driven weighted averaging, in which each pixel is weighted according to its similarity with the reference pixel, as in the pioneering sigma filter. The NL mean filter [104] extends the

above method. It sets the weights according to the probability of similarity which provides an extension of the Euclidean distance between a local patch centered at the reference pixel and a similar patch centered at a given neighbouring pixel.

The Block-Matching 3-Dfilter (BM3D) [105] combines the advantages of the NL principle and of the wavelet representation:3-D groups of pixels are formed by collecting blocks of pixels drawn from different image locations and chosen according to their similarity with a reference block, and Wiener filtering is applied to the wavelet coefficients of such 3-D groups. Following the NL approach, an improved similarity measure has been proposed in [106]. Other approaches consider a Bayesian NL framework [107], which has been applied to the despeckling of both ultrasound images and SAR images [108]. The NL principle has been successfully applied also to despeckling in the wavelet domain [109].

A three-dimensional block matching [110] image de-noise algorithm was used to suppress the speckle noise in SAS imaging processing. It usually adopts adjacent sub-blocks of the image for 3D transformation, and attains image de-noise by processing in the transform domain. [110]

2.6 Summary

This chapter gives a review about the salient operational and functional features of sonar imaging systems, especially side scan sonar systems and various despeckling techniques in the literature.

Chapter 3

Methodology

This chapter describes the methodology adopted for the blind estimation of sonar images considering different speckle-scene models. The literature review revealed that signal-independent additive and multiplicative noise speckle-scene models can be used to develop new despeckling techniques which can be efficiently made use of for the blind estimation of sonar images. A detailed account of the assessment methods for evaluating the performance of the despeckling methods is also presented in this chapter.

3.1 Introduction

Estimation, both blind and non-blind techniques, of sonar images is an important field of study in the sonar image processing arena. Non-blind estimation techniques are used, when the noise levels are known *a priori* or in simulation studies when manually noise is added to the image. However, even with the knowledge of the true noise level, the performance of the non-blind denoising method is not always the best.

For blind estimation methods, the noise level is unknown and is usually estimated along with the denoising process. Thus, the blind estimation is carried out first by estimating the noise level using appropriate statistical methods, followed by the application of a non-blind denoising process. To improve the performance of the blind denoising, the statistical methods employed for noise level parameter estimated should be fine tuned before using the non-blind denoising process.

In the case of sonar images where the noise levels are unknown, blind denoising

techniques yield satisfactory results. Sonar images are mostly affected by speckle noise and thus need to be despeckled before further processing. Application of suitable despeckling filters, whose performance depends strongly on the speckle-scene models, forms the basis for despeckling.

Prototypes using diverse speckle-scene models were developed for blind estimation of the sonar images and performance studies have been carried out.

3.2 Speckle-Scene Models

Speckle-scene models available in literature are either additive models, which can be signal independent or dependent or multiplicative noise models. Despeckling can be done either in the observed spatial domain or transformed frequency domain. Efficient despeckling filters can be obtained in both spatial domain as well as in transform domain using the signal-independent additive and multiplicative speckle-scene models as depicted in Fig.3.1.

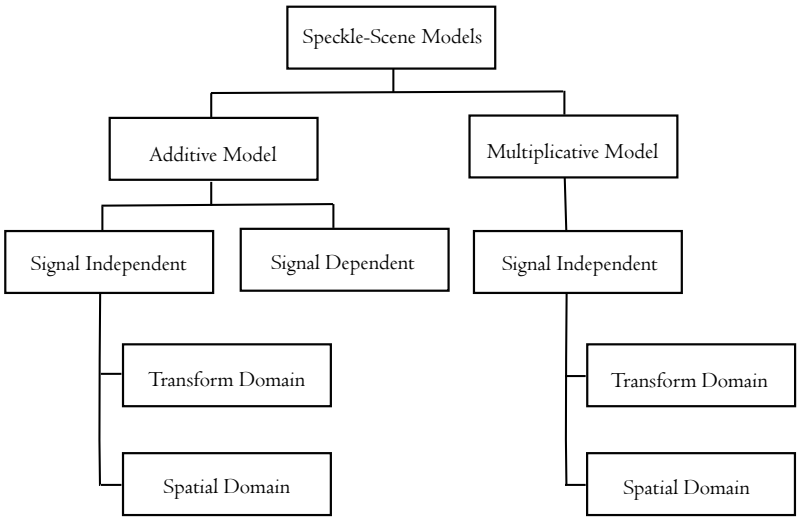

Fig. 3.1: Speckle-scene models used

As understood from the literature study covered in the previous chapter, the basic speckle-scene model for a sonar image can be multiplicative noise model. The homomorphic transformation when applied to the basic model yields the signal-independent additive noise model for the sonar image.

3.3 Estimation using Additive Noise Model

Sonar images, mostly homogenous and textured regions with relatively rare edges, are usually corrupted by multiplicative speckle noise. Homomorphic approach yields the signal-independent speckle-scene additive model for further processing in transform or spatial domain.

3.3.1 Transform Domain Estimation

The transform domain estimation method can be categorized into data adaptive or non-adaptive depending on the type of transforms used. In the non-data adaptive transform as in the multiresolution analysis method, a fixed basis is utilized while in the data adaptive transform the singular value decomposition or the principal component analysis method, a data adaptive basis is used. In addition, the computation complexity of the data adaptive method can been reduced by the applying the basis only on to the noisy image patches.

3.3.1.1 Multiresolution Method

In the multiresolution method, good denoising of sonar images can be achieved using the wavelet transform. The decomposition capability of the wavelet transform converts the signal into several scales which represent spatial distribution structure as well as different frequency bands. While the scene power is concentrated into a reduced number of wavelet transform coefficients, the noise power is distributed uniformly into all the wavelet transform coefficients. For distinguishing the information from noise, a threshold can be applied in the wavelet domain. Thus speckle reduction of images can be achieved through the use of hard thresholding, where the features are preserved or soft thresholding where smoothness is preserved.

The three steps in the wavelet denoising method are the computation of the forward wavelet transform, the application of threshold to the wavelet coefficients, and the computation of the inverse wavelet transform of the obtained result. It can be observed that the quality of the reconstructed image is a function of the threshold value, threshold rules and the selected multiresolution level.

3.3.1.2 Data Adaptive Transform Method

The Principal Component Analysis (PCA) and Singular Value Decomposition (SVD) are decorrelation techniques which seek an orthogonal basis for the representation of the sonar image. The decorrelation techniques basically redefine the data space, in terms of a set of data variables optimizing the statistical parameters like variances and singular values. These methods exploit the sparsity of the sonar images, as the singular values and eigenvalues of sparse images tend to decay exponentially. For a sparse matrix, even the assumption that the rank of the data matrix is lower than the sensor variables will yield us good results. The singular values and eigenvalues are arranged in the descending order and those values beyond the rank number will be set to zero. Reconstruction of the denoised data matrix is carried out using the remaining singular values and eigenvalues. The local principal components provide the best local basis set and the largest eigenvector is in the direction of the local image edge. Since the noise components are transformed into low eigenvalue feature components, by eliminating the lowest eigenvalues, the noise components associated with the sensors can be eliminated leading to dimensionality reduction. In comparison, the SVD denoising eliminates noise components associated with both the sensors and the pings. For blind denoising, the noise variance of the principal component coefficients for each patch is determined using the patch based estimation method and denoising of the coefficients is carried out using LMMSE estimator.

3.3.1.3 Noisy Image Patch Despeckling

The data adaptive method can be exercised on to the noisy image patches alone. The proposed heterogeneous patch classifier based on the naive homogeneity index identified is used for classification to the different statistical classes of patches *vis-a-vis* homogeneous, textured and target patches. In order to calculate the homogeneity index, the texture strength of each patch is calculated by taking the trace of the gradient covariance matrix of each patch. Approximating a gamma distribution for the texture strength and with the estimated noise variance, the homogeneity index is calculated.

The homogeneous patch , basically homogenous in nature, implying a spatially constant reflectivity, can use plain intensity averaging of the neighbouring pixel values as the viable denoising technique. The pixels belonging to the target patch which are intrinsically speckle-free, should be detected and left unprocessed. The interme-

diate patch is affected by speckle noise and denoising is done by decomposing the noisy image patches using principal components, estimating the clean coefficients, and reconstructing the final image.

3.3.2 Spatial Domain Estimation

SSS are used to produce high resolution acoustic images of the seafloor by moving the sonar forward and stacking the sonar response from successive pings with high resolution. The spatial domain denoising technique is used in denoising sonar images where each scan lines of the image is assumed to be unrelated in terms of speckle noise. With the additive speckle-scene model, the well developed Kalman filter based linear state estimation method is used for denoising in the spatial domain.

3.3.2.1 SSS Image Linear Estimation

The estimation method for image restoration exploits the side scan imaging technology, in which an independence exists in speckle characteristics of the each scan lines. Each row of data can be modeled by a state space equation and a measurement equation, with the current state being the current pixel value. The first stage of the algorithm is to perform the homomorphic filtering to transform the multiplicative noise model into an additive one. When the homomorphic transform is applied on to the sonar image, the observation becomes linearly related to state with Gaussian modeling errors. In a linear observation model, the Kalman filter provides an optimal estimate of the state. The process noise and the measurement noise are assumed to be white and independent of each other with normal probability distributions. In the Kalman filtering frame work, there are two occurrences to propagate the state variable through the transformation. One is in predicting the new pixel value from the past and the other is obtaining the observation from the predicted pixel value. The time update equations are responsible for projecting forward in time, the current pixel value and error covariance estimates to obtain the *a priori* estimates for the next time step. The measurement update equations are responsible for the feedback, i.e., for incorporating a new measurement into the *a priori* estimate to obtain an improved *a posteriori* estimate. Thus the method uses a one step pixel prediction for the sonar image estimation.

3.4 Despeckling using Multiplicative Noise Model

Images formed with coherent imaging techniques such as sonar imaging suffer from high frequency speckle noise, which reduces spatial resolution. While Gaussian noise can be modeled by random values added to an image, speckle noise can be modeled by multiplying random values with pixel values and hence it is also called multiplicative noise. The speckle effect introduces a variance to the intensity of each pixel and appears as a strong multiplicative noise where the variance of a point is identical to its mean.

Yet another proposed approach for denoising the sonar image uses the multiplicative speckle-scene model which can also be done in both the transform domain and in the spatial domain.

3.4.1 Transform Domain Despeckling

In the case of multiplicative noise model also, for denoising the sonar images, the data adaptive transforms like the Principal Component Analysis or the Singular Value Decomposition methods are used. A probabilistic patch based processing is employed to improve the noise removal.

3.4.1.1 Mixed Noise Removal by Processing of Patches

In case of sonar images, not much work has been carried out to effectively eliminate the mixed noise with additive and multiplicative components, due to the distinct characteristics of the degradation process induced by each component. The methods developed for additive Gaussian noise fail to suppress the speckle effect as they interpret the noisy pixels as edges to be preserved. Similarly the approaches for despeckling will retain most additive Gaussian noise in the restored images leading to grainy, visually disappointing results. Thus a two phase patch based mixed denoising algorithm has been proposed for additive Gaussian and multiplicative speckle noise removal in sonar images. In the first phase, the additive white Gaussian noise is removed by the sparse approximation of local image patches and in the second phase, despeckling is done on non-local patches formed by exploiting the noise distribution similarity between noisy patches. The Principal Component Analysis or the Singular Value Decomposition can be used for local patch denoising and the non-local patches by a weighted maximum likelihood denoising.

3.4.2 Spatial Domain Despeckling

In contrast with the transform domain, where some data adaptive transform methods are employed, the spatial domain approach works directly on the observed signal. In the spatial domain, the fractional integral mask based method, exploiting the high frequency noise removal property of the fractional mask can be used. In the case of the side scan sonar image, the UKF based estimation can be utilized.

3.4.2.1 High Frequency Filtering Method

A fractional integral mask acting as a low pass filter can be used to eliminate the high frequency noise signals in sonar images. Fractional calculus has proven to be better over integer calculus to analyze and model natural signals. Fractional order $\nu > 0$ corresponds to fractional differentiation whereas fractional orders $\nu < 0$ corresponds to fractional integration. The Riemann-Liouville definition for fractional integral calculus is used to create Fractional Integral Masks (FIM) in eight directions to be convolved with the data. The method can be optimized with the use of a single mask incorporated with the significant coefficients from all the eight directional masks and a single convolution operation of this mask with the image helps in obtaining the computational efficiency. The computational complexity can be further reduced by convolution of the mask only with the noisy patches.

3.4.2.2 Nonlinear Estimation Method

The Unscented Kalman filter, is a nonlinear state estimation method which provides an efficient recursive means to estimate the state of a process, in a way that minimizes the mean of the squared error. With the multiplicative speckle-scene model assumed, the unscented transformation is used for calculating the statistics of the random variable which undergoes a nonlinear transformation. The covariance of the process noise and the measurement noise were estimated first. The filter estimates the pixel value at certain location and then obtains feedback in the form of measurements. The predictor equations or the update equations are responsible for projecting forward the current pixel value and the error covariance estimates to obtain the *a priori* estimates for the next pixel value in the row. The measurement update equations or the corrector equations incorporate a new measurement into the *a priori* estimate to obtain an improved *a posteriori* estimate.

3.5 Assessment of the Despeckling Methods

An immediate and subjective approach for quality assessment is represented by visual inspection of filtered images. Visual inspection permits detection of the main human-visible features that characterize the behavior of a despeckling filter. Such features include edge preservation capability, degree of blur, point target preservation, as well as structural artifacts which are hardly detected by objective and direct measurements. On the other hand, visual assessment neither allows quantitative comparisons between the performances of different despeckling filters nor the measurement of bias introduced by the filter.

One of the most challenging tasks is the validation and quality assessment of data processed for speckle reduction. The most evident problem is that the noise-free reflectivity is unknown, so that no comparison can be carried out between the output of the despeckling process and the actual ground truth. Another important issue is the relationship between quality and fidelity of despeckled sonar data. Like many other denoising frameworks, the quality of a processed sonar image is usually evaluated in terms of blurring of homogeneous areas and detailed preservation in heterogeneous areas. Consequently, the radiometric preservation of the signal is an important requirement. A good despeckling filter should not introduce bias on the reflectivity.

In order to overcome the limitations of the visual comparison, several objective performance indexes have been proposed in the literature for the quality assessment of despeckling filters. They can be mainly divided into two classes: *with-reference* and *without-reference* indexes.

3.5.1 With-Reference Indexes

With-reference indexes are commonly used in the image denoising field for synthesized speckle noise, where reference image is known. A typical approach consists of choosing a reference image, either original or synthetic, representing the actual reflectivity or ground truth, and creating a synthetically degraded version according to a given signal model. The original speckle free image squared and multiplied by an exponentially distributed fading term can generate a synthetically speckled image which can be used as data for testing. This simulated data set will be a spatially uncorrelated and fully developed speckle image.

These indexes permit a quantitative and objective comparison between the per-

formances of different filters, which are expected to perform similarly on real sonar images. Moreover, insights on filters behavior on specific image features, like edge preservation and homogeneous areas smoothing, can be easily highlighted by choosing appropriate reference images. Unfortunately, experimental results carried out on simulated sonar images are not sufficient for inferring the performances of despeckling filters on real sonar images, since the synthetically speckled image may not be consistent with the actual sonar image formation and acquisition processes. Furthermore, the statistical properties of the chosen reference image and real ground truth reflectivity can substantially differ.

The most used model in the literature on despeckling as mentioned before is reflected in the eq.2.10, $g = fu$. The ability of the filter to preserve the texture is measured by Mean Square Error (MSE) between the original and filtered images. Despite the suppression of noise from the image, the error between the images must be as small as possible. The MSE, or Euclidean distance, between the ground truth f and the despeckled image, $\hat{f}$ and other measures derived from the MSE, like the SNR, the Peak Signal-to-Noise Ratio (PSNR) and the Energy Signal-to-Noise Ratio (ESNR), have been widely used for the quality assessment of both denoising and despeckling, [111], [112]. The equation for the MSE is eq.3.1,

$$MSE = E[(\hat{f} - f)^2] \tag{3.1}$$

In the presence of signal-dependent noise, the MSE is strongly influenced by the average signal level of the ground truth, unlike the case of additive signal-independent noise. Consequently, a quantitative evaluation of despeckling filters using this kind of indexes is strongly dependent on the content of the ground truth image, even though performance hierarchy is usually preserved across different images. The MSE based measurements are useful to obtain a global performance assessment on the whole image, but usually they yield little information about the preservation of specific features, for which other indexes as given in eq.3.2, eq.3.3 and eq.3.4 can be used.

$$SNR = 10 \log_{10} \left[\frac{var(f)}{MSE} \right] \tag{3.2}$$

$$PSNR = 10 \log_{10} \left[\frac{f_{PEAK}^2}{MSE} \right] \tag{3.3}$$

$$ESNR = 10 \log_{10} \left[\frac{E[f^2]}{MSE} \right] \tag{3.4}$$

3.5.2 Without-Reference Indexes

Without-reference indexes do not trust on the knowledge of the ground truth and use specific statistical hypotheses on the signal model. Since the signal model is strongly dependent on the degree of scene heterogeneity, a supervised selection of the most appropriate areas for the computation of a specific index, e.g., homogeneous areas, may be required. There are different statistical indexes to assess the quality of despeckling, without-reference image.

Typical measures can be computed from the ratio image r, defined as the point-by-point ratio between the noisy and the filtered image [113] as in eq.3.5.

$$r(n) = \frac{g(n)}{\hat{f}(n)} \tag{3.5}$$

The ratio image is a useful information in both homogeneous as well as heterogeneous scenes, where the fully developed speckle model hold. An ideal filter should result in a pure random pattern, whereas poor speckle noise removal causes structural information, such as borders and edges, to be clearly visible in the ratio image. The mean and the variance of r, that is $\overline{r} = E[r]$ and $var[r]$, should be as close as possible to the respective theoretical statistical moments of the speckle noise process. For this reason, they are often used as indexes of bias and speckle power suppression, respectively.

Another index is a measure of bias which is given by B index, where a value close to zero indicates an unbiased estimation given in eq.3.6.

$$B = E \left[\frac{[g - \hat{f}]}{g} \right] \tag{3.6}$$

Equivalent Number of Look (ENL) [114], [115] is one of the commonly used metric to quantify the quality of despeckled sonar images. The ENL is an index suitable for evaluating the level of smoothing in homogeneous areas, where the scene variation is supposed to be negligible with respect to speckle noise fluctuations. The ENL factor is related to the radiometric resolution of the image. ENL is the ratio of mean and standard deviation of the despeckled image and is calculated by using following

expression in eq.3.7,

$$ENL = \left(\frac{\mu_{\hat{f}}}{\sigma_{\hat{f}}}\right)^2 \tag{3.7}$$

where $\mu_{\hat{f}}$ and $\sigma_{\hat{f}}$ are mean and standard deviation of homogeneous area, $\hat{f}$ in despeckled image.

The ENL of the original sonar image is related to the nominal number of looks through the autocorrelation function of the speckle, whereas it increases after the despeckling stage according to the smoothing capability of the filter. A smaller value of ENL indicates more smoothing whereas a larger value indicates preservation of image features. In sonar images, the speckle variance is proportional to the mean intensity squared. Thus a large ENL indicates a small spread of values due to speckle. The higher the value of ENL, better the performance of despeckling technique.

The ratio of standard deviation to mean otherwise referred as Coefficient Of Variance (COV) can be used to measure the speckle strength in an image. Let g and $\hat{f}$ be original and speckle reduced sonar images respectively. The Speckle Suppression Index (SSI) [116] is denoted as the ratio of the coefficient of variance of despeckled image to the coefficient of variance of the original image as given in eq.3.8.

$$SSI = \frac{\sqrt{var(\hat{f})}}{mean(\hat{f})}\frac{mean(g)}{\sqrt{var(g)}} \tag{3.8}$$

SSI is always less than 1 and smaller values of SSI imply higher suppression of speckle noise.

Another without-reference index is the Correlation coefficient(CC). The CC for original image, f and despeckled image, $\hat{f}$ is calculated as in eq.3.9,

$$\rho_{g\hat{f}} = \frac{E[(g-\mu_g)(\hat{f}-\mu_{\hat{f}})}{\sigma_g \sigma_{\hat{f}}} \tag{3.9}$$

where μ_g and $\mu_{\hat{f}}$ are mean values of original and despeckled sonar images respectively and σ_g and $\sigma_{\hat{f}}$ are standard deviations of original and despeckled images respectively. Higher CC indicates better despeckling.

ENL and SSI are not considered as reliable measures when the despeckling algorithm overestimates the mean value. Therefore another method, *viz*, Speckle Suppression and Mean Preservation Index (SMPI) is used [117]. As the name suggests,

this index quantifies the speckle suppression and mean preservation capabilities of despeckling technique. The lower the value of SMPI, better the despeckling capability. The equations for SMPI is eq.3.10,

$$SMPI = Q\frac{\sqrt{var\hat{f}}}{\sqrt{var(g)}} \tag{3.10}$$

where $Q = K + |mean(\hat{x}) - mean(x)|$, with K given in eq.3.11,

$$K = \frac{max(mean(\hat{f})) - min(mean(\hat{f}))}{mean(g)} \tag{3.11}$$

Under the hypothesis of multiplicative speckle noise, a measure of texture preservation on heterogeneous areas is given by the comparison between the COV [118] calculated on the despeckled image, $C_{\hat{f}}$ as in eq.3.12, and the expected theoretical value on the noise-free image, C_f as in eq.3.13.

$$C_{\hat{f}} = \frac{\sqrt{Var[\hat{f}]}}{E[\hat{f}]} \tag{3.12}$$

$$C_f = \sqrt{\frac{C_g^2 - C_u^2}{1 + C_u^2}} \tag{3.13}$$

where C_g, the coefficient of variation of the observed noisy image and C_u, the coefficient of variation of the speckle noise. Intuitively, a poor preservation of details yields $C_f > C_{\hat{f}}$, while the introduction of impairments leads to $C_f < C_{\hat{f}}$.

3.6 Summary

The methodology suggested to be adopted for denoising the sonar images using different noisy signal models of the sonar images has been presented in this chapter. Different methods for the assessment of the despeckling methods are elaborated.

Chapter 4

Additive Noise Model Analysis

In this chapter a signal-independent additive noise model is assumed and the sonar image is estimated both in the transform domain and the spatial domain. For the signal-independent additive model, in the transform domain a mutiresolution analysis method and the sparsity of the natural sonar images are exploited for the denoising. In the spatial domain, a kalman filter based estimation method is used to denoise the side scan sonar image.

4.1 Introduction

Among the most widely used signal models for despeckling, the multiplicative model is often manipulated in order to obtain an additive one. In the additive signal models, the noise free informative signal is contaminated with either signal-dependent or signal-independent noise.The homomorphic transformation approach, which transforms the multiplicative noise into an additive one by taking the logarithm of the observed data, has the noise free signal affected by signal independent noise. However, this operation may introduce a bias into the denoised image, since an unbiased estimation in the log domain is mapped onto a biased estimation in the spatial domain. The processing can be done either in the homomorphic transform domain or in the homomorphic spatial domain.

4.2 Transform Domain

Bayesian thresholding method is proposed with a novel method for finding optimum multiresolution level based on PSNR values and visual quality, as an improvement on the classical thresholding approaches. For all the thresolding methods and the chosen wavelet function, the optimum multiresolution level for speckle reduction is found to be the maximum level of decomposition possible for the sonar image of size S to be despeckled. This method fine tunes the existing despeckling methods by optimizing the level of decomposition. The despeckling performance is further improved by choosing the optimum wavelet shrinkage rule for the image.

An efficient patch based and block based image despeckling algorithms, where the noisy image patches are represented using Principal Components and Singular Values, is also proposed. This work presents a framework for despeckling by learning a suitable basis to represent each image patch. The local basis functions are determined adaptively from the local image patches as opposed to being fixed for the entire image as in wavelet based technique and then being applied adaptively to local image patches. The results emphasized the strengths of this new decomposition approach for sonar image which are sparse and the details are of high frequency.

The data adaptive method is extended by applying to the noise affected patches only. For the patch classification, the proposed naive homogeneity index exploiting the heterogeneous nature of the sonar image is used. The heterogeneous patch classification is based on the texture strength of the patches unlike the traditional techniques which are based on the coefficient of variation. The method is computationally efficient, smoothens the uniform regions, preserving edges and features.

4.2.1 Multiresolution Method

Sonar images are highly affected by speckle noise which reduces spatial resolution. Denoising is required in sonar images to distinguish a number of different regions by analyzing the image. The proposed technique enhances the denoising property of the classical thresholding and the Bayes soft thresholding technique by proper selection of time scale level. The optimum mutiresolution level for speckle reduction is found to be the maximum level of decomposition possible for the image of size S to be denoised and the chosen basic wavelet function. The method is compared and evaluated based on the Peak Signal to Noise Ratio.

Sonar images [119] are highly unreliable due to the presence of speckle noise

which reduces spatial resolution by giving a variance to the intensity of each pixel. Sonar image of an object will closely resemble the optical image of the same but has less resolution than the optical image. The signal to noise ratio of such signals can be very low depending on the acquisition conditions and they contain almost homogeneous and textured regions with relatively rare edges. The spatial resolution of the side scan sonar image will be the constraining factor in its performance. The nominal resolution corresponds to the minimum distance between two objects that can still be distinguished on the sonar image.

Classical wiener filter is designed primarily for additive noise suppression. A homomorphic approach is suggested for addressing the multiplicative speckle noise. The multiplicative speckle noise that disturbs the sonar images can be transformed into an additive noise by obtaining the logarithm of the image and consequently applying the wiener filter. To obtain the denoised result, the logarithm inversion is performed at the end of the process.

The method described uses a wavelet decomposition method to remove the speckle noise from sonar images. The multiresolution analysis [120] represents the signals in different scales efficiently and helps images to be approximated from coarse to fine resolution. The method gives the optimum multiresolution level for speckle reduction. During the process, the sonar image quality is enhanced in terms of PSNR and resolution.

4.2.1.1 Wavelet Thresholding Rules for Denoising

The speckle noise produced due to the coherent nature of scattering phenomenon is of multiplicative nature. Most of the literature available is for the removal of additive noise. The method is to perform a logarithmic transformation to convert the multiplicative speckle noise into an additive noise, followed by a wavelet decomposition on the input noisy sonar image to pack the energy of the image into a few large coefficients, then modify the noisy wavelet coefficients using certain shrinkage functions. Finally, the denoised image is reconstructed by performing an inverse wavelet transform, followed by an exponential transformation.

First a logarithmic operation on the noisy sonar image with multiplicative model, $g(x,y) = f(x,y)u(x,y)$ is done which gives an additive equation. Then the observed data, $g'(x,y) = f'(x,y) + u'(x,y)$, contains the true signal $f'(x,y)$ with the additive noise $u'(x,y)$, independent and identically distributed. Let $W(.)$ and $W^{-1}(.)$ denote

the forward and inverse wavelet transform operators. The ultimate aim to remove the noise, or "denoise" $g'(x,y)$, and obtain an estimate $\hat{f}'(x,y)$ of $f'(x,y)$ which minimizes the mean squared error.

Let $G = Dg'$ denote the matrix of wavelet coefficients of g', where D is the two-dimensional dyadic orthogonal wavelet transform operator, and similarly $F = Df'$ and $U = Du'$.

The wavelet threshold denoising method filters each coefficient G from the detail sub-bands with a threshold function to obtain F. The denoised estimate is then $D^{-1}\hat{F}$, where D^{-1} is the inverse wavelet transform operator. DWT on 2-dimensional data is shown in Fig.4.1.

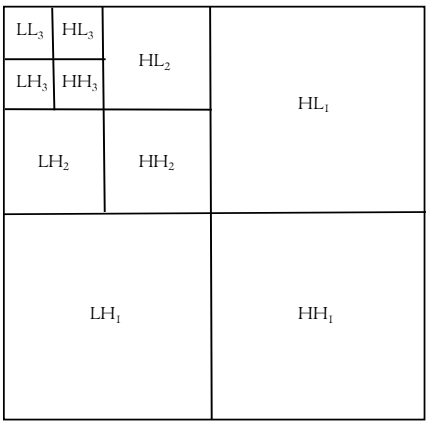

Fig. 4.1: DWT on 2-dimensional data

The sub-bands $HH_k, HL_k, LH_k, k = 1, 2, .. j$ are called the details, where k is the scale and j denotes the largest or coarsest scale in decomposition and LL_k is the low resolution component. Thresholding is now applied to the detail components of these sub-bands to remove the unwanted coefficients, which contribute to noise. Since speckle noise lies in the high spatial frequency region, it will reduce to near zero after a finite number of repeated smoothing operations. Reconstruction of the denoised image can be achieved through performing the inverse WT and taking the exponent.

When the image is in the wavelet domain, most of the image information is concentrated in the few largest coefficients while the additive noise is uniformly spread throughout the coefficients. For sonar image despeckling, the sparsity or the decorrelation capacity of the wavelet representation of the images is used. For distinguishing

information from noise in the wavelet domain, the most straightforward way is to threshold the wavelet coefficients.

The different wavelet denoising approaches differ in the selection of the threshold, time scale levels, and basic wavelet function. The signal denoising via wavelet thresholding or shrinkage have shown that various wavelet thresholding schemes for denoising have near-optimal properties in the *minimax* sense. The proposed method gives the optimum time scale level for the speckle reduction in sonar images for different wavelet shrinkage rules. Instead of blindly assuming a multiresolution level, give the last level for which at least one coefficient is correct for the image. This maximum level decomposition of image varies with the size of the image and the basic wavelet function chosen.

Key Problems Concerning Wavelet Denoising

1. Choice of Reasonable Wavelet Function
2. Choice of Proper Time Scale Levels
3. Determination of Accurate Thresholds
4. Choice of Suitable Thresholding Rules

Some of the experimental results obtained while dealing with the key problems concerning wavelet denoising are:

1. Choice of Reasonable Wavelet Function

The first step in denoising is to select a wavelet for the forward and inverse transformation. They differ in their support, symmetry and number of vanishing moments. Two wavelet-based noise reduction methods exists, the traditional spatially selective noise filtration technique and the threshold based denoising algorithm using the undecimated discrete wavelet transform (UDWT). UDWT can suppress noise better than discrete wavelet transform (DWT). Based on the direct spatial correlation of wavelet transform at several adjacent scales, a high correlation is used to judge whether there is a significant edge. For these implementations the choice of noise power reference is very important and a non-blind denoising approach is applied. For improving the filtering performance, edges can be extracted from coarse scales to fine scales.

Regarding the selection of a particular wavelet for the work, the optimal choice depended on the image selected. The work used different wavelets and compared

the result using MSE or PSNR indexes. For the simulation, a sonar image was taken and a speckle noise of variance 0.02 was added to it. The type of thresholding used is hard thresholding and shrinkage rule is SureShrink. For the analysis, different basic wavelets like the *haar*, *db*4, and $coif5$ were applied separately for the restoration of sonar image containing speckle noise as shown in Table.4.1.

Table 4.1: Choice of reasonable wavelet function

No. of Levels	2	2	3	3
Wavelet	MSE	PSNR	MSE	PSNR
Haar	357.66	22.5961	357.7102	22.5955
db4	355.4453	22.6231	356.6525	22.6084
coif5	356.9369	22.6049	353.1068	22.6517

2. Choice of Proper Time Scale Levels

Other than the choice of the wavelet, there can be a choice for the number of mutiresolution levels to be used based on several boundary treatment rules. In simulation it is seen that this optimum level calculation was optimum for the Bayes soft threshold method. It has been observed that the PSNR values were getting reduced for both the levels $L = 7$ and $L = 9$ compared to $L = 8$ which has been obtained as the optimum level for the image of the given size. The threshold selection is based on *minmax* method. The PSNR values were observed for different levels of decomposition of the image. Maximum PSNR values for Haar, Daubechies, and Coiflets were obtained at levels of decomposition 8, 5, and 3 respectively as in Table4.2. This is the maximum level of decomposition of the selected image for the chosen basic wavelet function and is called the optimum multiresolution level.

3. Determination of Accurate Thresholds

Various shrinkage functions that determine how the threshold is applied are hard thresholds, soft thresholds, garrote and semisoft thresholds. As the reconstructed image quality will change with the change in threshold value, finding the optimum threshold value t is a key problem. A small threshold value will pass all the noisy coefficients, the variance will get too large and smoothening of the image will be less. As the threshold value increases, more number of coefficients becomes zero which leads to smoother signal and destroys details and as a result image quality decreases. An efficient method for finding the threshold value for denoising is by analyzing the statistical parameters of the wavelet coefficients [121].

The hard threshold function as given in eq.4.1 keeps the input if it is larger than

Table 4.2: PSNR values of different levels of decomposition

Level	haar	db4	coif5
2	25.7723	25.7885	26.1952
3	25.9035	25.8819	**26.5427**
4	25.8849	25.8995	26.345
5	25.8971	**25.9432**	26.5377
6	25.8648	25.7686	26.5289
7	25.8229	25.7746	26.4956
8	**26.1932**	25.7914	26.5075
9	25.8517	25.8526	26.4652

the threshold t; otherwise, it is set to zero.

$$T_H = x.1\{|x| > t\} \tag{4.1}$$

The soft threshold function, as shown in eq.4.2 takes the argument and shrinks it towards zero the threshold **t**.

$$T_S = sgn(x).max(|x| - t, 0) \tag{4.2}$$

The pictorial representation of the equation is shown in Fig.4.2.

Fig. 4.2: Thresholding

An advantage of soft thresholding is that it provides smoothness while hard thresholding preserves features. The different thresholding techniques applied on given image with *haar* wavelet at a level of decomposition of 8 is shown in Table.4.3.The importance of thresholding rule for the selected wavelet at a particular chosen level of decomposition is depicted in the table.

4. Choice of Suitable Thresholding Rules

There exist various methods for wavelet thresholding, which rely on the choice of a threshold value. Some typically used methods for image noise removal include VisuShrink, SureShrink, and BayesShrink. For all these methods the image is first subjected to a discrete wavelet transform, which decomposes the image into various sub-bands.

Table 4.3: Threshold choice

Optimum Level	8	8
Thresholding	MSE	PSNR
Soft	287.6347	23.5424
Hard	357.4313	22.5989
Bayes	167.4678	25.8915

VisuShrink uses a threshold value t that is proportional to the standard deviation of the noise. It follows the hard thresholding rule and is also referred to as universal threshold defined as in eq.4.3:

$$t = \sigma\sqrt{2\log n} \tag{4.3}$$

with σ the noise variance present in the signal and n represents the signal size or number of samples. To estimate the noise variance eq.2.20 is used. VisuShrink does not deal with minimizing the mean squared error. It can be viewed as general-purpose threshold selectors that exhibit near optimal minimax error properties and ensures with high probability that the estimates are as smooth as the true underlying functions. For image denoising, VisuShrink is known to yield overly smoothed images as its threshold choice called the universal threshold and the noise variance, can be unwarrantedly large due to its dependence on the number of samples, which is high for a typical test image sizes.

A threshold selector based on Stein's Unbiased Risk Estimator (SURE) is called as SureShrink. It is a combination of the universal threshold and the SURE threshold. This method specifies a threshold value t_j for each resolution level j in the wavelet transform which is referred to as level dependent thresholding. The goal of SureShrink is to minimize the mean squared error. SureShrink suppresses noise by thresholding the empirical wavelet coefficients. The SureShrink threshold t_S^* is defined as in eq.4.4

$$t_S^* = min(t, \sigma\sqrt{2\log n}) \tag{4.4}$$

where t denotes the value that minimizes Stein's Unbiased Risk, σ is the noise variance and n is the size of the image. SureShrink follows the soft thresholding rule. A threshold level is assigned to each dyadic resolution level by the principle of minimizing the Stein's Unbiased Risk Estimator for threshold estimates and so it is an adaptive threshold method. It is smoothness adaptive, i.e. if the unknown function contains abrupt changes or boundaries in the image, the reconstructed image

also does.

In BayesShrink rule, the threshold is determined for each sub-band by assuming a GGD and the goal of this method is to minimize the Bayesian risk. The threshold t is obtained by minimizing the BayesianRisk, i.e, the expected value of the mean square error. It uses soft thresholding and is sub-band-dependent, which means that thresholding is done at each band of resolution in the wavelet decomposition and is smoothness adaptive. For the noise model $g = fu$ after the homomorphic transformation with $g' = f' + u'$, the Bayes threshold, t_B is defined as in eq.4.5.

$$t_B = \sigma^2/\sigma_{f'} \tag{4.5}$$

where σ^2 is the noise variance and $\sigma_{f'}$ is the signal variance without noise.

The determination of accurate thresholds and thresholding rules is shown in Table4.4. Simulation results show that the Bayesian soft thresholding method has the

Table 4.4: Determination of accurate thresholds and thresholding rules

No: of Levels	2	2	3	3
Threholding Rule	MSE	PSNR	MSE	PSNR
Soft	987.2228	18.1867	987.7221	18.1845
Hard	355.8919	22.6176	359.3575	22.5755
Bayes	172.4229	25.7649	167.3647	25.8942

maximum PSNR compared to the other thresholding methods. It can be observed that the quality of the reconstructed image is a function of the threshold value, threshold rules and the selected multiresolution level. The Table4.4 shows the importance of determination of accurate thresholds and thresholding rules as can be noticed that the PSNR values have significant difference between the soft, hard and Bayes thresholding rules.

4.2.1.2 Optimum Multiresolution Level for Classical Approach

The wavelet thresholding procedure removes noise only by thresholding the wavelet coefficients of the detail sub-bands, while keeping the low resolution coefficients unaltered.

Fig.4.3 shows the PSNR values observed at different levels of decomposition for

three different wavelets *haar*, *db*4, and *coif*5 using the hard thresholding method. The maximum PSNR values were observed at the optimum multiresolution level for three wavelets which were 8, 5, and 3 respectively as shown in Table4.5.

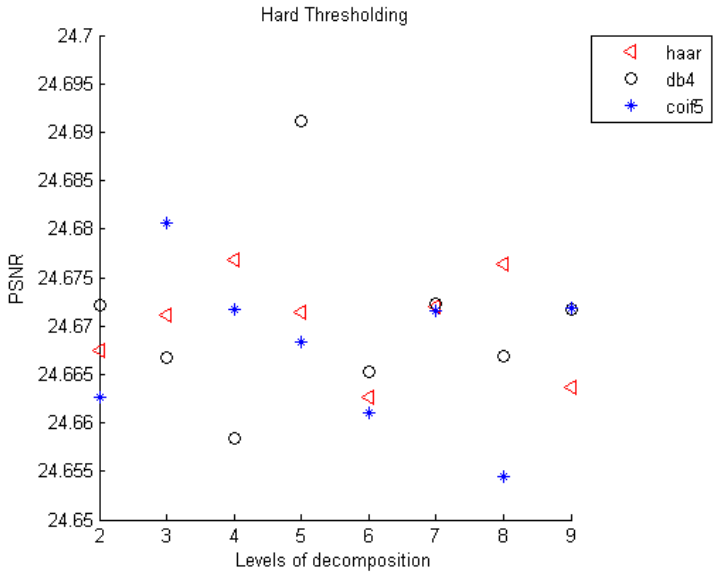

Fig. 4.3: Decomposition levels for different wavelets using hard thresholding

Table 4.5: PSNR values for hard thresholding

n	2	3	4	5	6	7	8	9
haar	24.6674	24.6711	24.6768	24.6714	24.6626	24.672	**24.6764**	24.6637
db4	24.6721	24.6667	24.6584	**24.6912**	24.6653	24.6723	24.6669	24.6717
coif5	24.6626	**24.6807**	24.6717	24.6684	24.6611	24.6716	24.6544	24.6718

The Fig.4.4 shows the Performance at different decomposition levels for three different wavelets *haar*, *db*4, and *coif*5 using soft thresholding method. The maximum PSNR values were observed at the optimum multiresolution level for three wavelets which were 8, 5, and 3 respectively as shown in Table4.6.

For the chosen image of size, S and the selected wavelet, the optimum multiresolution levels for the hard thresholding and soft thresholding method is obtained as the maximum level decomposition of image. As the level is decreased or increased, the performance degradation is observed.

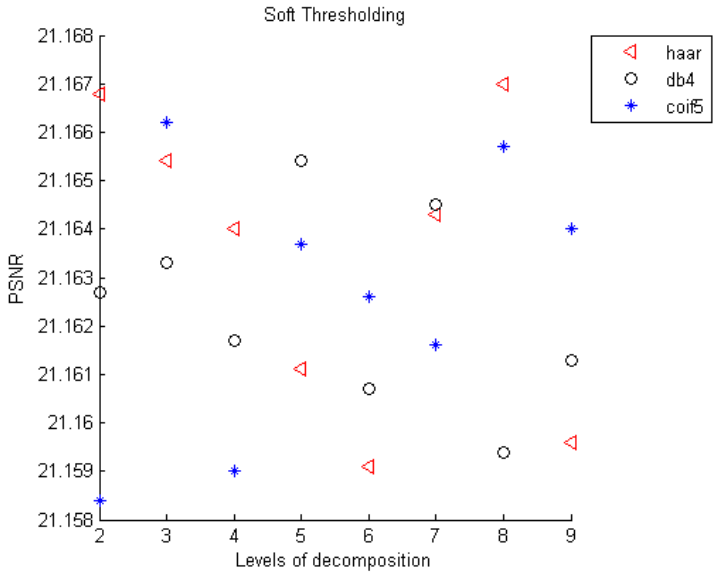

Fig. 4.4: Decomposition levels for different wavelets using soft thresholding

Table 4.6: PSNR values for soft thresholding

n	2	3	4	5	6	7	8	9
haar	21.1668	21.1654	21.164	21.1611	21.1591	21.1643	**21.167**	21.1596
db4	21.1627	21.1633	21.1617	**21.1654**	21.1607	21.1645	21.1594	21.1613
coif5	21.1584	**21.1662**	21.159	21.1637	21.1626	21.1616	21.1657	21.164

4.2.1.3 Optimum Multiresolution Level for Bayesian Approach

Bayes threshold choice adapts to both the signal and the noise characteristics. Simulation results show that the Bayesian soft thresholding method has the maximum PSNR compared to the other thresholding methods. The PSNR for the noisy image is found to be 24.6756. For the chosen image of size, S and the selected wavelet, the optimum multiresolution levels for the Bayesian method is obtained as the maximum level decomposition of image. The PSNR value for this method is 30.0954. As the level is decreased or increased, the performance degradation is observed in Bayes thresholding method also. Fig.4.5 depicts the results. The optimum multiresolution level for three different wavelets *haar*, *db*4, and $coif5$ using the Bayes thresholding method were 8, 5, and 3 respectively as in Table4.7.

The results demonstrate the variation in denoising effectiveness with the choice

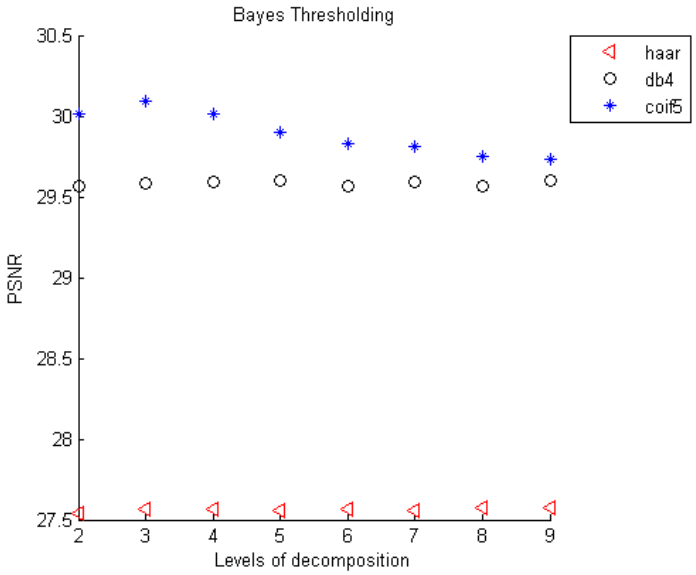

Fig. 4.5: Decomposition levels for different wavelets using Bayes thresholding

Table 4.7: PSNR values for Bayes thresholding

n	2	3	4	5	6	7	8	9
haar	27.5396	27.5642	27.5617	27.5591	27.5649	27.5593	**27.5577**	27.5727
db4	29.5658	29.5872	29.5917	**29.604**	29.5627	29.5927	29.5687	29.011
coif5	30.0146	**30.095**	30.096	29.8978	29.8274	29.812	29.7529	29.7363

of basic wavelet function, the wavelet shrinkage used and the multiresolution level. The new approach can achieve fairly desired denoising effectiveness. The level of decomposition is calculated based on the size of the selected image. Different basic wavelets were chosen separately for the proposed denoising algorithm for the restoration of image containing speckle noise.

The Fig.4.6 depicts a noisy image with speckle noise and the denoised image using the coiflets wavelet function using Bayes thresholding. A novel method for finding optimum multiresolution level based on PSNR values and visual quality is proposed, as an improvement over the classical thresholding approaches and the Bayesian thresholding method. For all the thresolding methods, the optimum multiresolution level for speckle reduction is the maximum level of decomposition possible for the image of size S to be denoised and the chosen basic wavelet function. This method fine

tunes the existing denoising methods by optimizing the level of decomposition and the optimum wavelet shrinkage rule for the image.

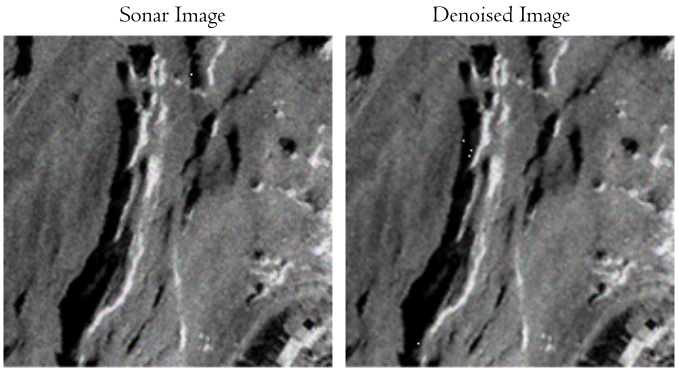

Fig. 4.6: Denoising using Bayes thresholding of Coiflets wavelet function

The simulation results on different size sonar images with their respective maximum level of decompositions for two different types of wavelet functions coif5 and dB4 are given in Table4.8 and Table4.9 respectively. The results show that the maximum level of decompositions possible on a sonar image vary with the size of the image to be processed and the type of the wavelet function used.

Table 4.8: PSNR values for different thresholding at maximum level of decomposition for coif5 wavelet

Image size	n	Soft	Hard	Bayes
211x232	2	16.7135	24.5524	22.9158
279x332	3	11.957	23.2983	12.5648
201x100	1	13.6356	25.2645	25.3437
240x476	3	13.6469	21.6851	23.9731
473x476	4	18.2552	23.0926	31.1466
361x360	3	21.1684	24.6615	30.0944
400x340	3	9.9864	19.2699	28.4681

4.2.2 Data Adaptive Transform Method

The data adaptive transforms, Principal Component Analysis and Singular Value Decomposition methods was used for denoising the noisy sonar image, image patches and blocks of patches. All of these methods exploited the sparse characteristics

Table 4.9: PSNR values for different thresholding at maximum level of decomposition for dB4 wavelet

Image size	n	Soft	Hard	Bayes
211x232	4	16.7141	24.4882	23.3047
279x332	5	11.9569	23.2753	12.8731
201x100	3	13.635	25.297	25.0581
240x476	5	13.6463	21.6756	24.0455
473x476	6	18.2577	23.1013	30.6008
361x360	5	21.162	24.6548	29.5957
400x340	5	9.9864	19.2688	28.369

of the sonar images. PCA and SVD are decorrelation techniques which seek an orthogonal basis for representation of the data space assumed to be linear. They redefine the data space in terms of a set of data variables which optimize certain statistical measures such as variances or singular values. Majority of the existing denoising algorithms are some form of a low pass filtering, while edges in the sonar images have high frequency components and noise removal can result in drastic loss of information. Fixed basis as in wavelet method is inappropriate in dealing with such sonar images. By generating 2-D basis sets, which have vectors lined up along the edges, and not across them, the high frequency coefficients caused by edges are much smaller [122]. The data adaptive denoising algorithms using PCA and SVD retains the edges.

Classical techniques of processing and analysis may fail since speckle noise in sonar images manifests itself as multiplicative non-Gaussian noise in the intensity domain. The degradation model $g = fu$ is used to describe the multiplicative noise affected sonar images where g is the observed image intensity, f is the noise-free reflectivity and u the multiplicative speckle fading term statistically independent of f with Rayleigh distribution. The implemented work uses homomorphic approach to convert the multiplicative noise to additive one and then local patches are processed exploiting the sparsity of the real images. The homomorphic approach convert the multiplicative signal model into a signal independent additive Gaussian noise model as $logg = logf + logu$ rewritten as $g' = f' + u'$, where the noise component u' is a signal-independent additive noise.

The image to be denoised is assumed to be affected by additive white Gaussian noise with zero mean and fixed, unknown standard deviation σ. For blind denois-

ing the noise variance of the image is estimated using eq.2.20 and the problem of despeckling is now modified as rejecting the additive noise of the known variance. Comparison of the different methods is done using different *without-reference* image performance evaluation criteria.

For the sonar image, the unknown standard deviation $\sigma_{f'}$ of the noisy image is estimated using the the noise level estimation algorithm. For the blind denoising of the image, $\sigma_{f'}$ needs to be estimated together with the denoising process. Blind denoising in images consists of two process, the estimation of the noise level in the image and then the non-blind denoising.

The variance $\sigma^2_{f'}$, is estimated using the maximum likelihood estimator eq.4.6.

$$\sigma^2_{f'} = max\left[0, \frac{1}{M}\sum_i f_i'^2 - \sigma^2\right] \tag{4.6}$$

Then denoise the coefficients using LMMSE estimator [123] given in eq.4.7

$$f_i' = \left(\frac{\sigma^2_{f'}}{\sigma^2_{f'} + \sigma^2}\right) \times g_i' \tag{4.7}$$

where f_i' is the denoised image coefficient or clean coefficient after the additive noise removal.

Denoising is done by decomposing the log transformed noisy image, image patches and blocks of patches as Principal Components or SVD coefficients, estimating the clean coefficients, and reconstructing the final image.

4.2.2.1 Despeckling by PCA and SVD

An $M \times N$ data matrix is generated by a sonar sending out M pings and N sensors. In linear matrix algebra, if X denotes the real value $M \times N$ data matrix, the rank r of X matrix represents the number of linearly independent vectors defined either along rows or columns, and is always less than or equal to the smaller of the two, ie. $r < min(M, N)$.

Eigenvalues and singular values of natural images tend to decay exponentially. The rank of the data matrix is assumed to be lower than the sensor variables and all descending order arranged eigenvalues and singular values beyond the rank number will be set to zero. Reconstruct the denoised data matrix by using the remaining

eigenvalues and the singular values. The feature directions, eigenvectors of PCA and singular values of SVD are usually referred to as the virtual sensors.

The local principal components provide the best local basis set and the largest eigenvector is in the direction of the local image edge. The noise components are transformed into low eigenvalue feature components. By eliminating the lowest eigenvalue components, not only dimensionality reduction but also elimination of some noise associated with sensors is achieved.

In comparison, the SVD denoising eliminates noise components associated with both the sensors and the pings. Working on the column covariance matrix, PCA is almost identical to SVD except that the data matrices used in PCA requires the mean of samples to be subtracted first or a mean-centered ones. However, in the studies the mean estimated deviate significantly from the true value due to the existence of unmatched samples. It was observed that the result of PCA transform was accurate as that of SVD and denoising effectiveness was slightly lower.

4.2.2.2 Adaptive Despeckling of Sonar Image Patches

The method uses the approach as in [124], where the entire image is divided into patches and to denoise an entire image, all the patches that make up the image are denoised separately. The entire image after division into non overlapping patches of size $N \times N$ is converted to 1-D training vectors which are arranged as columns so as to form a matrix of training vectors, S. The size of matrix S is $N^2 \times M$, where M is the number of patches.

If X denotes the inverse of (SS^T) i.e. $(SS^T)^{-1}$. Then each column of X denotes the principal components of the corresponding training vectors and the PC basis functions are the eigenvectors of X. For $i = 1 \ldots N^2$ and $l = 1 \ldots M$, the PC coefficients $y(i, l)$ are estimated by projecting the training vectors in S onto the PC basis functions of X. The newly generated PC coefficients helps to represent the noisy image using fewer values. Reconstruction is the reverse of the entire decomposition process. The denoised training vectors are converted back into patches, and the patches are arranged properly to obtain the denoised image.

In adaptive SVD based denoising method, the image is represented using singular values. The SVD of the covariance matrix is found out and denoising is performed on it. A sliding window is incorporated in variance calculation. Sliding window is used under the assumption that neighbouring patches will show some similarity

in terms of intensity and other factors. For finding the variance of a patch, the variances of all patches lying within a sliding window of fixed size placed about the particular patch was calculated. The size of the window was chosen in such a way that there is a reduction in the error. When the size of the window was too large, it contributed to approximation errors and when it was too small, the effect of neighbouring patches onto the specific patch under consideration was not accountable. Like the previous algorithm the entire image was divided into fixed patch size and converted to form the S matrix. The SVD of X equal to $(SS^T)^{-1}$ was calculated. SVD converged the image information into fewer coefficients with most of the information residing in the higher singular values which helped in reducing the need of large memory and complex calculations. The left singular vectors were chosen as the basis function in the algorithm developed due to the nature of the X matrix. SVD coefficients are calculated by projecting the training vectors in S onto corresponding basis function. After denoising, the denoised coefficient matrix was formed and image was reconstructed.

4.2.2.3 Block Adaptive Despeckling

In the block adaptive despeckling method, the noisy image was decomposed into patches and converted to S matrix and the complete set of training vectors were divided into blocks of fixed size. Exploiting the self-similarity of the images, the training samples of the local patch was formed by selecting a group of similar patches in its neighbourhood using block matching technique [125]. The block size was chosen in such a way that a trade of between the number of similar patches and computation speed is achieved. Too small block size resulted in complexity of computations and too large block size resulted in dissimilar patches getting grouped together and high calculation errors. After block formation, the principle components and the singular value coefficients were estimated and denoising was done at block level and reconstruction was carried out to obtain the final denoised image.

4.2.2.4 Performance Evaluation of Data Adaptive Despeckling Methods

The proposed despeckling of sonar images gave better performance compared to the existing methods available in literature. The performance of different denoising methods on real sonar image is as shown in Fig.4.7. Based on simulation analysis, the size of the image patch is set as 8×8 and the local search window in SVD method

as 8×8 and 8 adjacent patches are combined to form a block in the block based processing. In the visual comparison, the block adaptive SVD method gave better results.

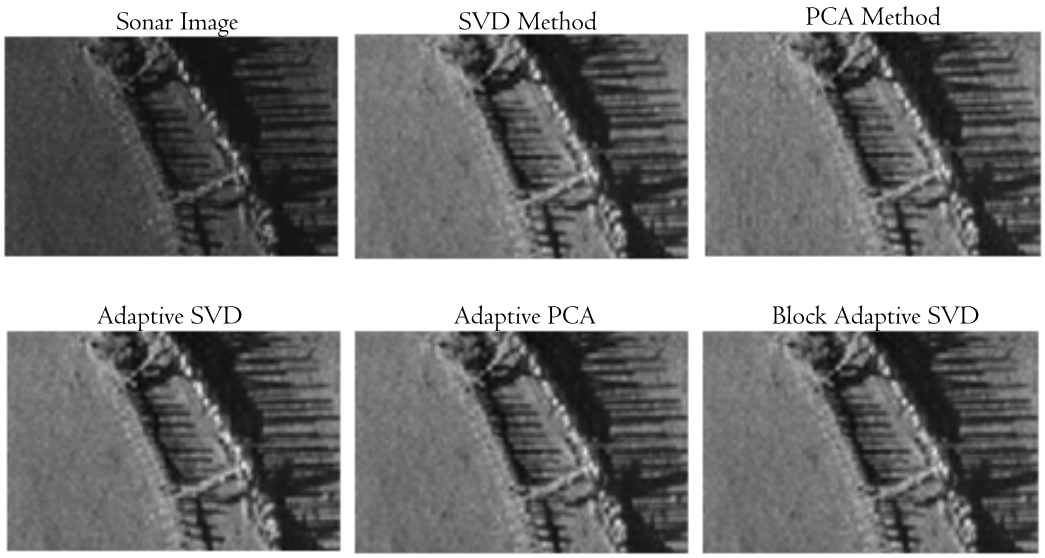

Fig. 4.7: Denoising using data adaptive transforms

SMPI index was used for simultaneous estimation of speckle suppression and mean preservation capabilities of despeckling technique and the performance evaluation of the various methods was carried out. The denoising capabilty of the proposed methods was revealed by looking at the ENL of the original and the denoised images. For an image of ENL 5.8442 the simulations were carried out. From Table 4.10 ENL is highest and SSI is lowest for the SVD denoising compared to PCA methods. This is because SVD eliminates noise components associated with both the sensors and the pings. Variance was maximum for the SVD method and so the suppression of speckle power was highest in this method. The data matrices used in PCA requires the mean of samples to be subtracted first and the mean estimated deviate significantly from the true value due to the existence of the unmatched samples and so the denoising effectiveness was slightly lower. By adaptively creating blocks of similar patches rather than adjacent patches better despeckling can be achieved in the block based method.

Table 4.10: Metric values of different despeckling methods for a sonar image of ENL 5.8442

Metric	PCA	SVD	APCA	ASVD	BAPCA	BASVD
Mean[r]	0.3492	0.33665	0.3492	0.3492	0.04134	0.04129
Var[r]	0.00965	0.00982	0.00965	0.00966	0.03964	0.03959
COV	0.1581	0.14189	0.1581	0.1581	0.15811	0.1581
ENL	40.007	49.668	40.008	40.009	40.004	40.005
SSI	0.38221	0.34302	0.3822	0.38219	0.38222	0.38221
CC	0.97535	0.98203	0.97535	0.97535	0.97535	0.97535
SMPI	103.29	102.33	103.29	103.29	103.29	103.29

A graphical comparison by metric values to grade the performance of different filtering methods is as shown in Fig.4.8.

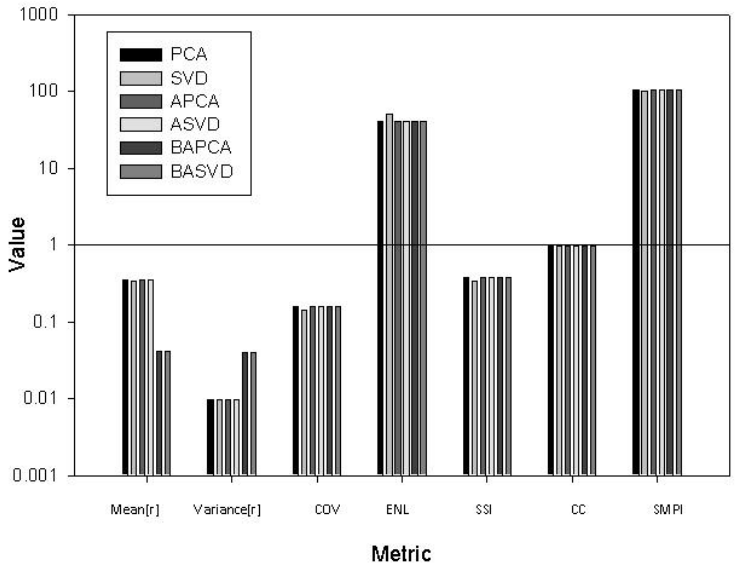

Fig. 4.8: Performance of data adaptive methods

4.2.3 Noisy Image Patch Despeckling

For all the sonar image processing like enhancement, segmentation and registration, speckle removal needs to be a pre-processing step. The heterogeneous nature of sonar images can be used for making this pre-processing stage computationally effective. For that a frame work based on blind denoising of sonar images based on sonar

image heterogeneity of the image patches is proposed. The homomorphic approach was used to convert the multiplicative signal model into an additive one. The noise level of the single noisy sonar image was estimated using a patch based algorithm and then non-blind denoising was done.

Most adaptive speckle filters are based on the local coefficient of variation, which serves to measure the heterogeneity of sonar images. However, the sensitivity of the measurements to speckle and noise of sonar images would greatly deteriorate the speckle reduction. The proposed method, presents a novel parameter for the heterogeneity measurement as a general index to quantify the sonar image heterogeneity.

The sonar image heterogeneous patch classification was based on the naive homogeneity index proposed and the despeckling filters were designed for these patches. The patches are classified into three classes, as mentioned in chapter 3 based on their texture strength. The trace of the gradient covariance matrix of each patch was calculated to obtain a naive homogeneity index τ defined for each patch and was used for patch classification. The naive homogeneity index was calculated by approximating a gamma distribution for the texture strength along with the estimated noise variance, classifies the patches into three classes and despeckling is applied on to the noisy patches only.

4.2.3.1 Heterogeneous Patch Classification using the Naive Index

The PCA estimation [126] included a patch-based noise level estimation algorithm that includes a texture strength metric which is based on the local image gradient matrix and its statistical properties to select low-rank patches without high frequency components from a single noisy image. In the patch based approach, images are decomposed into a number of patches from an input noisy image in a raster scan form. The patch with the smallest standard deviation among decomposed patches has the least change of intensity. The data model of the patches is eq.4.8

$$g'_i = f'_i + u'_i \quad i = 1, 2, 3, M \tag{4.8}$$

where M is the number of patches, f'_i is the i^{th} noise-free image patch with size $N \times N$ written in a vectorized format, and each patch is defined by its center pixel. g'_i is the observed vectorized patch corrupted by noise vector u'_i with zero-mean and variance σ^2.

The minimum variance direction [127] is the eigenvector associated to the mini-

mum eigenvalue of the covariance matrix defined by eq.4.9

$$\Sigma_{g'} = \frac{1}{M}\Sigma_{i=1}^{M} g'_i g'^T_i \tag{4.9}$$

where Σ'_g is the covariance matrix of the noisy patch g' is in eq.4.10.

$$\lambda_{min}(\Sigma_{g'}) = \lambda_{min}(\Sigma_{f'}) + \sigma^2 \tag{4.10}$$

where $\lambda_{min}(\Sigma)$ represents the minimum eigenvalue of the matrix Σ. The noise level was estimated by taking advantage of the properties of natural image. Because of the redundancy of natural images, the data of natural images span only low-dimensional subspace. If the data of patches $g'_i \in N \times N$ span a subspace whose dimension is smaller than $N \times N$, it is a low-rank patch.

To analyze the image structure and to select suitable patches from the noisy image, local variance of image patch is widely used. [128] proposed an algorithm in which the patches with the smallest local variance are assumed to be homogenous patches. In [129] a number of patches with largest variances are discarded. This method is simple and fast, but tends to overestimate the amount of noise. The reason is that for the rich textured images or images with high noise level, patches with the smallest local variance are not always homogenous patches.

In [130], it is reported that image structure can be measured effectively by the gradient covariance matrix. Assuming an image patch g'_i, its $N^2 \times 2$ gradient matrix $G_{g'_i}$ can be expressed as eq.4.11

$$G_{g'_i} = \left[D_h g'_i D_v g'_i\right] \tag{4.11}$$

where D_h and D_v represent the matrices of horizontal and vertical derivative operators, respectively. The $N^2 \times N^2$ matrices D_h and D_v are Toeplitz matrices [131] derived from gradient filter. The gradient covariance matrix $C_{g'_i}$ for the image patch g'_i is defined as eq.4.12

$$C_{g'_i} = G^T_{g'_i} G_{g'_i} \tag{4.12}$$

where T denotes the transpose operator. Much information about the image patch can be reflected by the gradient matrix $G_{g'_i}$ or the gradient covariance matrix $C_{g'_i}$. The dominant direction and its energy can be measured using the eigenvectors and eigenvalues of $C_{g'_i}$ [132].

The trace, sum of all eigenvalues of the covariance matrix reflects the texture strength of that patch. A larger trace reflects a richer texture. Define the texture strength ξ_i as eq.4.13

$$\xi_i = tr(C_{g_i'}) \tag{4.13}$$

where $tr(\Delta)$ denotes the trace operator. It might be readily apparent that a smaller trace value indicates a smoother or the weaker textured patch. The low-rank patches without high frequency components in the noise-free images can be distinguished easily by thresholding the texture strength. Unfortunately, the gradient matrix is sensitive to noise, so the texture strength is affected easily by the noise. The texture strength of the patch becomes as in eq.4.14

$$\xi(n) = tr(C_{g'}) \tag{4.14}$$

To analyze the statistical properties of texture strength, approximate the distribution of $\xi(n)$ by the gamma distribution to simplify the problem. The pdf of $\xi(n)$ can be derived as in eq.4.15

$$\xi(n) \approx Gamma\left(\frac{N^2}{2}, \frac{2}{N^2}\sigma^2 tr(D_h^T D_h + D_v^T D_v)\right) \tag{4.15}$$

where $Gamma(\alpha, \beta)$ represents a gamma distribution with the shape parameter α and scale parameter β. In addition, σ is the standard deviation of the Gaussian noise, N^2 represents the number of pixels in the patch, and D_h, D_v are matrices derived from the gradient filter. If the texture strength of that patch is less than the threshold τ , then the null hypothesis is accepted and that patch can be regarded as the weak textured patch. The threshold τ can be expressed as a function of the given significant level δ and noise level σ, as in eq.4.16,

$$\tau = \sigma^2 F^{-1}(\delta, \frac{2}{N^2}\sigma^2 tr(D_h^T D_h + D_v^T D_v)) \tag{4.16}$$

where $F^{-1}(\delta, \alpha, \beta)$ is the inverse Gamma cumulative distribution function and δ is the confidence level. If the points within the patch share a common intensity value, the image patch is assumed to be pure flat patch. The natural image patches usually contain some weak textures and flat patches can be selected and then the confidence level δ can be set very close to 1.

In the proposed work, a texture strength metric which was based on the local

image gradient matrix and its statistical properties to select low-rank patches was used. For estimating the noise variance of the sonar image the patches of size 7×7 were used. Each patch is assumed to be corrupted by additive Gaussian noise vector with zero-mean and a variance. The minimum variance direction is the eigenvector associated to the minimum eigenvalue of the covariance matrix of the patch. The minimum eigenvalue of the covariance matrix of the noisy patch $\lambda_{min}(\Sigma_{g'})$ is the sum of the minimum eigenvalue of the covariance matrix of the noise free patch $\lambda_{min}(\Sigma_{f'})$ and the Gaussian noise variance σ^2. Because of the redundancy of the sonar images, minimum eigenvalue of the covariance matrix of the noise free patch was assumed as zero. So the noise variance is equal to the minimum eigenvalue of the covariance matrix of the noisy patch as in eq.4.17.

$$\sigma^2 = \lambda_{min}(\Sigma_{g'}) \tag{4.17}$$

The small patches were extracted by sliding square windows. Naturally, ignoring boundary effects arising from the finite nature of the window, a flat patch remains unchanged. When the texture strength value was less than τ calculated using eq.4.16, it was classified as homogeneous patch and a normal averaging filter was applied to these type of patches. The patches with texture strength $\sqrt{3}\tau$ is classified as belonging to the target patches and were left unprocessed. The patches having texture strength lying between these two ranges were considered as the intermediate patches and needs to be despeckled.

4.2.3.2 Denoising of the Selected Patches

To check whether to the given patch, the averaging filter need to be applied or to be despeckled or to be left unprocessed, the homogeneity index of each patch was calculated. From the gradient covariance matrix of the particular patch, obtain the trace of the square root of the eigenvalues of the covariance matrix. Then the homogeneity index for each patch is the product of the above value with the number of image patches. For despeckling the selected patches, the patch based method of the data adaptive transform method was used.

4.2.3.3 Results After Adoption of the Naive Index

The experimental results proved that introduction of the proposed index for denoising brought in an overall improvement in terms of visual quality. The proposed technique not only produced smoother images in homogenous areas but also preserve edges. In the existing despeckling filters the contours were smoothed excessively and the edges tended to blur while removing the speckle noise. The proposed technique outperformed conventional despeckling techniques in terms of edge preservation as well as undesired artifacts as can be found in the visual comparison of the method with the existing methods.

The performance was evaluated for varying patch sizes and the optimum patch size for despeckling was found to be image dependent and had a direct dependence on the homogeneity index for patch classification. Small patch size selection increases the computational complexity, as more processing is required if the whole image need to be processed by the patch based method. The different *without-reference* image performance evaluation criterion was used to evaluate the proposed method. The qualitative results of Fig.4.9 shows that for the selected image, the better visual results were for the patch of size 20. The numerical results in Table 4.11 and the graphical comparison in Fig.4.10 substantiated the visual results.

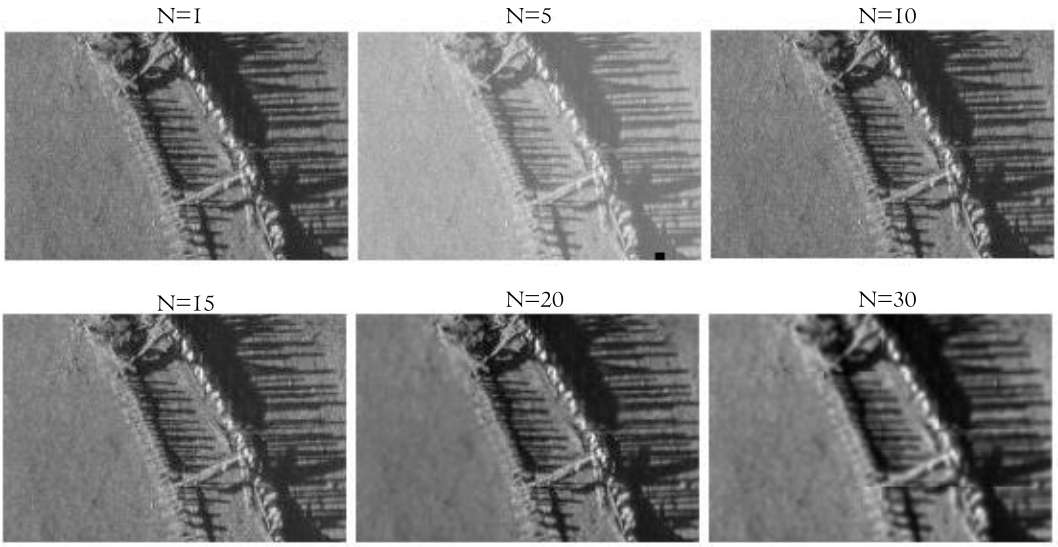

Fig. 4.9: Denoising by varying patch size

Based on the conclusions from the above said results, with the patch size 20 the proposed method can eliminate speckle without distorting useful image information

Table 4.11: Metric values for varying patch size

Patch Size	5	10	15	20	30
Patches	864	216	96	54	24
LowTh	684.9246	1.63E+03	2.98E+03	4.63E+03	7.72E+03
HighTh	1.19E+03	2.82E+03	5.16E+03	8.03E+03	1.34E+04
ENL	138.2733	49.8751	50.2116	40.5414	30.4516
COV	0.085	0.1416	0.1411	0.1571	0.1812
BIAS	0.2799	0.1909	0.192	0.1913	0.2005
SSI	0.2056	0.3423	0.3412	0.3797	0.4381
CC	0.9629	0.9819	0.9803	0.9673	0.912

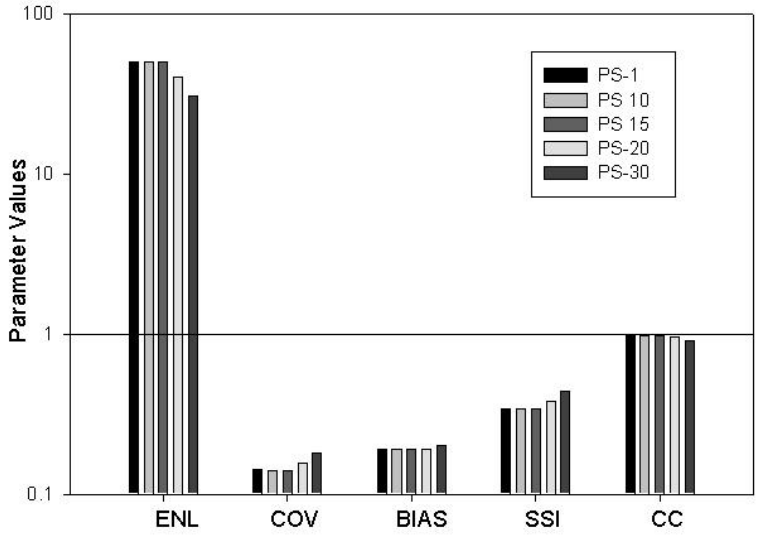

Fig. 4.10: Performance with varying patch size

and without destroying the important image edges as shown in the Fig.4.11. For the selected image, the patch size 20 was giving better visual appearance. Also with this patch size, the computations required is not much as that of other smaller patches. The proposed filter outperformed the conventional and non conventional speckle reducing filters in terms of ENL and SSI. The visual results are supported by the quantitative results in Table 4.12 and the Fig. 4.12.

The presented method uses a novel parameter for the heterogeneity measurement as a general index to quantify the sonar image heterogeneity. The performance of the despeckling methods was sensitive to the noise level estimation methods used.

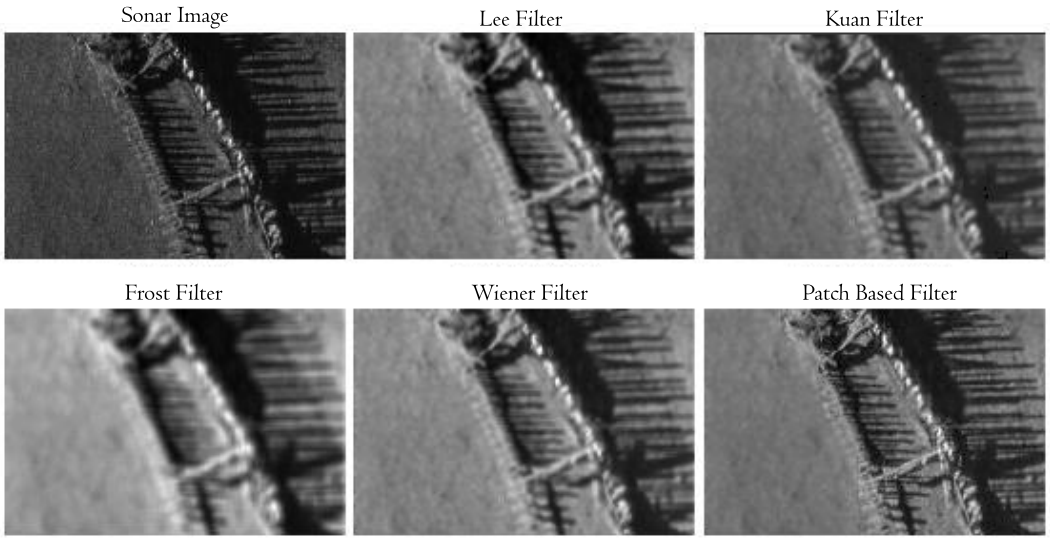

Fig. 4.11: Existing despeckling methods compared with patch based for a patch size 20

Table 4.12: Metric values for existing despeckling techniques and the patch based method of patch size 20

Filter	Lee	Kuan	Frost	Weiner	Proposed
ENL	30.4345	7.6212	25.2995	35.4564	40.5414
COV	0.1813	0.3622	0.1988	0.1679	0.1571
BIAS	0.2008	0.2008	0.2301	0.1944	0.1913
SSI	0.4382	0.8757	0.4806	0.406	0.3797
CC	0.9086	0.8983	0.8449	0.9199	0.9673

The patch based noise level estimation method and a patch based homogeneity index calculation used gave the add on advantage. The visual results as seen in Fig.4.12, showed the effectiveness of the use of new speckle reduction algorithm. Experimental results substantiate the effectiveness of using the new homogeneity index instead of the classical one based on coefficient of variation as in the Lee filter. The SMPI index is considered only when ENL and SSI are not considered as reliable measures when the despeckling algorithm overestimates the mean value.

4.3 Spatial Domain

In the spatial domain, a linear state estimation method like the Kalman filter based method was used for side scan sonar image estimation. Side scan sonars are used

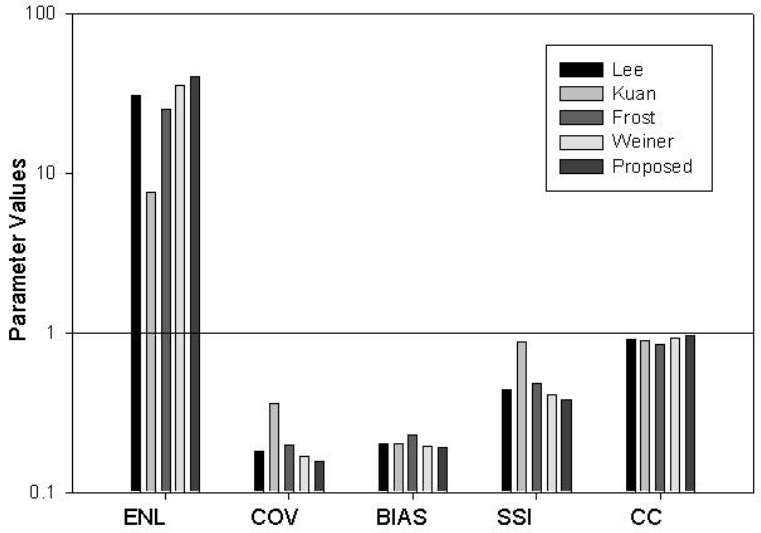

Fig. 4.12: Performance of patch based despeckling for a patch size 20

to provide qualitative images representing large areas of the seabed and the objects on it. The main characteristic features of side scan sonar are that it is a towed, sideways looking device. As the towfish is towed through the water, the lateral sound beams progressively scan a swath of the seabed, while the recorder produces a line-by-line record of the backscattered signal [133]. The visual record produced by a side-scan sonar is called a sonograph. The homomorphic approach was applied on the reflectivity domain relation to obtain the observation model for the Kalman filter.

Kalman estimation is used to estimate the original image from its degraded observations. When the observation is linearly related to state, and the modeling errors are Gaussian, then the Kalman filter [134] provides an optimal estimate of the state. But in practice, an image sensor can possess nonlinear characteristics. The proposed Kalman filter based speckle noise removal in sonar images exploits the basic principle of sonar image formation in a side scan sonar image.

4.3.1 SSS Image Linear Estimation

The one dimensional Kalman state estimation was extended to the two dimensional sonar image. The 2D Kalman state estimation complexity was avoided in the sonar

image restoration method as it exploited the independence in the speckle characteristics of each scan lines of the side scan imaging technology. Since Kalman estimation of the images deals with 2D data, the computation and the memory requirements increase drastically. In the proposed approach a one step pixel prediction for the sonar image estimation is employed. The 2D image processing is done similar to a 1D signal processing manner considering each row as a 1D signal. This is possible because of the line scanning characteristics of side scan sonar images. The assumption that each scan lines are independent, they can be processed row by row. So the dependency of the pixel elements in the single row is considered for the estimation. Otherwise all the four pixel neighbors effects are required to be considered for the estimation of the next pixel value which is a very tedious task.

4.3.1.1 SSS Image State Space Representation

The interpretation of side scan sonar images, or records, requires an understanding of the phenomena which result in the generation of the images. Due to the line scanning basis of the side scan sonar, the lines of the image are unrelated in terms of speckle noise and can be treated separately. The images are scanned from left to right, advance one line and then repeat. At any point in the image, some points represents the past, one point represent the present, and the remaining points represent the future. Due to the characteristics of side scan sonar image formation process, as the speckle noise effect on each scan line is independent, only the observed pixel values of the respective scan lines is used for estimating the true pixel value of the image. Thus to compute the present output given the present input only the pixel values of the respective row is used which greatly reduce the computation and memory requirements. With a model for the degradation process, the inverse process can be applied to the image for its restoration.

The proposed method assumed the signal-independent additive noise model, where the modeling errors were Gaussian and the observation is linearly related to the state. This model is obtained after applying a homomorphic filtering to transform the original multiplicative noise model into an additive one. The problem of despeckling now gets modified as rejection of an additive noise. The Kalman filter with the set of mathematical equations provided an efficient computational recursive means to estimate the state of a process, in a way that minimized the mean of the squared error. The filter supported the estimations of past, present, and even future

states, even with an unknown precise nature of the modeled system.

The Kalman filter achieves its optimal performance when the *a priori* measurement noise is equal to the actual measurement noise. There are different methods for estimating the actual observation noise of the system. The estimate of the actual observation noise is used to adapt the Kalman filter to improve its performance [135].

The Kalman filter addresses the general problem of trying to estimate the state of a $x \in R^n$ discrete-time controlled process that is governed by the linear stochastic difference equation. In side scan sonar image case, model each row of data by a state space equation as in eq.4.18,

$$x_{k+1} = A_k x_k + B w_k + u_k \tag{4.18}$$

with a measurement $z \in R^m$ that is eq.4.19,

$$z_k = H_k x_k + v_k \tag{4.19}$$

where
x_k is the true pixel intensity
z_k is the measured pixel intensity
w_k is a random forcing function
v_k is random measurement noise.

The random variables u_k and v_k represent the process and measurement noise respectively. They are assumed to be independent of each other, white, and with normal probability distributions.

The process noise covariance Q and measurement noise covariance R matrices were assumed to be constant. The matrices A and H were determined from the piecewise constant assumption of the data and first order or second order models were used.

4.3.1.2 Image Estimation based on Linear State Space Concept

In the Kalman filtering frame work, there are two occurrences to propagate the state variable through the transformation. One is while in predicting the new state from the past and the other is while obtaining the observation from the predicted state.

The algorithm flow is as follows:
Define all state definition fields: A,B,H,Q,R

Define initial state estimate: x,P
Obtain observation and control vectors: z,u
Call the filter to obtain updated state estimate: x,P
Return to step to obtain z,u, and repeat.

Let $\hat{x}_k^- \in R^n$ to be the *a priori* state estimate at step k given knowledge of the process prior to step k , and $\hat{x}_k \in R^n$ be the *a posteriori* state estimate at step k given measurement z_k. Then the *a priori* and *a posteriori* estimate errors are as in eq.4.20 and eq.4.21 respectively.

$$e_k^- \equiv x_k - \hat{x}_k^- \tag{4.20}$$

$$e_k \equiv x_k - \hat{x}_k \tag{4.21}$$

The *a priori* estimate error covariance is then eq.4.22,

$$P_k^- = E[e_k^- e_k^{-T}] \tag{4.22}$$

and the *a posteriori* estimate error covariance is eq.4.23,

$$P_k = E[e_k e_k^T] \tag{4.23}$$

In deriving the equations for the Kalman filter, begin with the goal of finding an equation that computes an *a posteriori* state estimate $\hat{x}_k$ as a linear combination of an *a priori* estimate $\hat{x}_k^-$ and a weighted difference between an actual measurement z_k and a measurement prediction $H_k\hat{x}_k^-$ as in eq.4.24,

$$\hat{x}_k = \hat{x}_k^- + K(z_k - H_k\hat{x}_k^-) \tag{4.24}$$

The difference $(z_k - H_k\hat{x}_k^-)$ is called the measurement innovation, or the residual. The residual reflects the discrepancy between the predicted measurement $H_k\hat{x}_k^-$ and the actual measurement z_k. A residual of zero means that the two are in complete agreement. The $n \times m$ matrix K is chosen to be the gain or blending factor that minimizes the *a posteriori* error covariance.

The Kalman filter estimates the pixel value at a location and obtains the feedback in the form of noisy measurements. The time update equations also called the

predictor equations are as in equations 4.25 and 4.26:

$$\hat{x}_{k+1}^{-} = A_k \hat{x}_k + B u_k \tag{4.25}$$

$$P_{k+1}^{-} = A_k P_k A_k^T + Q_k \tag{4.26}$$

The measurement update equations or the corrector equations are eq.4.27, eq.4.28 and eq.4.29:

$$K_k = P_K^{-} H_k^T (H_k P_k^{-} H_k^T + R_k)^{-1} \tag{4.27}$$

$$\hat{x}_k = \hat{x}_k^{-} + K(z_k - H_k \hat{x}_k^{-}) \tag{4.28}$$

$$P_k = (1 - K_k H_k) P_k^{-} \tag{4.29}$$

The $n \times n$ matrix A in the difference equation relates the state at the previous time step k to the state at the current step $k+1$, in the absence of either a driving function or process noise. In practice A might change with each time step, but here it is assumed to be a constant. The $n \times l$ matrix B relates the optional control input $u \in R^l$ to the state x. The $m \times n$ matrix H in the measurement equation relates the state to the measurement z_k. In practice H might change with each time step or measurement, but here it is again assumed to be a constant. The estimated pixel value of the first row of the real side scan sonar image is shown in Fig.4.13.

4.3.1.3 Despeckling Assessment

The despeckling results of the proposed technique and comparison methods for two side scan sonar images are given in Fig.4.14 and Fig.4.15.

The assessment parameters ENL, SSI, CC and SMPI are applied to the whole image. The quantitative results in Table4.13 and Table4.14 clearly reveal that the proposed method can eliminate speckle without distorting useful image information and without destroying the important image edges. An objective measure of the homogeneity degree of a region is the enhancement of the ENL. It is defined by the ratio of the square of the mean and the variance of the pixels situated in the considered region. The index ENL is suitable for evaluating the level of smoothing in homogeneous areas, where the scene variation is supposed to be negligible with respect to speckle noise fluctuations. This has been achieved with the homomorphic transformation and so ENL is preferred over the index SMPI in such cases.

When the log transformation is applied on the sonar image to obtain the signal-

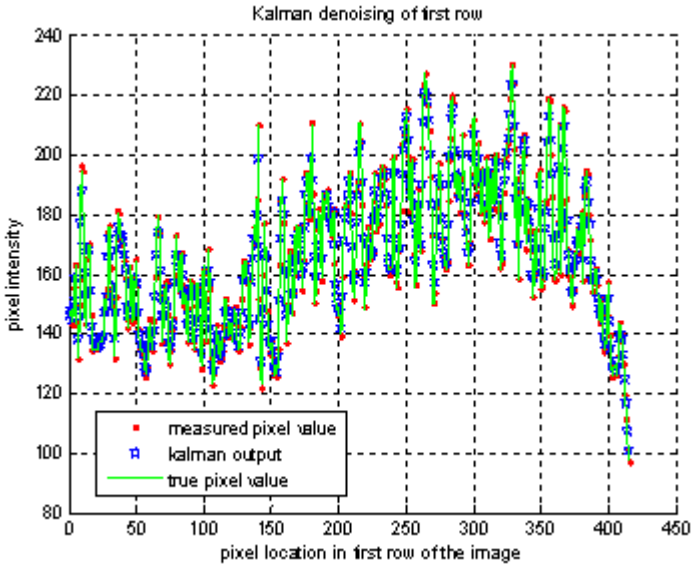

Fig. 4.13: Estimated pixel value of the first row of the side scan sonar image

independent additive noise model results in very high values of ENL and SMPI compared to the other existing methods in the literature, which mostly uses the signal-dependent noise models. The homomorphic approach introduces an undesired bias. The unbiased estimate becomes a biased estimate after this transformation and doing this transformation alone results in an increase in the ENL and SMPI. The proposed filter has a higher ENL than others because it always use all the pixels in the filtering window and outperformed the conventional and non conventional speckle reducing filters in terms of ENL and SSI. Without-reference indexes uses specific statistical hypotheses on the signal model and is strongly dependent on the degree of scene heterogeneity. So a supervised selection of the most appropriate areas for the computation of a specific index, e.g., homogeneous areas, is required. The numerical results are further supported by qualitative examination.

The quantitative results in Table4.15 and Table4.16 shows metric values considering a homogeneous area of 25×25 of the two sonar images considered.

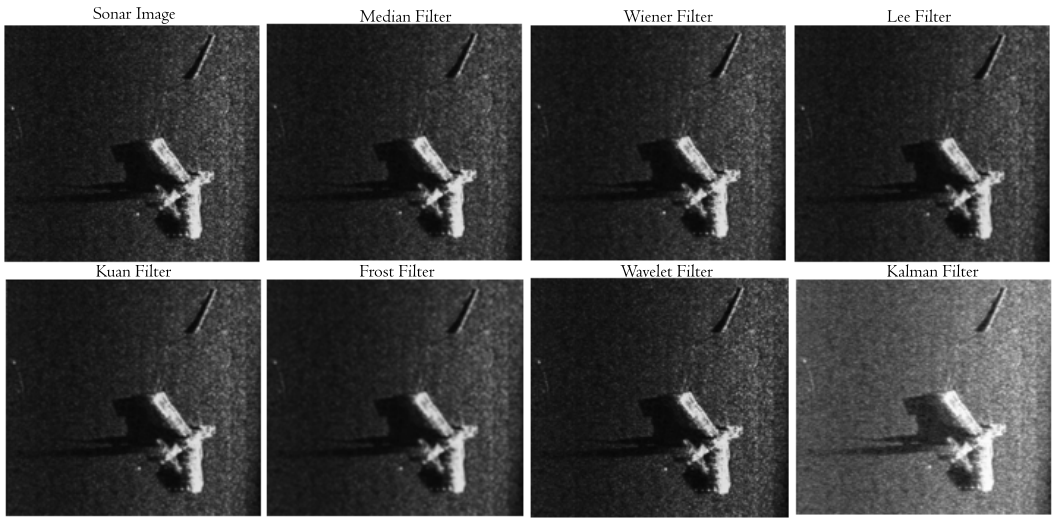

Fig. 4.14: Visual comparison of despeckling techniques for a sonar image of ENL 1.3691

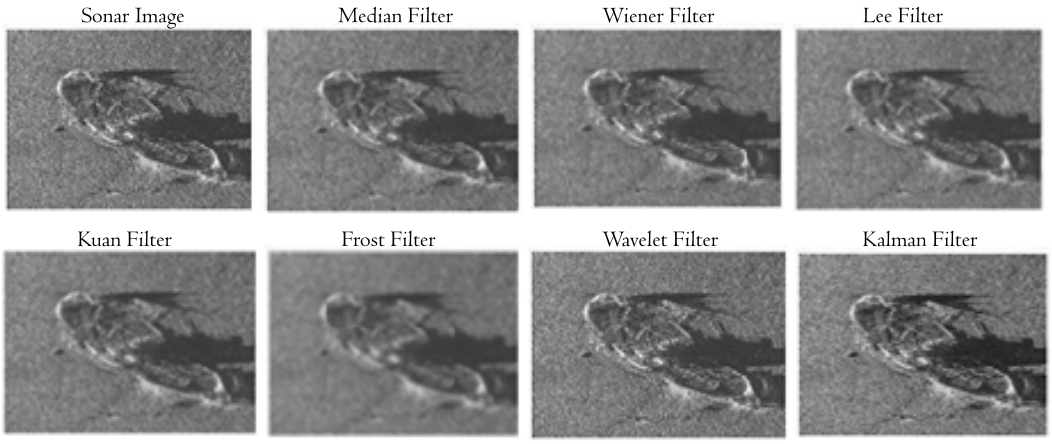

Fig. 4.15: Visual comparison of despeckling techniques for sonar image of ENL 6.5877

4.4 Results and Discussions

The despeckling of sonar images based on signal-independent additive models have been implemented and compared with the existing ones. The despeckling results of the different methods proposed need to be analyzed and compared. This analysis is performed by applying these methods to the same image.

Table 4.13: Metric values for despeckling methods for sonar image of ENL 1.3691

Method	Median	Wiener	Lee	Kuan	Frost	SRAD	Wavelet	Proposed
ENL	1.5234	1.5499	1.7228	1.7053	1.8478	1.5609	1.3962	34.7682
SSI	0.948	0.93985	0.8914	0.89602	0.86078	0.93653	0.99031	0.1984
CC	0.91303	0.97265	0.9178	0.9145	0.90193	0.97309	0.99518	0.9344
SMPI	1.5177	0.16073	4.30E-04	0.12784	0.02845	0.91512	2.11E-07	80.9785

Table 4.14: Metric values for despeckling methods for sonar image of ENL 6.5877

Method	Median	Wiener	Lee	Kuan	Frost	SRAD	Wavelet	Proposed
ENL	7.5625	7.9319	8.4279	9.1911	9.5104	7.2474	6.7802	30.554
SSI	0.9333	0.91134	0.88412	0.84661	0.8323	0.9534	0.9857	0.46434
CC	0.9453	0.95838	0.9019	0.79183	0.8644	0.98209	0.9932	0.97012
SMPI	0.17	0.44382	0.40822	2.5344	0.4622	0.94577	0.00001	29.192

4.4.1 Analysis of Different Additive Noise Model Methods

In order to get the additive noise model for the speckle affected sonar images, the homomorphic approach is applied on the reflectivity domain of the sonar image. The model thus obtained for the filter is a signal independent additive speckle scene-model, which can be despeckled by transform domain or spatial domain methods.

In the transform domain, an image independent transform like the multiresolution method with the 2D wavelet transform is employed. The noise power reference and an estimation of the standard deviation of original noise must be known for the despeckling using the wavelet denoising. The wavelet transform method extract edges from coarse scales to fine scales and by applying the wavelet shrinkage techniques despeckling of the sonar image is achieved. However such denoising in sonar images tend to blur the edges while removing the speckle noise as depicted in the results.

Most of the despeckling algorithms smooth excessively the contours when they are not sufficiently contrasted as in the case of sonar images and remove the edges, resulting in unreliable loss of information. Thus in the second method of the transform domain, an image dependent transform which make uses the principal component of the image for signal representation has been used. The PCA denoising algorithm uses a 2-D basis sets having the vectors lined up along edges, and not across them. In such cases unlike the fixed basis analysis, the high frequency coefficients caused by

Table 4.15: Metric values considering a homogeneous area of 25×25 with an ENL 8.6558

Method	Median	Wiener	Lee	Kuan	Frost	SRAD	Wavelet	Proposed
ENL	23.993	30.019	29.88	29.88	58.48	21.196	9.6124	195.65
SSI	0.9480	0.9399	0.8914	0.8960	0.8608	0.9365	0.9903	0.1984
CC	0.9130	0.9727	0.9178	0.9145	0.9019	0.9731	0.9952	0.9344
SMPI	0.5414	0.0469	0.0056	0.0056	0.0137	0.319	2.51E-05	149.58

Table 4.16: Metric values considering a homogeneous area of 25×25 with an ENL 54.649

Method	Median	Wiener	Lee	Kuan	Frost	SRAD	Wavelet	Proposed
ENL	177.66	246.91	246.2694	246.27	561.4	288.37	64.925	353.38
SSI	0.9333	0.91134	0.8841	0.8467	0.8323	0.9534	0.9857	0.46434
CC	0.9453	0.9584	0.9019	0.7918	0.8644	0.9821	0.9932	0.97012
SMPI	0.2222	0.2478	0.0956	0.0956	0.0731	0.4661	8.68E-05	24.368

the edges are much smaller and hence the edges are retained. This is the advantage of using a data adaptive transform method over the data independent transform methods. For the blind denoising, the noise variance of the principal component coefficients for each patch is determined using the patch based estimation method and the coefficients are denoised using the minimum mean square estimator. The data adaptive transform method is extended on to the noisy image patch despeckling by using the naive homogeneity index proposed. The method has the benefit of applying the despeckling method on to the specified region of interest, resulting in the computational complexity reduction. Among the classified patches the complicated time consuming despeckling algorithms need to be applied to the textured patches, while the simple averaging algorithm can be applied on the homgeneous patches and can leave the target patches unprocessed justifying the computation reduction. The specified region can be the textured regions or can define by a expert sonar interpreter.

In spatial domain, the side scan sonar image with the signal-independent additive noise model representation has the observation linearly related to pixel state and Gaussian modeling errors. The noise variance of the image for the denoising is estimated along with estimation process. Assuming the independence of the pixel values of each scan lines of the sonar image, a linear state estimator like the Kalman filter can provide an optimal estimate for the next pixel state from the current state.

The same linear state estimation concept is extended to the successive scan lines of the sonar image. In this manner the well appreciated 1D Kalman estimation is applied to estimate the original image from speckle degraded observations.

The comparison of the various despeckling methods using the signal independent additive speckle-scene model has been applied and the resulting sonar images are shown in Fig.4.16. The size of image patch is set to be 8×8 and the local search window in SVD method is fixed as 8×8 and 8 adjacent patches are combined to form a block in block based processing.

Variance is maximum for the SVD method and so the suppression of speckle power is highest in this method. The small patches are extracted by sliding square windows and is used under the assumption that neighbouring patches will show some similarity in terms of intensity and other factors. The size of the window was chosen in such a way that there is a reduction in the error. When the size of the window was too large, it contributed to approximation errors and when it was too small, the effect of neighbouring patches onto the specific patch under consideration was not accountable. The patch classification can be done by using the naive homogeneity index introduced. The various non-reference metric value comparison is shown in Table 4.17 and the graphical comparison is depicted in Fig.4.17.

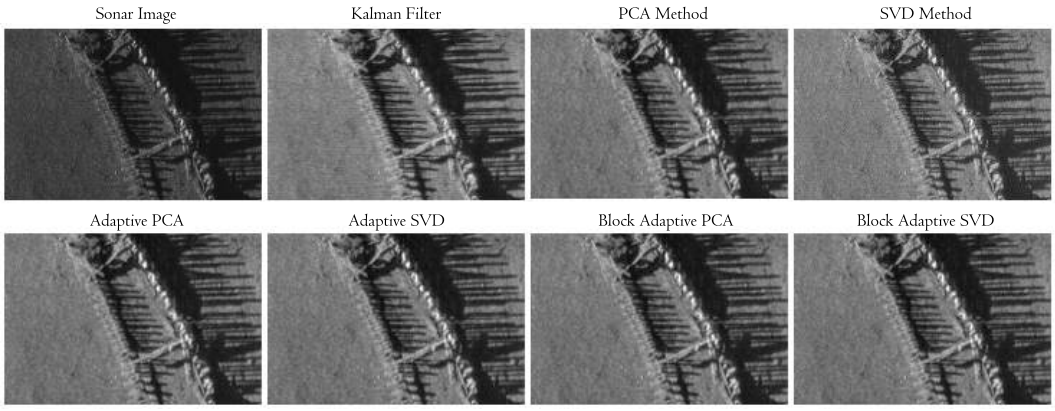

Fig. 4.16: Visual comparison of methods using different additive noise model

4.5 Summary

This chapter deals with different despeckling methods in both transform and spatial domains with the signal-independent additive noise model followed by the results and

Table 4.17: Metric value comparison for the despeckling using different additive noise model

Method	PCA	SVD	APCA	ASVD	BAPCA	BASVD	HomPCA	KF
ENL	40.007	49.668	40.008	40.008	40.004	40.005	40.5414	36.939
SSI	0.38221	0.34302	0.3822	0.3822	0.38222	0.38221	0.3797	0.39776
CC	0.97535	0.98203	0.97535	0.97535	0.97535	0.97535	0.9673	0.95357
COV	0.1581	0.14189	0.1581	0.1581	0.15811	0.1581	0.1571	0.34352
SMPI	103.29	102.33	103.29	103.29	103.29	103.29	101.571	114.73

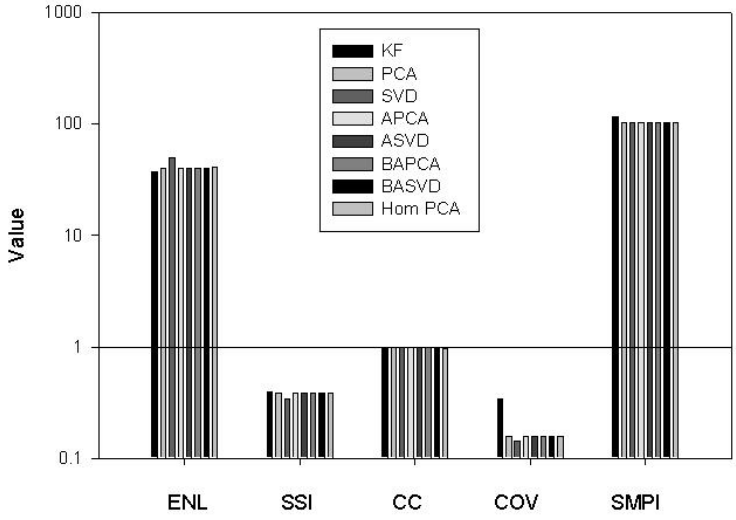

Fig. 4.17: Graphical comparison to grade the performance of despeckling using different additive noise model

discussions of the methodologies adopted. The result of PCA transform methods' effectiveness is slightly lower compared to SVD denoising as SVD eliminates noise components associated with both the sensors and the pings. The patch based filter outperformed the conventional and non conventional speckle reducing filters in terms of ENL and SSI. The one step pixel prediction method uses 1D Kalman estimation effectively in estimating the row pixel values and thereby avoiding the complexity of the estimation in 2D. The log transformation performed in the homomorphic approach to obtain the signal-independent additive noise model leads to very high values of ENL and SMPI compared to the other existing signal-dependent noise models methods in literature.

Chapter 5

Multiplicative Noise Model Analysis

In this chapter, a multiplicative noise model is assumed and the sonar image is estimated in both the transform domain and the spatial domain. For the multiplicative noise model, in the transform domain a mixed noise removal based on probabilistic patch based processing is employed and in the spatial domain, the fractional integral mask based method and an unscented kalman filter estimation method is adopted.

5.1 Introduction

The model in the literature on despeckling is the multiplicative speckle noise model, which expresses the observed intensity as the product of the scene signal intensity and speckle noise intensity. The model relates the two entities, at each pixel, as a function of speckle noise. The speckle fading term is independent of the noise free reflectivity. This model formulates speckle as a multiplicative modulation of the scene reflectivity. Hence, the speckle effects are more pronounced in a high intensity area than in a low intensity area. The non-homomorphic approach followed avoids the undesired bias affect occurring. The signal can be processed in the non-homomorphic transform domain or in the non-homomorphic spatial domain.

5.2 Transform Domain

In the transform domain, a data adaptive mixed noise removal in sonar images is implemented. The additive Gaussian noise and multiplicative speckle removal is done by exploiting the sonar image local sparsity and non local similarity in probability distribution respectively, which efficiently characterize the statistical properties of sonar image.

5.2.1 Mixed Noise Removal by Processing of Patches

A frame work for mixed noise removal in sonar images was done assuming the sonar images being degraded by multiple noises which has adverse impact on detection and classification performance. The multiple noise in sonar images are the additive Gaussian noise and the speckle noise. Classical filters are primarily designed for additive noise suppression. Some of the speckle suppression methods for sonar image denoising takes a homomorphic approach which transform the multiplicative noise model into an additive one by considering the logarithm of the image and assumes the noise is Gaussian. However, not much work has been designed to effectively eliminate mixed noise due to the distinct characteristics of both types of degradation processes. The methods developed for Gaussian noise cannot effectively suppress speckle effect because they interpret the noisy pixels as edges to be preserved, whereas the approaches for despeckling will retain most Gaussian noise in the restored images leading to grainy, visually disappointing results.

A methodology for patch based denoising and its application to additive Gaussian and multiplicative speckle noises was adopted. The adaptive processing of local patches was used to remove the additive Gaussian noise whereas the multiplicative speckle noise which is normally Rayleigh distributed as gathered from the literature review was removed by processing of non local patches. The PCA and SVD methods were used for denoising the noisy image patches and blocks of patches. A weighted maximum likelihood denoising of the non local patches reduced the speckle effect. Simulations conducted on sonar images and the results substantiated the effectiveness of mixed noise removal in sonar images. The different methods were compared by using different *without-reference* image performance evaluation criteria.

5.2.1.1 Sonar Image Noisy Signal Model

The degradation model to describe the multiple noise affected sonar images is $y = g + v$, where y is the observed image intensity, $g = fu$ denotes the multiplicative noise model with f, the corresponding scene reflectivity, u the multiplicative speckle fading term statistically independent of f, and v denotes the additive white Gaussian noise with mean zero and unknown variance σ_v^2.

In the two phase patch based mixed denoising algorithm, the additive white Gaussian noise is removed by the sparse approximation of local image patches in the first phase and in the second phase, despeckling is done on non local patches formed by exploiting the similarity between noisy patches defined from the noise distribution.

5.2.1.2 Denoising by Processing of Local Patches

Because of the redundancy of sonar images, the data of natural images span only in low-dimensional subspace. If the data of patches $g_i \in R^{N\times N}$ span a subspace whose dimension is smaller than $N \times N$, then they are called low-rank patches. The noise level of the additive Gaussian noise is estimated from the selected patches using PCA. With the available sonar image, the noise level estimation algorithm estimates the unknown standard deviation σ_v of the image. The PCA estimation includes a patch-based noise level estimation algorithm that includes a texture strength metric which is based on the local image gradient matrix and its statistical properties to select low-rank patches without high frequency components from a single noisy image.

In patch-based approaches images are decomposed into a number of patches from an input noisy image in a raster scan form. The patch with the smallest standard deviation among decomposed patches has the least change of intensity. The data model of the patches is in eq.5.1,

$$y_i = g_i + v_i \qquad i = 1, 2, 3, M \tag{5.1}$$

where M is the number of patches, g_i is the i^{th} noise-free image patch with size $N \times N$ written in a vectorized format, and each patch is defined by its center pixel. y_i is the observed vectorized patch corrupted by noise vector v_i with zero-mean and variance σ_v^2.

The minimum variance direction is the eigenvector associated to the minimum

eigenvalue of the covariance matrix defined by eq.5.2,

$$\Sigma_y = \frac{1}{M}\Sigma_{i=1}^{M} y_i y_i^T \tag{5.2}$$

where Σ_y is the covariance matrix of the noisy patch y_i. The $\lambda_{min}(\Sigma)$ represents the minimum eigenvalue of the matrix Σ is in eq.5.3,

$$\lambda_{min}(\Sigma_y) = \lambda_{min}(\Sigma_g) + \sigma_v^2 \tag{5.3}$$

where Σ_g is the covariance matrix of the additive noise removed patch g_i.

Consequently, the minimum eigenvalue of the covariance matrix $\lambda_{min}(\Sigma_g)$ is assumed as zero. Since Gaussian noise has the same power in every direction and all eigenvalues are the same, it should be able to estimate the noise level from the subspace spanned by the eigenvectors of the covariance matrix $\lambda_{min}(\Sigma_y)$ with zero eigenvalues. For blind denoising, the eq.5.4 gives the additive noise variance σ_v^2 of the image determined using the patch based estimation method .

$$\sigma_v^2 = \lambda_{min}(\Sigma_y) \tag{5.4}$$

Then the non-blind denoising is performed.

With the additive Gaussian noise model of the sonar image, denoising is done by decomposing the noisy image patches and blocks of patches using Principal Components or SVD coefficients, estimating the clean coefficients, and reconstructing the final image. Estimate σ_g^2 using eq.5.5, the noise variance of the PC coefficients for each patch using the maximum likelihood estimator.

$$\sigma_g^2 = max\left[0, \frac{1}{M}\sum_i y_i^2 - \sigma_v^2\right] \tag{5.5}$$

Then denoise the coefficients using LMMSE estimator eq.5.6

$$g_i = \left(\frac{\sigma_g^2}{\sigma_g^2 + \sigma_v^2}\right) \times y_i \tag{5.6}$$

where g_i is the denoised image coefficient or clean coefficient after the additive noise

removal.

For despeckling, the image is divided into non overlapping patches of size $N \times N$. The patches are converted into 1D training vectors, which are arranged as columns so as to form a matrix of training vectors, S. The size of matrix S is $N^2 \times M$, where M is the number of patches. To denoise the image, the patches or the block of patches, the data adaptive method like the Principal Component Analysis and the SVD method is adopted.

5.2.1.3 Despeckling by Processing of Non Local Patches

In the second phase of denoising, the sonar image, the reflectivity is considered to be corrupted by the Rayleigh distributed speckle noise model as given in eq.5.7,

$$g_s = u_s n_s \tag{5.7}$$

where g_s is the observed noisy value at site s and u_s its underlying noise-free value. The denoising process is expressed as a Weighted Maximum Likelihood Estimation (WMLE) problem with the estimate $\hat{u}_s$ defined by eq.5.8,

$$\hat{u}_s = \arg max_{u_s} \Sigma_t w(s,t) \log p(g_t|u_s) \tag{5.8}$$

where t is a pixel index and $w(s,t)$ is a data-driven weight depending on the similarity between pixels with index s and t. This patch-based filter can be considered non-local as pixel values far apart can be averaged together, depending on the weight values i.e., surrounding patch similarity and the new measure of similarity between pixels will better reflect the image content. For the non-additive noise model, the weight $w(s,t)$ is given in eq.5.9,

$$w(s,t) \cong p(u_s = u_{\Delta_t}|v)^{(1/h)} \tag{5.9}$$

where $u_{\Delta s}$and $u_{\Delta t}$ denote the sub-image extracts from the parameter image u in the respective windows Δ_s and Δ_t, and $h > 0$ is a scalar parameter, that depends on the noisy image parameter, search window size and width. The h parameter is similar to that of the NL means algorithm and acts on the size of the fuzzy set i.e., the number significant weights to control the amount of filtering and it probably

counter balances the invalidity of the patch independence assumption [136]. All the parameter in this session are taken under the similar assumptions as done in the reference [102].

The pixel amplitudes A_s are modeled as independent and identically distributed according to the following a Rayleigh distribution eq.5.10,

$$p(A_s|\hat{R}_s) = \frac{2L^L}{\Gamma(L)\hat{R}_s^L} A_s^{2L-1} exp(-\frac{LA_s^2}{\hat{R}_s}) \tag{5.10}$$

where $\hat{R}$ is the underlying reflectivity image and L the equivalent number of looks, calculated as the ratio of mean to standard deviation of the image and the underlying noise-free amplitude image $\hat{A}$ is the square root of the reflectivity image $\hat{R}$. From the first order optimality condition, the following estimation eq.5.11,

$$\hat{R}_S = \frac{\Sigma_t w(s,t) A_t^2}{\Sigma_t w(s,t)} \tag{5.11}$$

must hold to maximize the WMLE and according to weights derivation for multiplicative noise eq.5.12,

$$p(A_{s,k}, A_{t,k}|\hat{R}_{s,k} - \hat{R}_{t,k})\alpha \left(\frac{A_{s,k}, A_{t,}}{A_{s,k}^2 + A_{t,k}^2} \right)^{2L-1} \tag{5.12}$$

with the final weights as eq.5.13,

$$w(s,t) = \exp\left[-\Sigma_k \left(\frac{2L-1}{h} \log\left(\frac{A_{s,k}}{A_{t,k}} + \frac{A_{t,k}}{A_{s,k}} \right) \right) \right] \tag{5.13}$$

which can be used for processing.

5.2.1.4 Performance Evaluation

A methodology for patch based denoising and its application to additive Gaussian and multiplicative speckle noises was proposed. A patch based blind denoising procedure is followed for estimating the noise level in the sonar images which results in an improved denoising performance. Additive noise removal helps to smoothen the image while speckle removal helps to get a better image with details preserved. The method enforces smoothness while preserving edges. Fig.5.1 shows that the

proposed method denoises without distorting useful image information as well as the important image edges. The additive denoising is approached using sparse ap-

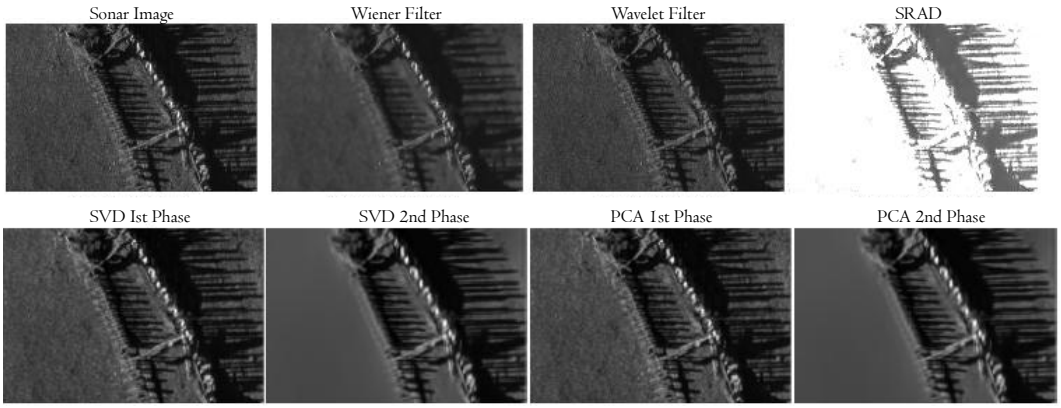

Fig. 5.1: Visual comparison of despeckling techniques for sonar image. In Phase 1 the additive Gaussian noise removed and in Phase 2 speckle noise also removed

proximation of local image patches which is a characteristic of sonar images. For the multiplicative noise removal non-homomorphic approach was followed, so that the unnecessary introduction of the bias in the image was avoided.

After a number of simulations, for the additive noise level estimation a patch of size 8×8 was used. Local patch based processing uses a patch size of 8×8 the and 8 adjacent patches are combined to form a block in block based processing. For the non local patch processing also a patch of 8×8 is used.

The filters are assessed in sonar images by means of visual inspection and quantitative measures. As the major noise content is the speckle, the assessment parameters ENL, SSI, CC, SMPI and COV were used. The improvement in the ENL is a clear indication of the speckle reduction in the second stage. The Table5.1 and Fig.5.2 depicts the numerical comparison.

The metric value comparisons for the varying window width is depicted in the Table 5.2 and the graphical comparison in Fig.5.3. The higher despeckling capability at the lower window width is at the cost of increased computational complexity.

Table 5.1: Metric values for different methods for a sonar image of ENL 5.8422

Metric	Wiener	SRAD	Wavelet	SVD of Patches	PCA of Patches	SVD of Block	PCA of block
ENL	6.9486	6.1805	5.5116	7.3797	7.3781	7.3800	7.3845
SSI	0.9171	0.9724	1.0297	0.8899	0.8900	0.8899	0.8896
CC	0.9646	0.9898	0.9933	0.9467	0.9467	0.9466	0.9465
COV	0.3794	0.4022	0.4260	0.3681	0.3682	0.3681	0.3680
SMPI	0.2023	0.9552	3.0623	0.1093	0.1102	0.1143	0.1139

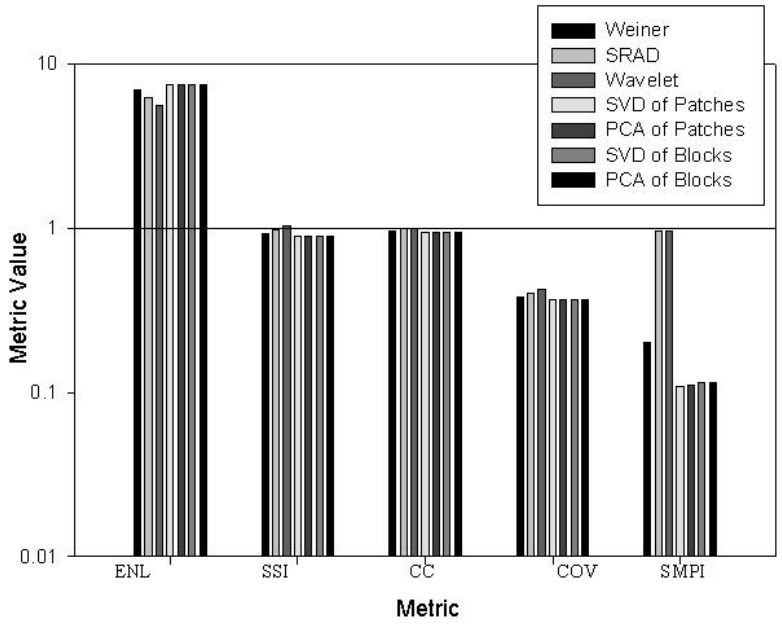

Fig. 5.2: Performance of the mixed noise removal method

5.3 Spatial Domain

In the spatial domain, a high frequency noise removal method employing the fractional integral mask was applied on different sonar images affected with high frequency speckle noise. The fractional masks when compared with the integer order masks can model the sonar image in a better way and has a good filtering effect. The results of the experiments prove that, noise removal using fractional integral mask is better than traditional despeckling method. According to the observations, mask extraction is possible for lower fractional orders and this helps in reducing the

Table 5.2: Metric values for a sonar image of ENL 5.8422 for varying window width

Window	2	3	4	5	6	7	8
ENL	9.1561	9.1584	8.7726	8.257	7.9164	7.7095	7.5502
SSI	0.79893	0.79883	0.8162	0.8413	0.85921	0.87066	0.8798
CC	0.8989	0.89473	0.90658	0.92205	0.93147	0.93715	0.94143
COV	0.33048	0.33044	0.33763	0.34801	0.35542	0.36015	0.36393
SMPI	0.033575	0.00942	0.016907	0.046955	0.012042	0.025944	0.039381

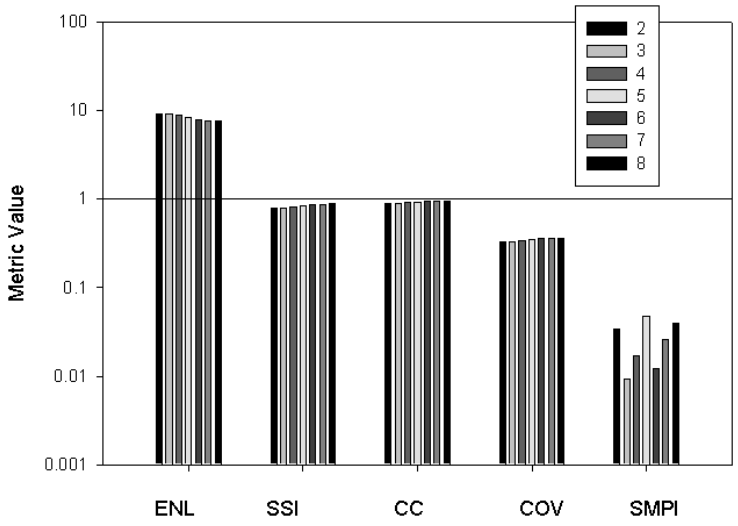

Fig. 5.3: The metric values for varying window width

complexity of computation without affecting the despeckling performance adversely. Again the despeckling filters applied only on to the speckle affected class of sonar image patches makes the algorithm computationally more efficient.

In the subsequent method an unscented Kalman filter estimation for side scan sonar image was carried. The non linear state estimation method provides an efficient recursive means to estimate the state of a process, in a way that minimizes the mean of the squared error. 1D UKF is applied on to the multiplicative noise model of the side scan sonar image considering each row as a one dimensional signal.

5.3.1 High Frequency Filtering Method

The classical denoising algorithms uses the integer order integration directly or indirectly and this results in loss of image details. Fractional calculus has proven to be better over integer calculus to analyze and model natural signals [137]. Riemann-Liouville (RL), Grunwald- Letnikov(GL) and Caputo are widely used definitions of fractional calculus. Fractional integral algorithm based on RL definition and GL definition are used for image denoising [138] and the [139] uses Riesz fractional differential operator for image enhancement.

Riemann-Liouville definition of fractional calculus was used to create the Fractional integral masks (FIM) in eight directions. The use of a mask incorporated with the significant coefficients from the eight directional masks and a single convolution operation required in such case helped in obtaining the computational efficiency. The design of the despeckling filter uses the naive homogeneity index for patch classification. The application of the mask convolution only to the selected patches again reduced the computational complexity. The non-homomorphic approach used in the proposed method avoids the undesired bias occurring in the traditional homomorphic approach. Experiments showed that the mask size required directly dependent on the fractional order and so can be reduced for lower fractional orders thus ensuring the computation complexity reduction for lower orders.

5.3.1.1 Fractional Integral Mask

The noise which exists as high frequency signals in image can be eliminated by low pass filtering [140]. The coefficients of mask are calculated using Reimann-Lioville definition for Fractional integral calculus [141]. Fractional order $\nu > 0$ corresponds to fractional differentiation whereas fractional orders $\nu < 0$ corresponds to fractional integration. The Reimann-Liouville definition for fractional calculus is as eq.5.14:

$$\begin{aligned} \frac{d^{\nu}}{dx^{\nu}} s(x) &= \frac{1}{\Gamma(-\nu)} \int_0^x \frac{s(\xi)}{(x-\xi)^{\nu+1}} d\xi \\ &= \frac{1}{\Gamma(-\nu)} \int_0^x \frac{s(x-\xi)}{\xi^{\nu+1}} d\xi, \nu < 0 \end{aligned} \tag{5.14}$$

When dividing the signal $s(x)$ to N equal parts and on changing the continuous integral to discrete sum of products, the equation can be rewritten eq.5.15,

$$\frac{d^{\nu}}{dx^{\nu}}s(x) \cong \frac{x^{-\nu}N^{\nu}}{\Gamma(-\nu)}\Sigma_{k=0}^{N-1}\frac{s_k + s_{k+1} + 1}{-2\nu} \times [(k+1)^{-\nu} - k^{-\nu}], \nu < 0 \tag{5.15}$$

The image is a two dimensional signal in which each pixel is represented using its x and y coordinates. So partial differentiation is essential. The fractional differentiation equation can be modified as eq.5.16 and eq.5.17,

$$\begin{aligned}\frac{\delta^{\nu}s(x,y)}{\delta x^{\nu}} \cong & \frac{1}{\Gamma(-\nu)(-2\nu)}s(x,y) \\ + & \tfrac{1}{\Gamma(-\nu)(-2\nu)} \times \Sigma_{k=1}^{n-1}((k+1)^{-\nu} - (k-1)^{-\nu})s(x-k,y) \\ + & \frac{1}{\Gamma(-\nu)(-2\nu)}(n^{-\nu} - (n-1)^{-\nu})s(x-n,y)\end{aligned} \tag{5.16}$$

$$\begin{aligned}\frac{\delta^{\nu}s(x,y)}{\delta y^{\nu}} \cong & \frac{1}{\Gamma(-\nu)(-2\nu)}s(x,y) \\ + & \tfrac{1}{\Gamma(-\nu)(-2\nu)} \times \Sigma_{k=1}^{n-1}((k+1)^{-\nu} - (k-1)^{-\nu})s(x,y-k) \\ + & \frac{1}{\Gamma(-\nu)(-2\nu)}(n^{-\nu} - (n-1)^{-\nu})s(x,y-n)\end{aligned} \tag{5.17}$$

In the proposed work the above equation is used to estimate the coefficients of masks in eight directions according to the value of order, ν. As Derivative is the left inverse of integration, and therefore, take negative decimal values for ν. For different fractional orders different eight directional masks are obtained and the significant coefficients in the masks has an inverse relation to the fractional order. Mask coefficients are estimated for the required order using eq.5.18.

$$\begin{aligned}C_{S_0} &= \frac{1}{\Gamma(-\nu)(-2\nu)} \\ C_{S_1} &= \frac{2^{-\nu}}{\Gamma(-\nu)(-2\nu)} \\ &. \\ &. \\ C_{S_k} &= \frac{(k+1)^{-\nu} - (k-1)^{-\nu}}{\Gamma(-\nu)(-2\nu)} \\ &. \\ C_{S_n} &= \frac{(n)^{-\nu} - (n-1)^{-\nu}}{\Gamma(-\nu)(-2\nu)}\end{aligned} \tag{5.18}$$

A 7×7 masks in eight directions is used in order to compare the performance with existing filters. The value k in eq.5.18 varies from 0 to n where the value of $n = N - 1$ for a N masks. The method implemented uses the Reimann-Lioville definition to create fractional integral masks in eight directions. For a 7×7 mask take $N = 7$ and then $n = 6$. Then by giving the required fractional order $-\nu$, the seven non-zero coefficients of the mask can be generated. These coefficients can be arranged in the 7×7 matrix with the orientations given as 0 degree, 45 degree, 90 degree, 135 degree, 180 degree, 225 degree, 270 degree and 315 degree to get the eight directional masks with all other coefficients being zeroes. The mask can be created for any orders ranging from -0.0001 to -1.000. In simulations, the performance of the mask is found good for the order range -0.0001 to -0.4. The Fig.5.4 shows the eight directional masks obtained for the order $\nu = 0.0001$.

0	0	0	0	0	0	0
0	0	0	0	0	0	0
0	0	0	0	0	0	0
0.5003	0.5006	0.0005	0.0003	0.0003	0.0002	0.0002
0	0	0	0	0	0	0
0	0	0	0	0	0	0
0	0	0	0	0	0	0

0 degree

0	0	0	0	0	0	0
0	0	0	0	0	0	0
0	0	0	0	0	0	0
0.0002	0.0002	0.0003	0.0003	0.0005	0.5006	0.5003
0	0	0	0	0	0	0
0	0	0	0	0	0	0
0	0	0	0	0	0	0

180 degree

0	0	0	0.5003	0	0	0
0	0	0	0.5006	0	0	0
0	0	0	0.0005	0	0	0
0	0	0	0.0003	0	0	0
0	0	0	0.0003	0	0	0
0	0	0	0.0002	0	0	0
0	0	0	0.0002	0	0	0

270 degree

0	0	0	0.0002	0	0	0
0	0	0	0.0002	0	0	0
0	0	0	0.0003	0	0	0
0	0	0	0.0003	0	0	0
0	0	0	0.0005	0	0	0
0	0	0	0.5006	0	0	0
0	0	0	0.5003	0	0	0

90 degree

0.5003	0	0	0	0	0	0
0	0.5006	0	0	0	0	0
0	0	0.0005	0	0	0	0
0	0	0	0.0003	0	0	0
0	0	0	0	0.0003	0	0
0	0	0	0	0	0.0002	0
0	0	0	0	0	0	0.0002

315 Degree

0	0	0	0	0	0	0.5003
0	0	0	0	0	0.5006	0
0	0	0	0	0.0005	0	0
0	0	0	0.0003	0	0	0
0	0	0.0003	0	0	0	0
0	0.0002	0	0	0	0	0
0.0002	0	0	0	0	0	0

225 degree

0	0	0	0	0	0	0.0002
0	0	0	0	0	0.0002	0
0	0	0	0	0.0003	0	0
0	0	0	0.0003	0	0	0
0	0	0.0005	0	0	0	0
0	0.5006	0	0	0	0	0
0.5003	0	0	0	0	0	0

45 degree

0.0002	0	0	0	0	0	0
0	0.0002	0	0	0	0	0
0	0	0.0003	0	0	0	0
0	0	0	0.0003	0	0	0
0	0	0	0	0.0005	0	0
0	0	0	0	0	0.5006	0
0	0	0	0	0	0	0.5003

135 degree

Fig. 5.4: Fractional integral masks in 8 directions

5.3.1.2 Computation Complexity Reduction Methods

Two algorithms has been proposed for denoising using the eight directional masks derived from the above equations. The block diagrams of the algorithms are depicted in figures Fig.5.5 and Fig.5.6.

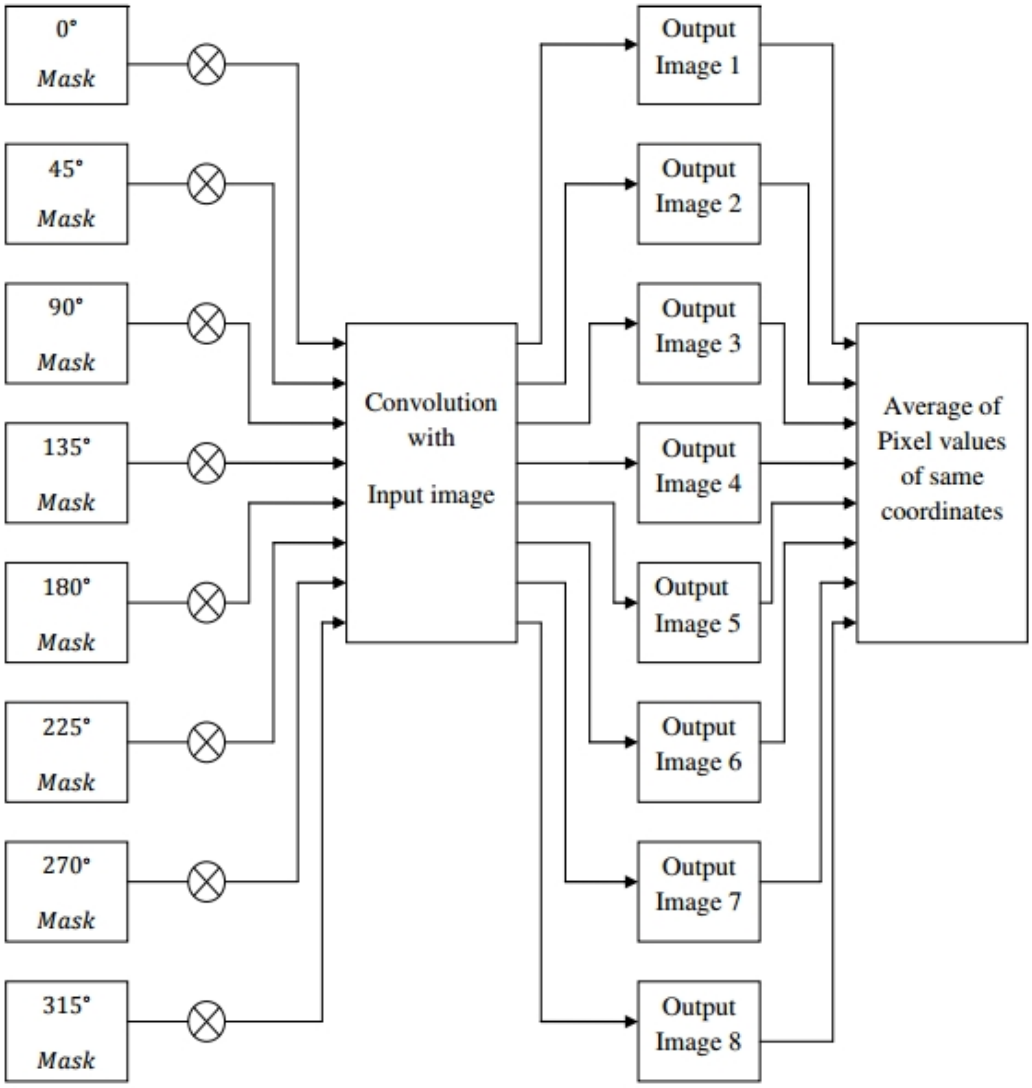

Fig. 5.5: Block diagram of the first algorithm

In the first algorithm, the image is convoluted separately with eight directional

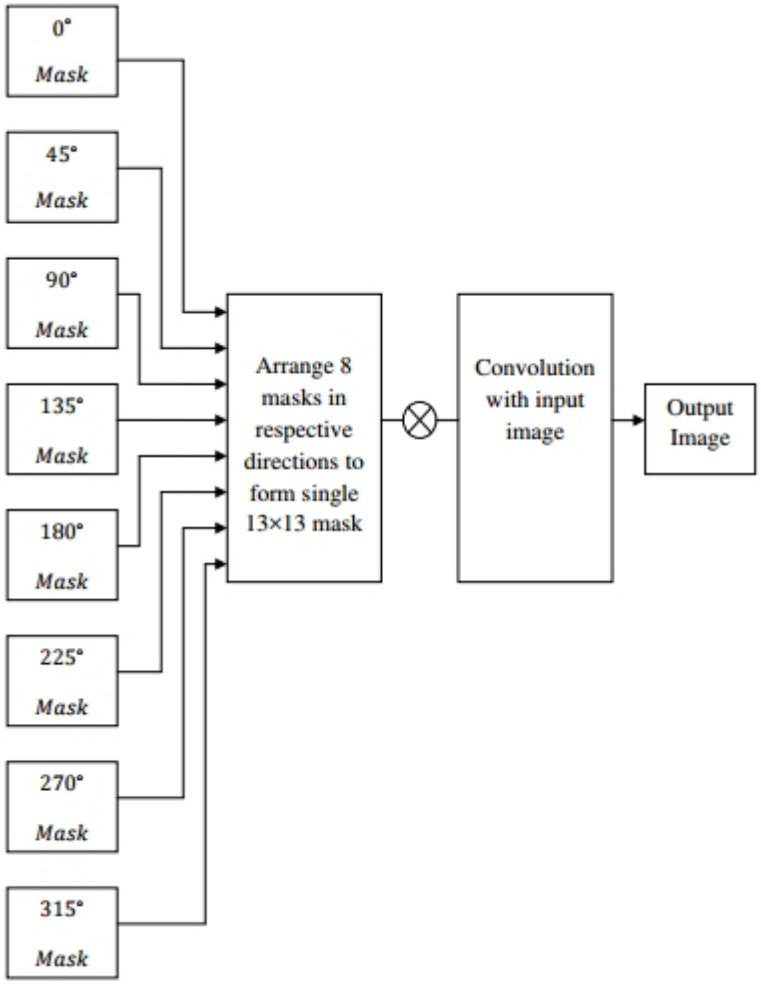

Fig. 5.6: Block diagram of the second algorithm

fractional integral masks. These masks can be implemented for different orders. The convolution of the image with masks of eight directions assures better denoising as it considers the relationship of the pixel of interest with all its neighbouring pixels of every direction. The individual results of convolution are then combined by taking the average of pixel values corresponding to the respective (x, y) coordinate positions. Thus, the resultant image will carry the effect of adjacent pixels of eight directions. This method ensures better denoising performance than the traditional noise removal algorithms. Another advantage of the algorithm is that this technique can be very

well utilized in applications which involve directional noise. Denoising of the image can be done in the direction of interest. The performance of mask of each direction over the image can be assessed separately if required and works well for the range of fractional order 0.0001 to 0.4.

In the second algorithm, the eight fractional masks are arranged and combined according to their directional characteristics. In the mask combining process, after arranging the masks of size 7×7 with the correct orientation, the center value of the mask will have the component from all the eight masks and the remaining positions with the single values. The individual values of the 13×13 mask formed are divided by N. The extreme values of the combined mask will then have values of the order 10^{-5}, so approximated to fourth decimal digit to the show existence of the non zero values in the respective positions. For individual directional masks of size 7×7 formed for the order $\nu = 0.0001$ of Fig.5.4, this process resulted in the formation of a single mask of size 13×13 as shown in Fig.5.7. The noisy sonar image is convolved with the resultant mask. The usage of single mask reduces the computation complexity. This method also reduces the computation time by eliminating the need for multiple convolution operation. The algorithm gave good denosing results for the fractional orders of range 0.0001 to 0.18. The denoising performance of second algorithm is high when compared with that of the first and much higher than traditional noise removal techniques.

0.0001	0	0	0	0	0	0.0001	0	0	0	0	0	0.0001
0	0.0001	0	0	0	0	0.0001	0	0	0	0	0.0001	0
0	0	0.0001	0	0	0	0.0001	0	0	0	0.0001	0	0
0	0	0	0.0001	0	0	0.0001	0	0	0.0001	0	0	0
0	0	0	0	0.0002	0	0.0002	0	0.0002	0	0	0	0
0	0	0	0	0	0.0717	0.0717	0.0717	0	0	0	0	0
0.0001	0.0001	0.0001	0.0001	0.0002	0.0717	0.5724	0.0717	0.0002	0.0001	0.0001	0.0001	0.0001
0	0	0	0	0	0.0717	0.0717	0.0717	0	0	0	0	0
0	0	0	0	0.0002	0	0.0002	0	0.0002	0	0	0	0
0	0	0	0.0001	0	0	0.0001	0	0	0.0001	0	0	0
0	0	0.0001	0	0	0	0.0001	0	0	0	0.0001	0	0
0	0.0001	0	0	0	0	0.0001	0	0	0	0	0.0001	0
0.0001	0	0	0	0	0	0.0001	0	0	0	0	0	0.0001

Fig. 5.7: 13×13 mask formed by combining the directional masks

Experiment shows that, for small orders, significant mask coefficients are found only at the central part of the combined mask. This characteristic is observed with fractional orders in the range 0.0001 to 0.0020. Fig.5.8 shows the 13×13 mask for order 0.0008. Hence, for these orders the mask size for the second algorithm was reduced by extracting the central portion where significant coefficients are actually

available as 5×5 mask. By reducing the mask size, computation complexity was again reduced.

0.00001	0	0	0	0	0	0.00001	0	0	0	0	0	0.00001
0	0.00001	0	0	0	0	0.00001	0	0	0	0	0.00001	0
0	0	0.00001	0	0	0	0.00001	0	0	0	0.00001	0	0
0	0	0	0.00001	0	0	0.00001	0	0	0.00001	0	0	0
0	0	0	0	0.0001	0	0.0001	0	0.0001	0	0	0	0
0	0	0	0	0	0.0715	0.0715	0.0715	0	0	0	0	0
0.00001	0.00001	0.00001	0.00001	0.0001	0.0715	0.5717	0.0715	0.0001	0.00001	0.00001	0.00001	0.00001
0	0	0	0	0	0.0715	0.0715	0.0715	0	0	0	0	0
0	0	0	0	0.0001	0	0.0001	0	0.0001	0	0	0	0
0	0	0	0.00001	0	0	0.00001	0	0	0.00001	0	0	0
0	0	0.00001	0	0	0	0.00001	0	0	0	0.00001	0	0
0	0.00001	0	0	0	0	0.00001	0	0	0	0	0.00001	0
0.00001	0	0	0	0	0	0.00001	0	0	0	0	0	0.00001

(a)

0.0001	0	0.0001	0	0.0001
0	0.0715	0.0715	0.0715	0
0.0001	0.0715	0.5717	0.0715	0.0001
0	0.0715	0.0715	0.0715	0
0.0001	0	0.0001	0	0.0001

(b)

Fig. 5.8: Fractional integral mask for order 0.0008 (a) Original 13×13 Mask (b) Extracted 5×5 Mask

5.3.1.3 Denoising Results using Fractional Integral Mask

The Fig.5.9 shows the visual results of the fractional integral mask of size 13×13 convolved with the sonar image of ENL 6.8510, for different fractional the order of the mask. The Table 5.3 gives the parametric values for varying fractional orders and the graphical comparison is shown in Fig.5.10. Denoising performance is measured based on visual perception and other *without-reference* measurement methods. Fractional order can be selected based on the visual results and the quantitative assessment, also considering the processing time.

Table 5.3: Metric values for different fractional order

Order	0.001	0.003	0.005	0.007	0.01	0.03	0.05	0.07	0.1
ENL	8.6614	8.6821	8.703	8.7195	8.7517	8.946	9.1347	9.3206	9.5941
SSI	0.8894	0.8883	0.8872	0.8864	0.8848	0.8751	0.866	0.8573	0.845
CC	0.9662	0.9661	0.9658	0.9655	0.9652	0.9627	0.9599	0.957	0.9523
COV	0.3398	0.3394	0.339	0.3387	0.338	0.3343	0.3309	0.3275	0.3228
SMPI	11.771	12.2767	12.7913	13.3061	14.0937	19.6381	25.746	32.4686	43.7816

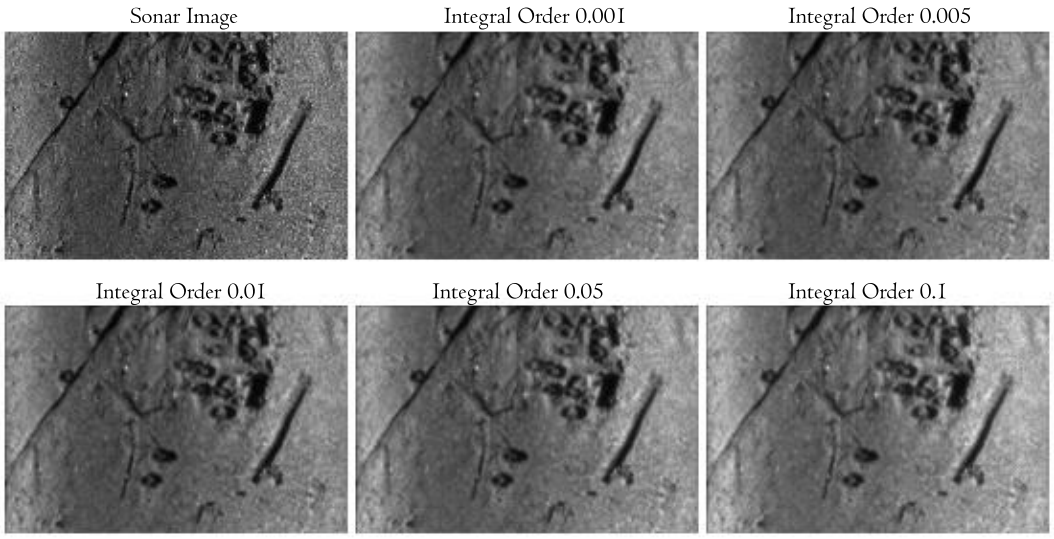

Fig. 5.9: Visual comparison for varying fractional order

Experiments shows that the mask size required depends on the fractional order. Mask size can be reduced for lower fractional orders thus ensuring the computation complexity reduction for lower orders. For lower orders the mask size after mask combining is reduced by extracting the central portion where significant coefficients are actually available. By further reducing the mask size, instead of going with the 13×13 mask, computation complexity is again reduced. The reduction in the mask size of the combined mask to 11×11, 9×9, 7×7, or 5×5 can be based on the significant coefficients which depends on the fractional order.

Performance of the algorithm is compared with that of traditional noise removal method for the given sonar image by taking an order 0.01, which gives a better visual results compared to the other orders as shown in Fig.5.9. The Fig.5.11 shows the result of the comparison of the proposed method with the existing denoising and the Table 5.4 and Fig.5.12 gives the parametric value comparison of the fractional order filtering with the different existing despeckling methods.

5.3.1.4 Patch Despeckling using Fractional Integral Mask

Patch classification based on the proposed naive homogeneity index was adopted and only the intermediate patches which are assumed to be speckle affected are despeckled using the fractional integral mask convolution method before further processing. The patch size is selected as 10 and the convolution with the 13×13 mask

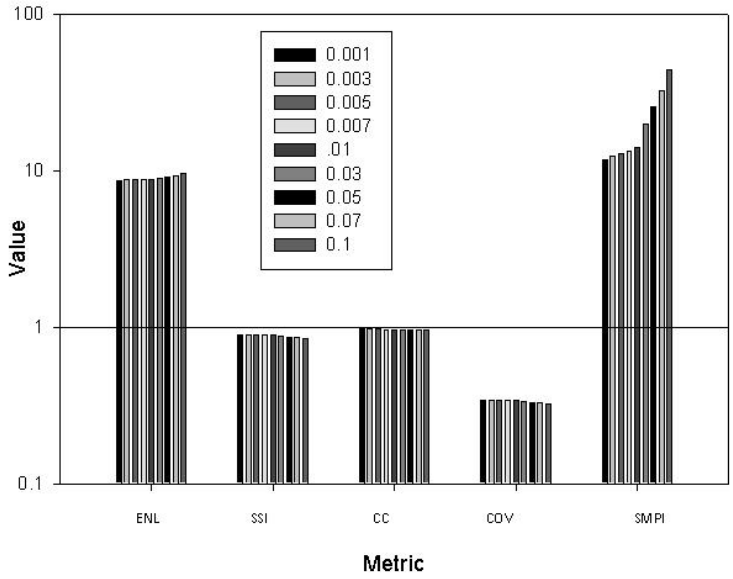

Fig. 5.10: Despeckling performance of varying filter order

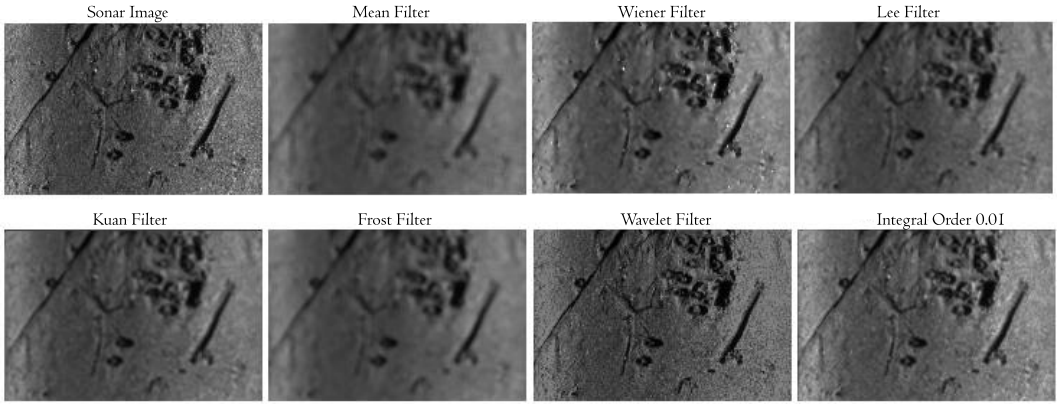

Fig. 5.11: Visual comparison of the fractional mask method with the existing

is employed on the relevant patches. The computational efficiency of the method lies in the fact that, here also the combined fractional integral mask of size 13×13 is used, but the convolution of the mask with only the selected patch is sufficient. Table 5.5 depicts that as the fractional order increases there is a depreciation seen in the despeckling performance. This shows that the despeckling can be effective with further low fractional orders. When the fractional orders are reduced instead of

Table 5.4: Metric values for despeckling techniques and FIM of order 0.01

Filter	Mean	Wiener	Lee	Frost	Kuan	Wavelet	FIM order 0.01
ENL	11.018	7.6657	9.5421	10.545	9.4286	6.9838	8.7517
SSI	0.7885	0.9454	0.8473	0.806	0.8524	0.9904	0.8848
CC	0.8415	0.9356	0.8951	0.8636	0.8745	0.9906	0.9652
COV	0.3013	0.3612	0.3237	0.3079	0.3257	0.3784	0.338
SMPI	0.0099	0.3489	0.0022	0.1163	0.4067	3.7105	14.0937

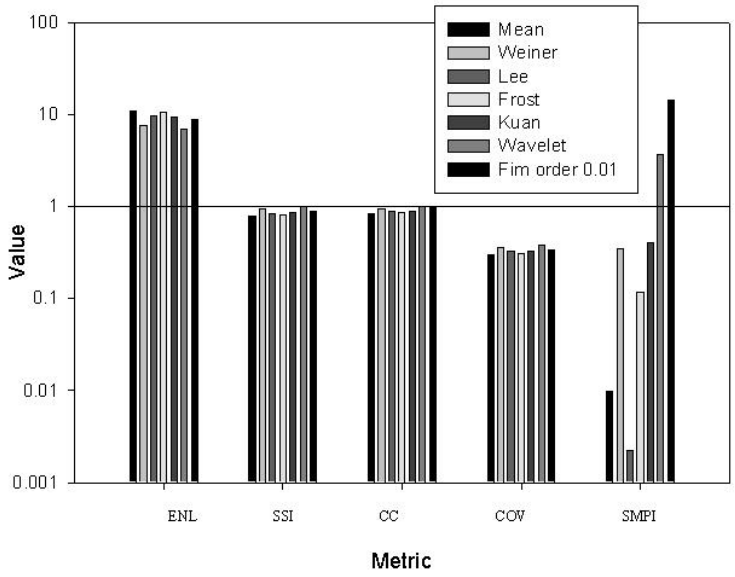

Fig. 5.12: Performance of fractional order 0.01 filter with other existing methods

going with a 13×13 mask, a lower size combined mask, for example a 5×5 may be sufficient to give almost the similar performance. This is due to the fact that lower fractional order directional mask in eight directions have less significant coefficients themselves and so the combined mask. The denoising capability is slightly traded off for the computation reduction. Visual comparisons were shown in Fig.5.13 and metric value comparison in Table5.5.

The Fig.5.14 gives the parametric values for the heterogeneous patch despeckling for varying fractional order of the mask for a patch of size 10. The ENL enhancement for the lower fractional order encourages to use the lower fractional orders for despeckling and inturn helps in reducing the mask size from 13×13 to lower ones

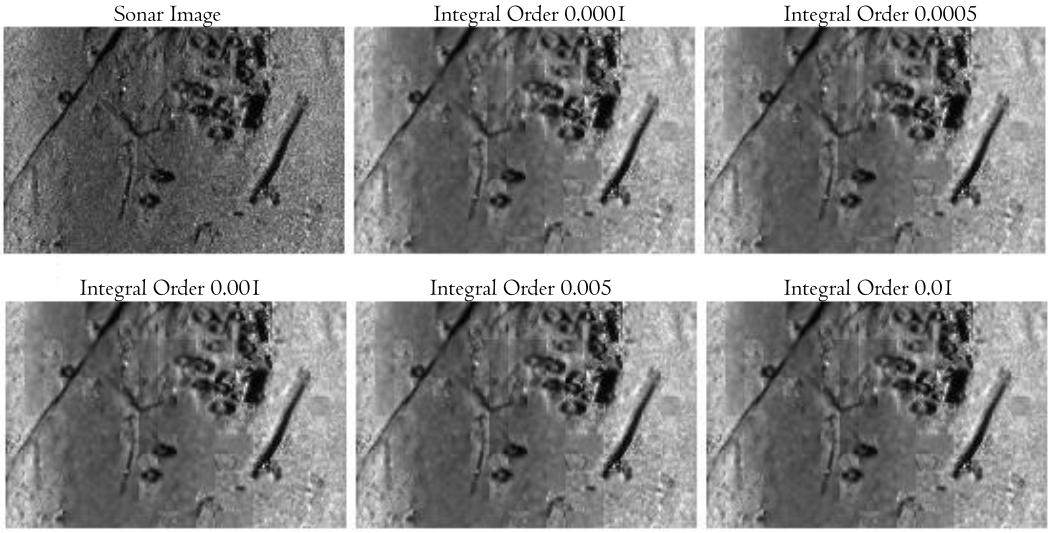

Fig. 5.13: Visual comparison for the heterogeneous patch despeckling for varying fractional order of the mask

Table 5.5: Metric value for the heterogeneous patch despeckling for varying fractional order of the mask for a patch of size 10

Order	0.0001	0.0005	0.001	0.005	0.007	0.01	0.05
ENL	6.8936	6.8872	6.8792	6.8147	6.7824	6.7338	6.0876
SSI	0.9969	0.9974	0.9979	1.0027	1.005	1.0087	1.0609
CC	0.9486	0.9484	0.9481	0.9459	0.9448	0.943	0.9165
COV	0.3809	0.381	0.3813	0.3831	0.384	0.3854	0.4053
SMPI	0.4639	0.4645	0.4651	0.4697	0.4706	0.4719	0.4903

as the significant coefficients in the periphery of the masks becomes less significant.

The patch based denoising helps the sonar image interpreters in defining their areas of interest to be despeckled without doing the convolution operation for the entire image pixels.

5.3.2 Nonlinear Estimation Method

In the nonlinear state estimation method, the unscented Kalman filter based approach is used for side scan sonar image estimation from the observation model of the image. First the noise level in the side scan sonar image is estimated using a patch based algorithm and then non-blind denoising is done. For the blind denoising part, the heterogeneity of side scan sonar image patches is exploited.

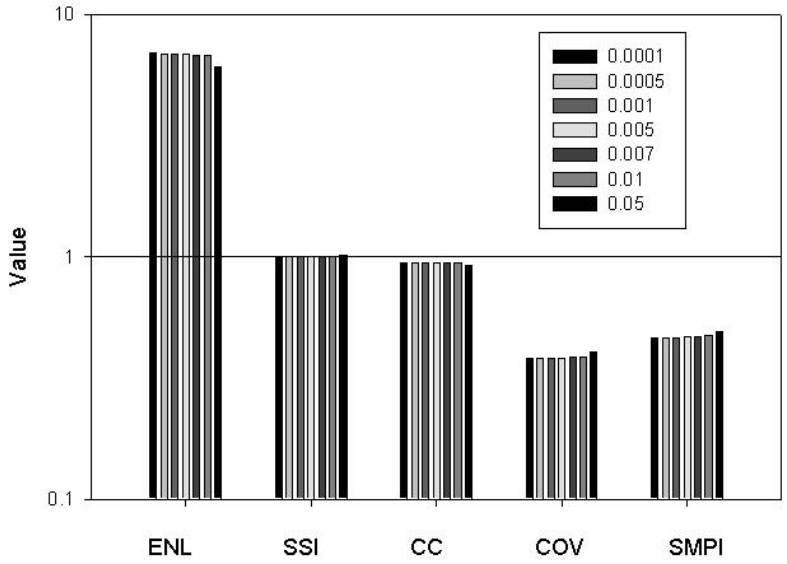

Fig. 5.14: Performance for varying order of the fractional order filter

The application of one dimensional Kalman filter to the two dimensions [142] to smooth out the observation noise in image data does not preserve the optimality of the linear state estimation filter. For nonlinear systems, subject to Gaussian noise, the EKF [143] is frequently applied for estimating the system state vector from output measurements. The unscented Kalman filter [144] (UKF) is a method for nonlinear state estimation, which does not introduce linearization errors. The unscented transformation helps to propagate mean and covariance through linear transformation. Most of the Kalman estimation methods for image denoising uses the 2D block adaptive filtering. In the proposed method, the unscented Kalman filtering in one-dimension extended to the two-dimensional sonar image restoration is done. The methodology is to deal with signal in the observed domain itself. Even though the absence of the bias due to the nonlinear mapping of the logarithm is an advantage, the estimation of the parameters of the signal and noise pdfs becomes more complex.

5.3.2.1 Noise Level Estimation for Blind Denoising

Blind denoising in images consists of two process, the estimation of the noise level in the image and then the non-blind denoising. Sonar image heterogeneity helps in a patch based noise level estimation. With the available sonar image, the noise level estimation algorithm estimates the unknown standard deviation σ of the image. Because of the redundancy of natural images, the data of natural images span only low-dimensional subspace. If the data of patches $g_i \in R^{N\times N}$ span a subspace whose dimension is smaller than $N \times N$, then called as low-rank patches. The noise level is estimated from the selected patches using Principal Component Analysis. The Principal Component Analysis estimation includes a patch-based noise level estimation algorithm that includes a texture strength metric which is based on the local image gradient matrix and its statistical properties to select low-rank patches without high frequency components from a single noisy image.

In patch-based approaches images are decomposed into a number of patches from an input noisy image in a raster scan form. The patch with the smallest standard deviation among decomposed patches has the least change of intensity. The data model of the patches is shown in eq.5.19,

$$g_i = f_i u_i \quad i = 1, 2, 3, M \tag{5.19}$$

where M is the number of patches, f_i is the i^{th} noise-free image patch with size $N \times N$ written in a vectorized format, and each patch is defined by its center pixel. g_i is the observed vectorized patch corrupted by noise vector u_i with zero-mean and variance σ^2. The minimum variance direction is the eigenvector associated to the minimum eigenvalue of the covariance matrix defined by eq.5.20,

$$\Sigma_g = \frac{1}{M}\Sigma_{i=1}^{M} g_i g_i^T \tag{5.20}$$

where Σ_g is the covariance matrix of the noisy patch g, and $\lambda_{min}(\Sigma)$ represents the minimum eigenvalue of the matrix Σ. The minimum eigenvalue of the covariance matrix $\lambda_{min}(\Sigma_g)$ can be assumed as noise variance, given in eq.5.21,

$$\sigma^2 = \lambda_{min}(\Sigma_g) \tag{5.21}$$

With the variance found out in the above said method, the non blind denoising is

performed.

5.3.2.2 Image Estimation based on UKF Algorithm

Due to the line scanning basis of the side scan sonar, the lines of the image are unrelated in terms of speckle noise and can be treated separately. This property is used in the non linear state estimation method used.

Initialize the state estimate from the first observation. Assuming same number of observable variables as state variables, the image row data of side scan sonar image is modeled by a discrete-time nonlinear dynamic system as eq.5.22 and eq.5.23,

$$x_{k+1} = F(x_k, v_k) \tag{5.22}$$

$$y_k = H(x_k, n_k) \tag{5.23}$$

where x_k is the true pixel intensity and y_k is the measured pixel intensity. The process noise v_k drives the dynamic system, and the observation noise is given by n_k.

Note that additivity of the noise sources is not assumed. The random variables v_k and n_k represent the process as well as measurement noise respectively and are assumed to be white, independent of each other and with normal probability distributions. The noise means are denoted by $\bar{v} = E[v]$ and $\bar{n} = E[n]$, and are usually assumed to equal to zero. The system dynamic model F and H are assumed known. The process noise covariance Q and measurement noise covariance R matrices might change with each time step or measurement, and are obtained by estimating the noise level in the image. The state transition matrix F in the difference equation relates the pixel value at $k+1$ to the pixel value at k, in the absence of either a driving function or process noise. The observation matrix H in the measurement equation relates the state to the measurement y_k and is taken by defining the observed pixel value as the next state pixel value.

The unscented transformation is a method for calculating the statistics of a random variable which undergoes a nonlinear transformation. Consider propagating a random variable x (dimension L) through a nonlinear function, $y = g(x)$. Assume x has mean $\bar{x}$ and covariance P_x. To calculate the statistics of y , form a matrix X of $2L+1$ sigma vectors X_i with corresponding weights W_i , according to the following

eq.5.24,

$$X_0 = \bar{x} \tag{5.24}$$

Then calculate the sigma points using eq.5.25 − eq.5.29,

$$X_i = \bar{x} + \left(\sqrt{(L+\lambda)P_x}\right)_i \qquad i = 1,,L \tag{5.25}$$

$$X_i = \bar{x} - \left(\sqrt{(L+\lambda)P_x}\right)_{i-L} \qquad i = L+1,,2L \tag{5.26}$$

$$W_0^{(m)} = \frac{\lambda}{L+\lambda} \tag{5.27}$$

$$W_0^{(c)} = \frac{\lambda}{L+\lambda} + (1-\alpha^2+\beta) \tag{5.28}$$

$$W_i^{(m)} = W_i^{(c)} = \frac{1}{2L+1} \qquad i = 1,,2L \tag{5.29}$$

where $\lambda = \alpha^2(L+\kappa) - L$ is a scaling parameter. α determines the spread of the sigma points around $\bar{x}$ and is usually set to a small positive value (e.g., $1E^{-3}$). κ is a secondary scaling parameter which is usually set to θ, and β is used to incorporate prior knowledge of the distribution of x . $(\sqrt{(L+\lambda)P_x})_i$ is the i^{th} row of the matrix square root. These sigma vectors are propagated through the nonlinear function in eq.5.30,

$$\Upsilon_i = g(\chi_i) \qquad i = 0,,2L \tag{5.30}$$

and the mean and covariance for y are approximated using a weighted sample mean and covariance of the posterior sigma points using eq.5.31 and eq.5.32,

$$\bar{y} \approx \Sigma_{i=0}^{2L} W_i^{(m)} \Upsilon_i \tag{5.31}$$

$$P_y \approx \Sigma_{i=0}^{2L} W_i^{(c)} (\Upsilon_i - \bar{y})\,(\Upsilon_i - \bar{y})^T \tag{5.32}$$

The process noise covariance and the measurement noise covariances were estimated using the noise level estimation method described in the previous session.

The UKF is a straight forward application of the scaled UT to recursive minimum mean square estimation. The Kalman filter estimates the pixel value at some location and then obtains feedback in the form of measurements. The pixel update equations or the predictor equations are responsible for projecting forward the current pixel value and the error covariance estimates to obtain the *a priori* estimates for the next

pixel value in the row. The measurement update equations or corrector equations are responsible for incorporating a new measurement into the *a priori* estimate to obtain an improved *a posteriori* estimate.

The estimation applied to the some of the rows of the real side scan sonar image for varying total dynamic steps of 100 for different rows are shown in Fig.5.15. From the figure it is evident that from the observed pixel value the filter tries to estimate the next pixel value and the actual state and estimate are saved.

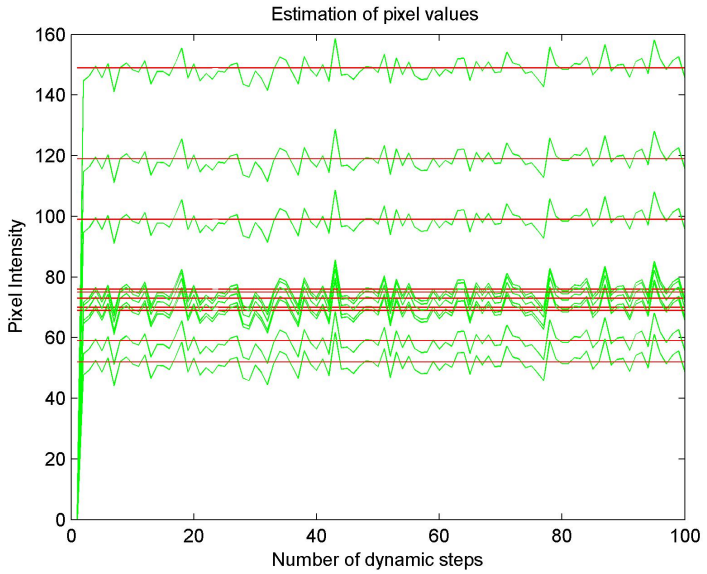

Fig. 5.15: Estimation of pixel values for total dynamic steps, $N = 100$ for some selected rows

The quantitative assessment for a side scan sonar image of ENL 6.851 and COV 0.3821 of the proposed filter for varying total dynamic steps are shown in Table 5.6 and Fig.5.16. The optimum total dynamic step is going to be image dependent and can be found out by trial and error method. The enhancement of the ENL of the denoising method applied to small homogeneous region with ENL 21.6586 is also depicted for different total dynamic steps.

5.3.2.3 Performance Comparison of Speckle Reduction Filters

The filters are assessed using real input data by means of visual inspection and quantitative measures. The experimental results exhibit that proposed despeckling technique performs better than classical despeckling filters and recent techniques in

Table 5.6: Metric values for different total dynamic steps, N

N	10	20	30	50	75	100	200
ENL	7.3394	7.8528	7.8767	7.7725	7.3504	8.1197	7.6009
SSI	0.9662	0.934	0.9326	0.9389	0.9654	0.9186	0.9494
CC	0.7191	0.7174	0.7188	0.7183	0.7192	0.7187	0.7187
COV	0.3691	0.3569	0.3563	0.3587	0.3688	0.3509	0.3627
SMPI	0.3574	0.3487	0.3514	0.35	0.3505	0.3511	0.3571
ENL(H)	23.637	24.8861	25.531	24.821	23.593	26.8334	24.6546

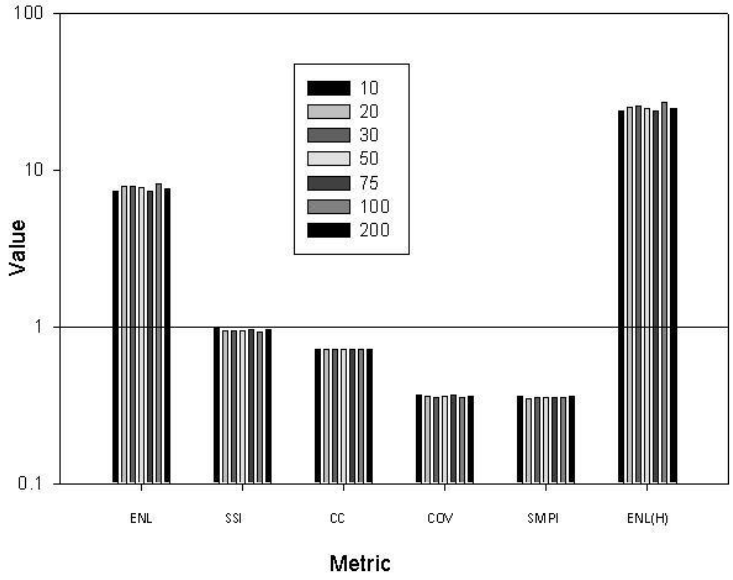

Fig. 5.16: Performance for different dynamic steps, N

terms of visual quality. The proposed technique not only produces smoother images in homogenous areas but also preserve edges. Fig.5.17 shows the visual quality improvement of the method compared to the existing methods.

The quantitative results of Table 5.7 and Fig.5.18 shows the comparison of the proposed method with existing despeckling methods. The visual comparison in terms of edge preserving capability of only the wavelet method was as good as that of the proposed method. So the analysis is done mainly by comparing the quantitative metrices of these two methods. The parameters like ENL, SSI and SMPI are better compared to the wavelet method which has similar performance in visual perfor-

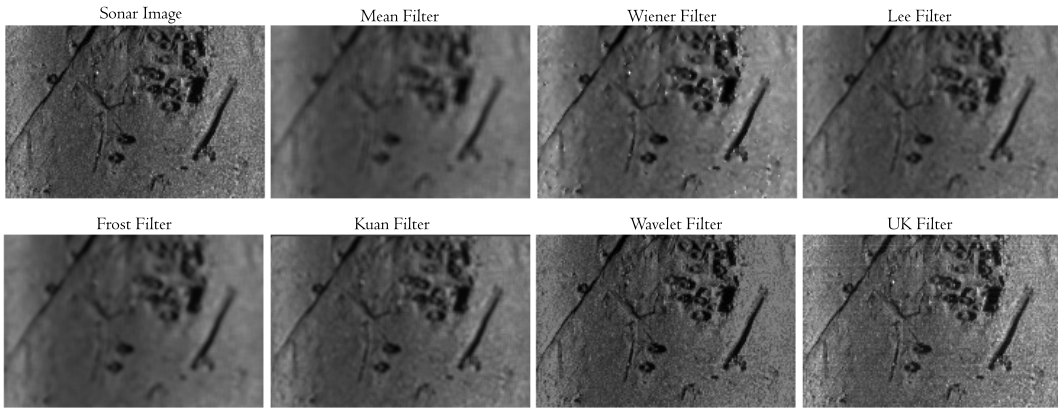

Fig. 5.17: Visual comparison of despeckling techniques with that of non-linear estimation method

mance with the proposed method. The coefficient of variation, a measure of texture preservation on heterogeneous areas, shows a better edge preservation capability for the proposed method.

Table 5.7: Metric values for different despeckling techniques with the proposed

Filter	Mean	Wiener	Lee	Frost	Kuan	Wavelet	Proposed
ENL	11.018	7.6657	9.5421	10.545	9.4286	6.9838	8.1197
SSI	0.7885	0.9454	0.8473	0.806	0.8524	0.9904	0.9186
CC	0.8415	0.9356	0.8951	0.8636	0.8745	0.9906	0.7187
COV	0.3013	0.3612	0.3237	0.3079	0.3257	0.3784	0.3509
SMPI	0.0099	0.3489	0.0022	0.1163	0.4067	3.7105	0.3511

5.4 Results and Discussions

The despeckling of sonar images based on multiplicative speckle-scene models have been implemented and compared with the existing ones. The despeckling results of the different methods proposed need to be analyzed and compared. This analysis is performed by applying these methods to the same image.

5.4.1 Analysis of Different Multiplicative Noise Model Methods

In the non-homomorphic case, methodology is to deal with signal in the observed domain itself and the speckle affected sonar image will have multiplicative speckle-

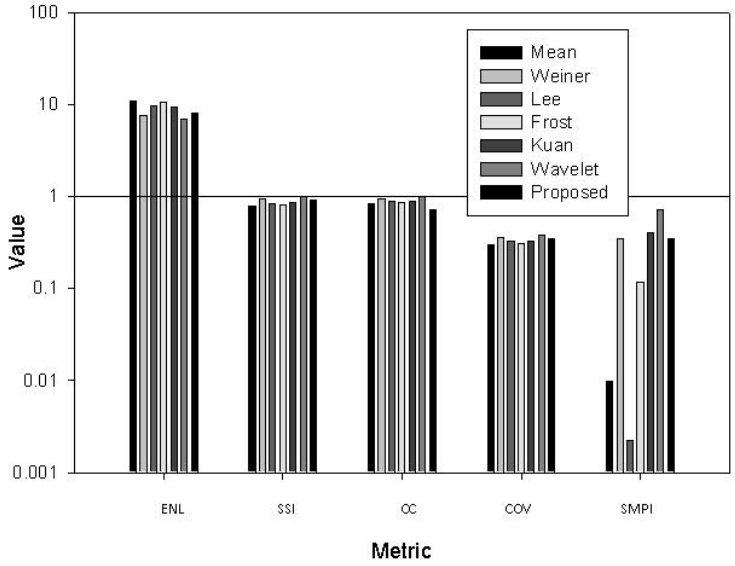

Fig. 5.18: Performance of despeckling techniqued compared with the proposed

scene model representing it. Both the transform domain and spatial domain analysis have been carried out using the blind denoising approach.

In the transform domain assuming a multiple noise affected sonar image, the adaptive processing of local image patches is used to remove the additive Gaussian noise whereas the multiplicative Rayleigh distributed speckle noise is removed by processing of non local patches. The noise variance is estimated using patch based method. The Principal Component Analysis and Singular Value Decomposition methods can be used in the noisy local patches and blocks of patches for additive Gaussian noise denoising. The weighted maximum likelihood denoising of the non local patches is used to reduce the speckle effect.

In the spatial domain denoising, the noise level in the image is estimated using a patch based algorithm and then non blind denoising is done.

The first method in the spatial domain makes use of the fractional order filtering method for denoising. The Fractional Integral Mask incorporated with the significant coefficients from the eight directional masks and a single convolution operation required in such case helps in obtaining the computationally efficient despeckling of sonar images. The application of the mask convolution only to the selected patches

again reduce the computational complexity. Experiments show that the mask size required directly depends on the fractional order and can be reduced for lower fractional orders thus ensuring the computation complexity reduction for lower orders. Order adaptive fractional order mask based denoising can be employed to have improved performance. The procedure is time consuming, but based on the algorithm behaviour it could give better results.

The second method uses an unscented Kalman filter based approach for the side scan sonar image estimation from the observation model of the image. This nonlinear state estimation method is applied on the sonar image by expanding the 1D state estimation method to the 2D state estimation.

In the case of homomorphic transformation method which takes the logarithm of the observed data, the multiplicative speckle noise is transformed into an additive one. This operation may introduce a bias into the denoised image, since an unbiased estimation in the log domain is mapped onto a biased estimation in the observed domain. However the non-homomorphic approach used avoids this undesired bias occurring with the traditional homomorphic approach. Even though the absence of the bias is an advantage, the estimation of the parameters of the signal and noise probabilty density function becomes more complex. The comparison of the various methods using the multiplicative speckle-scene model is done for a real side scan sonar image and has been presented in Fig.5.19. The various non reference metric value comparison is shown in Table 5.8 and the graphical comparison in Fig.5.20, where Mix PCA and Mix SVD is the additive noise removal from the local patches using the PCA and SVD method and the NL PCA and NL SVD is the multiplicative noise removal from the non local (NL) patches using the weighted ML denoising applied to the additive noise removed images.

Table 5.8: Metric value comparison for the despeckling using different multiplicative noise model

Method	MixPCA	NL PCA	Mix SVD	NL SVD	FIM	UKF
ENL	6.3796	7.3784	6.3797	7.3831	7.5669	4.1911
SSI	0.95712	0.88999	0.95711	0.8897	0.87883	1.1809
CC	0.98701	0.94666	0.98701	0.94653	0.96684	0.80492
COV	0.39592	0.36815	0.39591	0.36803	0.36353	0.48847
SMPI	0.0053622	0.11438	0.0054508	0.11404	17.613	0.2606

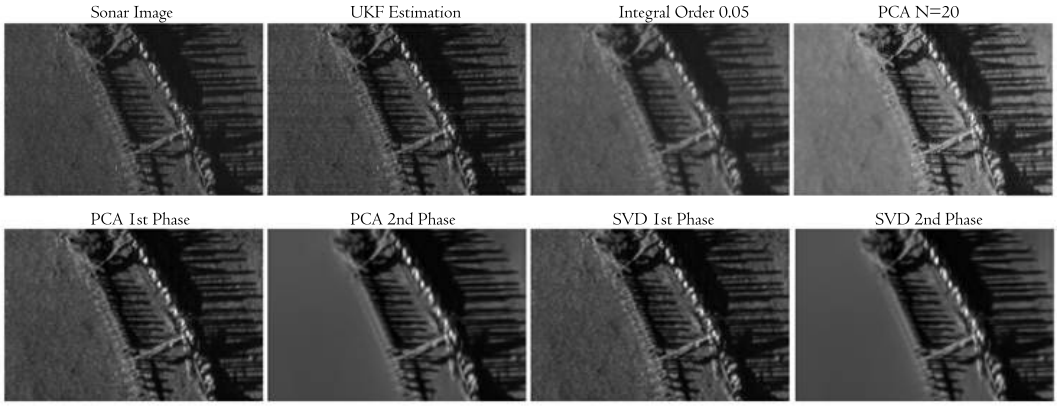

Fig. 5.19: Visual comparison of methods using different multiplicative noise model

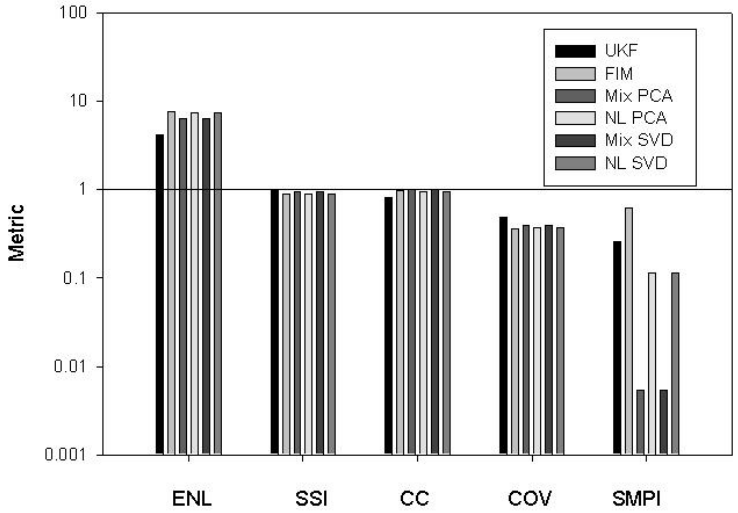

Fig. 5.20: Graphical comparison to grade the performance of despeckling using different multiplicative noise model

5.5 Summary

This chapter deals with different despeckling methods in both transform and spatial domains with the multiplicative noise model followed by the results and discussions of the methodologies adopted in the chapter. The non-homomorphic approach avoids the occurance of undesired bias effects. In the mixed noise removal method, the processing of local and non local patches effectively removes the additive Gaussian and multiplicative noises. While using Fractional Integral Mask denoising method,

the reduction in size of the mask ensures computational reduction without much performance degradation.

Chapter 6

Sonar Image Enhancement

This chapter considers the enhancement of the sonar image which is despeckled by the Fractional Integral Mask algorithm. Image enhancement in sonar images enhance the region of interest in the image by improving the intensity levels of each pixels. This improves the visual appearance of the image and allows the extraction of spatial features. Despeckling of sonar images prior to the enhancement, can generally result in a strong enhancement. Any of the despeckling techniques previously dealt can be a pre-processor for the sonar image enhancement.

6.1 Introduction

The choice of image processing filter for speckle reduction is largely dependent on the application as described in Chanussot *et.al.* [145]. For instance, a detection of the mines based on the analysis of the shadows in sonar image may need an accurate location of the shadows. Therefore a filter with a strong enhancement effect using which the segmentation of the shadow becomes easier is employed. In contrast if a classification of the mines based on the analysis of the echoes is considered, a filter preserving the highly energetic features, with a good resolution is to be preferred. In such instances also enhancement of sonar image is required.

6.2 Processing using Fractional Masks

The algorithm described constitute of a sonar image enhancement section preceded by a noise reduction section, both based on fractional masks. Noise in sonar image

is reduced first by adopting the second method discussed in the fractional order denoising with the fractional integral mask. In the method, the mask size required for lower fractional orders can be reduced and therefore ensures reduction in computation complexity. The enhancement section is based on fractional differential mask which use image adaptive fractional order. The estimation of fractional order is based on adaptive fractional differential function which is used to classify edges and weak texture of the image. A modification in the method for estimation of adaptive order is also proposed. Results show that, the proposed modification reduces the complexity of sonar image enhancement by reducing the required number of masks and thereby reducing the number of convolution operations. The proposed algorithm is applied on raw sonar image and significant enhancement is obtained.

6.3 Generation of Fractional Differential Mask

Fractional integration and differentiation uses fractional or non-integer orders unlike normal calculus. All real objects can be accurately modeled using fractional calculus. Natural signals are generally fractional but classical integer models were used because of the absence of proper solution methods for fractional differential equations [138], [146], [147]. Noise and edges exist as high frequency components in image signal, whereas, the smooth texture exist as low frequency components. Fractional integral mask which act as low pass filter is proved to perform well in removing speckle noise from sonar images. On the other hand, Fractional differential masks (FDM) perform high pass filtering and can be used for the enhancement of these images.

Fractional differential masks are constructed in eight directions and are used to enhance the image. The coefficients of these masks are estimated using the Grunwald-Letnikov equation for fractional derivative. According to Grunwald-Letnikov definition of fractional calculus, the general formula for fractional differentiation is in eq.6.1,

$$\begin{aligned} \frac{d^{\nu}}{dx^{\nu}}s(x) &\equiv \lim_{h\to 0}\frac{1}{h^{\nu}}\sum_{k=0}^{\infty}(-1)^{k}\binom{\nu}{k}s(x-kh) \\ &= \lim_{h\to 0}\frac{1}{h^{\nu}}\sum_{k=0}^{\infty}(-1)^{k}\frac{\Gamma(\nu+1)}{\Gamma(k+1)\Gamma(\nu-k+1)}s(x-kh) \end{aligned} \tag{6.1}$$

For large N the Grunwald-Letnikov equation is as follows eq.6.2,

$$\begin{aligned} \frac{d^{\nu}}{dx^{\nu}}s(x) &\cong \frac{x^{-\nu}N^{\nu}}{\Gamma(-\nu)}\sum_{k=0}^{N-1}\frac{\Gamma(k-\nu)}{\Gamma(k+1)}s(x-\frac{kx}{N}) \\ &= \frac{x^{-\nu}N^{\nu}}{\Gamma(-\nu)}\sum_{k=0}^{N-1}\frac{\Gamma(k-\nu)}{\Gamma(k+1)}s_k \end{aligned} \tag{6.2}$$

For two dimensional signal such as image, partial differentiation will be of the form eq.6.3 and eq.6.4,

$$\begin{aligned} \frac{d^{\nu}s(x,y)}{dx^{\nu}} &\cong s(x,y)+(-\nu)s(x-1,y) \\ &+ \frac{(-\nu)(-\nu+1)}{2}s(x-2,y) \\ &+ \frac{(-\nu)(-\nu+1)(-\nu+2)}{6}s(x-3,y) \\ &+ \ldots\ldots\ldots\ldots\ldots\ldots\ldots \\ &+ \frac{\Gamma(n-\nu-1)}{(n-1)!}s(x-n+1,y) \end{aligned} \tag{6.3}$$

$$\begin{aligned} \frac{d^{\nu}s(x,y)}{dy^{\nu}} &\cong s(x,y)+(-\nu)s(x,y-1) \\ &+ \frac{(-\nu)(-\nu+1)}{2}s(x,y-2) \\ &+ \frac{(-\nu)(-\nu+1)(-\nu+2)}{6}s(x,y-3) \\ &+ \ldots\ldots\ldots\ldots\ldots\ldots\ldots \\ &+ \frac{\Gamma(n-\nu-1)}{(n-1)!}s(x,y-n+1) \end{aligned} \tag{6.4}$$

From the above equations, the coefficients of differential mask can be estimated. The generalized expression for the coefficients of mask is given in eq.6.5. The coefficient values depends on the fractional order. The fractional order can be selected according to the level of enhancement required. For large sonar images, enhancement is necessary only at the region of interest. The fractional differential mask in 8 directions is shown in Fig.6.1.

$$\begin{aligned} C_{S_0} &= 1 \\ C_{S_1} &= -\nu \\ &\cdot \\ &\cdot \\ &\cdot \\ C_{S_k} &= \frac{\Gamma(k-\nu)}{k!\Gamma(-\nu)} \\ &\cdot \\ &\cdot \\ C_{S_n} &= \frac{\Gamma(n-\nu)}{n!\Gamma(-\nu)} \end{aligned} \tag{6.5}$$

6.4 Estimation of Image Adaptive Fractional Order

The visual improvement in sonar image after image enhancement should be such that edges get highlighted without affecting the texture. The best effect of image enhancement is to make edges clear and to preserve weak textures. Higher order increases the amplitude of high frequency signals like strong edges at the expense of low amplitude weak textures. Lower order enhances only the low frequency texture areas. These problems can be avoided by adhering to an an image adaptive fractional differential approach. Bo Li and Wei Xie [148] adopt image adaptive order for enhancement using the dynamic gradient feature of the entire image.

The adaptive fractional order ν for each pixel of the image is estimated using the

0	0	0	0	0	0	0
0	0	0	0	0	0	0
0	0	0	0	0	0	0
1.1284	-0.661	-0.1087	-0.0563	-0.036	-0.0256	-0.0194
0	0	0	0	0	0	0
0	0	0	0	0	0	0
0	0	0	0	0	0	0

0 degree

0	0	0	0	0	0	0
0	0	0	0	0	0	0
0	0	0	0	0	0	0
0	0	0	0	0	0	0
0	0	0	0	0	0	0
0	0	0	0	0	0	0
0	0	0	0	0	0	0

45 degree

0	0	0	0	0	0	0
0	0	0	0	0	0	0
0	0	0	0	0	0	0
-0.0194	-0.0256	-0.036	-0.0563	-0.1087	-0.661	1.1284
0	0	0	0	0	0	0
0	0	0	0	0	0	0
0	0	0	0	0	0	0

180 degree

0	0	0	1.1284	0	0	0
0	0	0	-0.661	0	0	0
0	0	0	-0.1087	0	0	0
0	0	0	-0.0563	0	0	0
0	0	0	-0.036	0	0	0
0	0	0	-0.0256	0	0	0
0	0	0	-0.0194	0	0	0

270 degree

0	0	0	-0.0194	0	0	0
0	0	0	-0.0256	0	0	0
0	0	0	-0.036	0	0	0
0	0	0	-0.0563	0	0	0
0	0	0	-0.1087	0	0	0
0	0	0	-0.661	0	0	0
0	0	0	1.1284	0	0	0

90 degree

1.1284	0	0	0	0	0	0
0	-0.661	0	0	0	0	0
0	0	-0.1087	0	0	0	0
0	0	0	-0.0563	0	0	0
0	0	0	0	-0.036	0	0
0	0	0	0	0	-0.0256	0
0	0	0	0	0	0	-0.0194

315 Degree

0	0	0	0	0	0	1.1284
0	0	0	0	0	-0.661	0
0	0	0	0	-0.1087	0	0
0	0	0	-0.0563	0	0	0
0	0	-0.036	0	0	0	0
0	-0.0256	0	0	0	0	0
-0.0194	0	0	0	0	0	0

225 degree

-0.0194	0	0	0	0	0	0
0	-0.0256	0	0	0	0	0
0	0	-0.036	0	0	0	0
0	0	0	-0.0563	0	0	0
0	0	0	0	-0.1087	0	0
0	0	0	0	0	-0.661	0
0	0	0	0	0	0	1.1284

135 degree

Fig. 6.1: Fractional differential masks in 8 directions

piecewise function as in eq.6.6,

$$\nu = \begin{cases} \frac{M(i,j)-t}{M(i,j)} & if \quad M(i,j) \geq t \quad and \quad \frac{M(i,j)-t}{M(i,j)} \geq v_1 \\ v_1 & if \quad M(i,j) \geq t \quad and \quad \frac{M(i,j)-t}{M(i,j)} < v_1 \\ v_2 & if \quad 2 < M(i,j) < t \quad and \quad \frac{M(i,j)}{t} \geq v_2 \\ \frac{M(i,j)}{t} & if \quad 2 < M(i,j) < t \quad and \quad \frac{M(i,j)}{t} < v_2 \\ 0 & if \quad 0 < M(i,j) < 2 \end{cases} \tag{6.6}$$

For a digital image $s(i,j)$, $M(i,j)$ is the average gradient magnitude of each pixel in eight directions. The parameter t is the optimal gradient threshold of image edge obtained using the improved Otsu Algorithm [149]. v_1 is the threshold of adaptive fractional differential order of image edge, and v_2 is the threshold of adaptive fractional differential order of weak texture.

Parameters v_1 and v_2 are defined in eq.6.7,

$$\begin{aligned} v_1 &= \frac{M_{ed}-M_{avg}}{M_{ed}} \\ v_2 &= \frac{M_{avg}-M_{tex}}{M_{avg}} \end{aligned} \tag{6.7}$$

The parameter M_{avg} is the average gradient of the original image, M_{ed} and M_{tex} are the average gradients of edge pixels and texture pixels respectively, segmented by improved Otsu algorithm.

The variation of gradient magnitude near edges are relatively high. So for pixels, if M(i,j) is larger than the optimal threshold t, then those pixels can be regarded as edges. A larger gradient $M(i,j)$ yields a larger ν and thus can achieve better edge enhancement. The variation of gradient magnitude in weak texture regions are relatively low and the variation of gradient magnitude in smooth areas are nearly zero. A smaller gradient $M(i,j)$ yields a smaller ν and thus more weak textures can be preserved. In a similar way, adaptive orders are estimated for all pixels of the image. Using these orders, fractional differential masks are constructed for each pixel. These masks are then used for the enhancement of the sonar image.

The adaptive fractional differential algorithm uses an improved Otsu [150] algorithm to differentiate smooth areas, textures and edges of the image. In that algorithm, adaptive orders are obtained for each and every pixel of the image and fractional differential masks are constructed for every obtained order. Even though this method offer considerable enhancement, computation complexity is really high. As the number of pixels in sonar images is high, the number of computations will be high. The proposed method is a modified version of the method of estimation of adaptive orders in the region of interest. The modification assures reduction in the number of computations without affecting the accuracy of enhancement. The noise reduction method using fractional integral mask and the modified image adaptive enhancement technique based on fractional differential mask are jointly used.

Fractional differential masks were constructed in eight directions by using the fractional order for each pixel. A convolution of the different masks with each subsequent pixel is conducted. The entire process is computationally complex. The proposed method aims at reducing this computation complexity. In the Fig.6.2 the portion included in the dashed lines depicts the modified adaptive fractional differential algorithm. Using the piecewise function for fractional differential order, estimate the adaptive order for each pixel. After specifying the region of interest (ROI), cal-

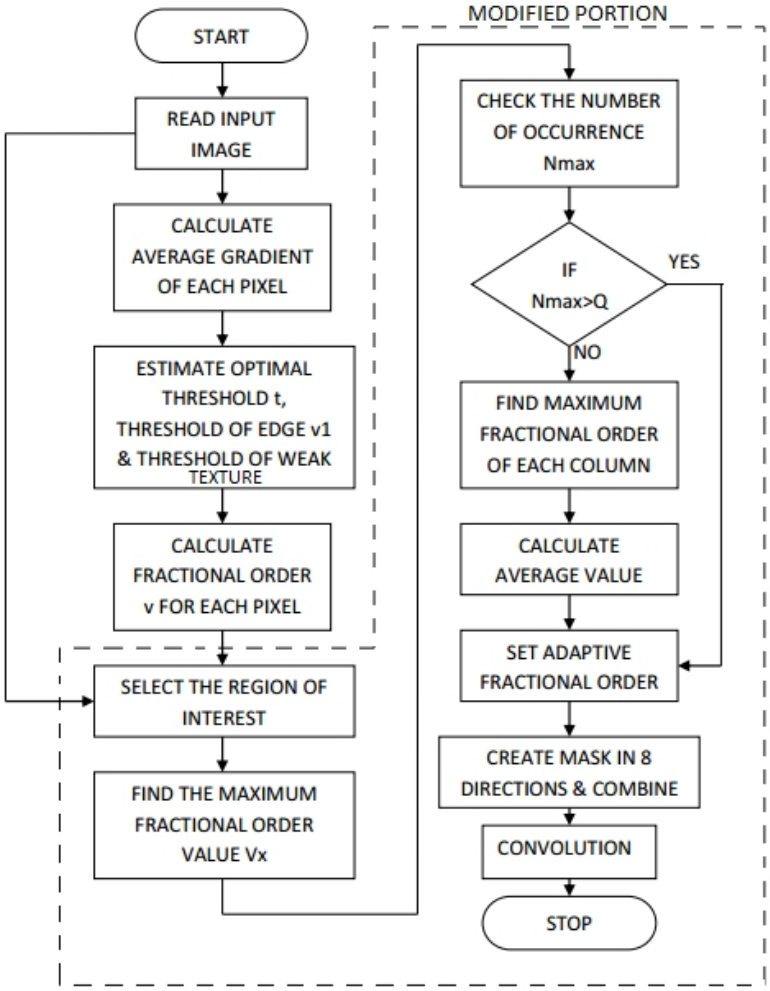

Fig. 6.2: Flowchart of the modified algorithm

culate the gradient of each pixel in the ROI and divide the image into appropriate sections. For each section, find the maximum value of fractional order. Check the number of occurrence of this maximum value in the corresponding section. If the number of occurrence is greater than a desired limit, i.e., half the number of pixels in the section, select this maximum fractional order for the construction of fractional differential mask. On the other hand, if the number of occurrence of maximum fractional order is less than the desired limit, then, find the maximum fractional order in each column of the selected section and take the mean value of maximum fractional orders obtained from each column for the construction of mask.

6.5 Image Enhancement

Gradient Magnitude for each pixel of a 180×120 sonar image is generated. From the generated result, the maximum value obtained for gradient is 31.8750. The minimum value obtained is 0 and the average gradient obtained is 4.7540. The optimal gradient threshold is estimated using improved Otsu Algorithm. The gradient threshold for which the maximum cluster variance occurs is regarded as optimal gradient threshold. The maximum cluster variance is obtained for the gradient threshold 15 for the image. It is specific for the selected image. The gradient threshold for which the maximum cluster variance occurs is regarded as optimal gradient threshold. The maximum cluster variance is obtained for the gradient threshold 15 for the image.Therefore, the Optimal gradient threshold, t is fixed as 15. After determining the value of optimal gradient threshold t, the gradients are classified into two classes. The gradient values greater than t are regarded as edges. Whereas, the gradient values smaller than t are considered as weak texture and low frequency smooth areas. The average gradient of edge pixels is $M_{ed} = 22.6714$ and the average gradient of texture pixels is $M_{tex} = 3.2307$. From eq.6.7, v_1 and v_2 are estimated as 0.7903 and 0.3204, respectively.

The adaptive order for each pixel of the whole sonar image is estimated using the piecewise function given in eq.6.6 for adaptive fractional differential order. The whole image is then divided into some non overlapping sections. From each section, maximum fractional order is found and recorded. The number of occurrence of these maximum values in corresponding sections are also recorded. According to the proposed modification, adaptive orders for each section is estimated. Fractional differential masks are constructed in 8 directions for each section using the estimated adaptive fractional differential order of corresponding section.

For a real time processing system applicable in AUVs, a fast pre-segmentation of ROI in sonar images reduces not only the amount of data for the human operator but also for the consecutive classification algorithms significantly. Convolving fractional differential mask only with the region of interest, better output images with reduced computation complexity are obtained. The region of interest extracted from the denoised image and enhanced using the proposed algorithm is shown in Fig.6.3. Percentage reduction in the computation complexity is going to be directly dependent on the ratio of the number of textured patches to the number of original patches in the selected image.

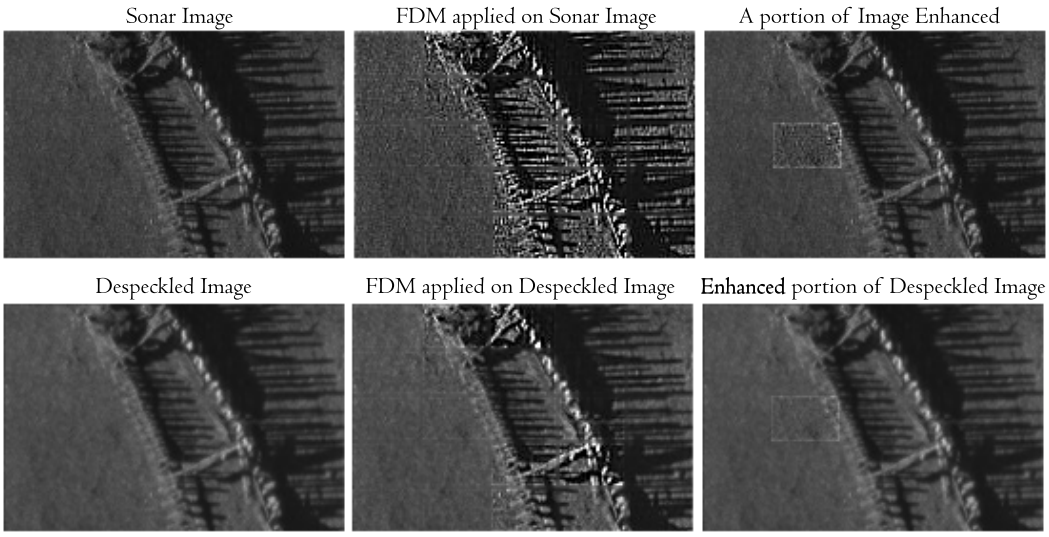

Fig. 6.3: Enhanced portion

6.6 Summary

This chapter deals with the application of a new method to enhance the denoised image. A modified algorithm for the estimation of image adaptive order proposed. Results depicts that, the proposed modification reduces computation complexity required for enhancement of sonar images.

Chapter 7

Conclusions and Future Scope

This chapter sums up the conclusions of the research work carried out. It also highlights the achievements followed by few suggestions for future work. The results presented in the thesis have been published in different international journals and conferences.

7.1 Conclusions

The despeckling of sonar images based on different speckle-scene models *vis-a-vis* signal-independent additive noise model and multiplicative noise model have been implemented and compared with the existing ones. The results and discussions part compare and analyze the different methods proposed based on the particular model selected. For comparison and analysis of the different methods proposed same sonar image has been used. Since each proposed method has its own unique speckle-scene model and denoising domain, deduction of a single conclusion becomes difficult, i.e patch based processing is good for ROI identified images,whereas the linear estimation method or non linear estimation method can be employed for SSS image processing. Depending on the application for which the denoised image will be put to use, an optimal methodology would have to be adopted. The patch based denoising helps the sonar image interpreters in defining their areas of interest to be despeckled without doing the convolution operation for the entire image pixels. The sonar image enhancement chapter emphasizes the importance of despeckling before any further processing in sonar images.

7.1.1 Additive Speckle-Scene Model

The additive noise model analysis chapter deals with the despeckling assuming a signal-independent additive noise model. The denoising was done both in the transform domain and in the spatial domain. Four sonar image estimation methods were analyzed in the chapter three of them in the transform domain and the last one in the spatial domain. In all the methods, except the multiresolution method, a blind denoising method was adopted.

In the first work a novel method for finding optimum multiresolution level based on PSNR values and visual quality, as an improvement on the classical thresholding approaches and the Bayesian thresholding method is proposed. For all the thresolding methods, the optimum multiresolution level for speckle reduction is the maximum level of decomposition possible for the image of size S to be denoised and the chosen basic wavelet function. This method fine tunes the existing denoising methods based on wavelet shrinkage in literature by optimizing the level of decomposition. The above method can be applied to other denoising architecture with proper modifications. The maximum level of decomposition possible for the particular image and the chosen basic wavelet function is determined after a series of simulations. The denoising performance is further improved by choosing the optimum wavelet shrinkage rule for the image.

Next an efficient patch based and block based image denoising algorithms, where the noisy image patches are represented using Principal Components and Singular Values is implemented. This work has presented a framework for denoising by learning a suitable basis to represent each image patch i.e, an image adaptive basis is adopted. The local basis functions are determined adaptively from the local image patches as opposed to being fixed for the entire image as in wavelet based technique and then being applied adaptively to local image patches. The denoising results emphasized the strengths of this new decomposition approach for sonar images which are sparse and the details are of high frequency.

The third work which is computationally efficient version of the second work, a blind denoising of sonar image based on a proposed naive homogeneity index is employed. The noisy patches are selectively processed which increases the computational efficiency. The assessment of the filters is done on a real sonar data by means of visual inspection and quantitative measures. The performance figures obtained by means of simulations reveal that the method provides superior performance in com-

parison to the other speckle reducing filters in terms of smoothing uniform regions and preserving edges and features. Besides, the method can significantly reduce the speckle while preserving the resolution of the original image.

In the final work which is done in the spatial domain, a Kalman filter based method for sonar image estimation is employed. The homomorphic approach is applied on the reflectivity domain relation to obtain the observation model for the Kalman filter estimation proposed. The improvement obtained over existing filters is demonstrated with real examples. The effectiveness of the techniques encourages the possibility of using the approach in a number of sonar applications. Also, cleaner images suggest potential improvements for classification and recognition.

7.1.2 Multiplicative Speckle-Scene Model

In multiplicative noise model analysis chapter a multiplicative speckle-scene model is used for the despeckling. The results of the despeckling method is compared with the existing methods in visual methods and in numerical way by using different assessment methods. Three methods using the above said model is analyzed, one in the transform domain and the other two in the spatial domain.

The traditional sonar image filtering method can only remove one kind of noise, the speckle noise and the details of the image are blurred in various degrees. Mixed noise removal from sonar images is a challenging task. In the first method of the chapter, a novel algorithm for mixed additive Gaussian and multiplicative speckle removal is done by exploiting image local sparsity and nonlocal similarity in probability distribution respectively. The performance can be further enhanced by going for patch size adaptation.

In the second method described in the chapter, the popular Riemann-Liouville definition of fractional calculus is used for the construction of eight directional integral masks and a high frequency filtering using the masks is done. The denoising algorithm can be applied on different sonar images affected with speckle noise. The results of the experiments prove that, noise removal using Fractional integral mask is better than traditional despeckling method. The mask extraction is possible for lower fractional orders and the application of the denoising filter only on to the speckle affected class of sonar image patches makes the algorithm computationally effective.

The unscented Kalman filter estimation for image restoration described in the

final part of the chapter exploits the independence in the speckle characteristics of each scan lines of the side scan imaging technology. The filter provides an efficient recursive means to estimate the state of a process, in a way that minimizes the mean of the squared error. On to the observation model of the side scan sonar image, one-dimensional UKF is applied considering each row as one-dimensional signal and blind denoising is done. The improvement obtained over existing filters is demonstrated with real examples.

7.2 Major Contributions

A detailed analysis of the literature available for despeckling of radar and sonar images has been carried out. Literature Review brought out the various algorithms based on signal dependent and independent, additive and multiplicative noise models for speckle reduction. In the work carried out, signal-independent additive noise models and multiplicative noise models were considered. A comparative study has been carried out with signal dependent model studies available in the literature. The blind and non blind denoising indexes to quantify the despeckling capability of the methods were reviewed. Different noise level estimation algorithms were reviewed and were used in the blind denoising of sonar images.

A comparison of all the methods developed based on a particular speckle scene-model is carried out at the summary portion of the working chapters. Application of a data adaptive and non data adaptive transforms for sonar image despeckling is explored. Another method like linear and non linear estimation methods were introduced for sonar image estimation in spatial domain. A fractional integral and differential mask based methods were applied for sonar image denoising and enhancement respectively.

In the presence of signal-dependent noise, the with-reference indexes were strongly influenced by the average signal level of the ground truth, unlike the case of additive signal-independent noise. For all the methods developed based on the signal-independent additive noise model, a homomorphic approach is used to obtain the additive model from the multiplicative model. This helps in the comparison of the methods based on selected model. The result of PCA transform methods' effectiveness is slightly lower compared to SVD denoising as SVD eliminates noise components associated with both the sensors and the pings. The patch based filter outperformed the conventional and non conventional speckle reducing filters in terms

of ENL and SSI. The one step pixel prediction method uses 1D Kalman estimation effectively in estimating the row pixel values and thereby avoiding the complexity of the estimation in 2D. The log transformation performed in the homomorphic approach to obtain the signal-independent additive noise model leads to very high values of ENL and SMPI compared to the other existing signal-dependent noise models methods in literature.

The non-homomorphic approach avoids the occurrance of undesired bias effects in the methods using the multiplicative noise model. In the mixed noise removal method, the processing of local and non local patches effectively removes the additive Gaussian and multiplicative noises. While using Fractional Integral Mask denoising method, the reduction in size of the mask ensures computational reduction without much performance degradation.

An immediate and subjective approach for quality assessment is represented by visual inspection of filtered images. Visual inspection permits detection of the main human-visible features that characterize the behavior of a despeckling filter. Such features include edge preservation capability, degree of blur, point target preservation, as well as structural artifacts which are hardly detected by objective and direct measurements. The skill of the sonar interpreter is often unattainable by computers. A visual comparison of various proposed methods among themselves and with existing methods is performed for the choice of sonar image interpreters. Since purely visual interpretation of sonar image is subjective, qualitative, and time consuming, quantitative assessments is also made for the same.

7.3 Suggestions for Future Work

The following are some of the prospects for future work: Thesis work deals mainly with the analysis of despeckling methods in transform and spatial domain for the two different speckle-scene model, the signal-independent additive noise model and the multiplicative noise model. The signal-dependent additive and multiplicative noise models can also be explored as future work. With the growing realization that the fixed basis such as wavelet is inappropriate for handling images, efforts have been made towards building the locally or globally adaptive basis for image sparse representations. Among that the thesis work deals with the locally adaptive basis. Globally adaptive basis methods can be analyzed. In the block adaptive patch based denoising, creating blocks of similar patches rather than adjacent patches as taken in

the algorithm can give good improvement on a statistical basis. Also the adaptation of the PCA and SVD for the selected similar patches or having them applied in a non local means filtered data, the despeckling effects can be better. Order adaptive fractional order mask based denoising can be employed to have further improved performance.

7.4 Summary

This chapter brings out the highlights of the work carried out, the general inferences gathered along with enlisting the scope and direction for future work in this area.

References

[1] P. X.F.Ye, Z.H.Zhang and H.L.Guan, "Sonar image segmentation based on gmrf and level-set models," *Ocean Eng.*, vol. 37, no. 10, pp. 891–901, Jul. 2010.

[2] P.W.Flemming., "Side-scan sonar: A practical guide," *Int. Hydrogr. Rev.*, vol. 1, no. 1, pp. 65–92, Jan. 1976.

[3] R. A.Lopes and E.Nezry, "Adaptive speckle filters and scene heterogeneity," *IEEE Trans. Geosci. Remote Sensing*, vol. 28, no. 6, pp. 992–1000, Nov. 1990.

[4] R. A.Lopes, E.Nezry and H.Laur, "Maximum a posteriori speckle filtering and first order texture models in sar images," *In Proc. IEEE Int. Geoscience and Remote Sensing Symp.(IGARSS)*, pp. 2409–2412, Sep. 1990.

[5] S. W.A.Barnhardt, J.T.Kelley and D.F.Belknap, "Mapping the gulf of maine with side-scan sonar: A new bottom-type classification for complex seafloors," *J. Coastal Res.*, vol. 14, no. 2, pp. 646–659, 1998.

[6] R.J.Urick, "Principles of underwater sound," New York: McGraw- Hill, 1975.

[7] C.Mazel, "Side scan sonar record interpretation," *Klein Assoc., Inc.*, Jun. 1985.

[8] X. Lurton, "An introduction to underwater acoustics, principles and applications," Chichester, UK, Springer, ISBN 3-540-42967-0, 2002.

[9] Y. I.Tena Ruiz and D.M.Lane, "Improved auv navigation using side-scan sonar," *In. Proc. MTS/IEEE Int. Conf. OCEANS*, pp. 1261–1268, Oct. 2003.

[10] D.Gueriot, "Bathymetric and side scan data fusion for sea-bottom 3-d mosaicing," *In. Proc. MTS/IEEE Int. Conf. OCEANS*, pp. 1663–1668, Sep. 2000.

[11] S.-K. H. Yet-Chung Chang and C.-H. Tsai, "Sidescan sonar image processing: Correcting brightness variation and patching gaps," *Journal of Marine Science and Technology*, vol. 6, pp. 785–789, Aug. 2010.

[12] J. M.F.Doherty and F.H.Malt, "Side scan sonar object classification algorithms," pp. 417–424, Jun. 1989.

[13] M.F.Czarnecki, "An application of pattern recognition techniques to side scan sonar data," *In Pro. IEEE OCEANS*, pp. 112–119, 1985.

[14] W. F.Langner, C.Knauer and A.Ebert, "Side scan sonar image resolution and automatic object detection, classification and identification," *In Pro. IEEE OCEANS Europe*, pp. 554–557, May. 2009.

[15] N.G.Pace and H.Gao, "Swathe seabed classification," *IEEE .J. Oceanic Eng.*, vol. 2, no. 13, pp. 83–90, Apr. 1988.

[16] N. Z.Reut and M.J.P.Heaton, "Computer classification of sea beds by sonar," *Nature*, vol. 4, no. 314, pp. 426–428, Apr. 1985.

[17] P.M.Maguire and N.G.Pace, "Pattern recognition techniques for swathe seabed classf1cation," School of Physics, University of Bath, 1993.

[18] P. Blondel, "The hand book of sidescan sonar," Springer Praxis Publishing, 2009.

[19] E. Dura, "Image processing techniques for the detection and classification of man made objects in side-scan sonar images, sonar systems," *InTechOpen*, no. ISBN: 978-953-307-345-3, Sep. 2011.

[20] P. B.J.Davis and B.R.Hunt, "Modeling surface multipath effects in synthetic aperture sonar," *IEEE J. Ocean. Eng.*, vol. 34, no. 3, pp. 239–249, Jul. 2009.

[21] J.S.Bird and G.K.Mullins, "Wake removal for clear side-scan images," *OCEANS Conf., Quebec City, QC, Canada*, pp. 15–18, Sep. 2008.

[22] X. G. E.Dura, Y.Zhang and L.Carin, "Active learning for detection of mine-like objects in side-scan sonar imagery," *IEEE J. Ocean. Eng.*, vol. 30, no. 2, pp. 360–371, Apr. 2005.

[23] J.W.Goodman, "Some fundamental properties of speckle," *J. Opt. Soc. Amer.*, vol. 66, no. 11, pp. 145–150, Nov.1976.

[24] K. M.Tur and J.W.Goodman, "When is speckle multiplicative?," *Appl. Optics*, vol. 21, no. 7, p. 115711590, 1982.

[25] A. H. Frederic Maussang, Jocelyn Chanussot and M. Amate, "Mean standard deviation representation of sonar images for echo detection: Application to sas images," *IEEE Journal of Oceanic Engineering*, vol. 32, no. 4, pp. 1449–1451, Oct. 2007.

[26] S.Solbo and T.Eltoft, "A stationary wavelet-domain wiener filter for correlated speckle," *IEEE Trans. Geosci. Remote Sensing*, vol. 46, no. 4, pp. 1219–1230, Apr. 2008.

[27] F. A.Lapini, T.Bianchi and L.Alparone, "A whitening method for the despeckling of sar images affected by correlated speckle noise," *In Proc. 20th European Signal Processing Conf.(EUSIPCO)*, pp. 2487–2491, Aug. 2012.

[28] C.Burckhardt, "Speckle in ultrasound b-mode scans," *IEEE Trans. Sonics Ultrason*, vol. 25, pp. 1–6, Jan. 1978.

[29] J.A.Ogilvy, "Theory of wave scattering from random rough suifaces," Adam Higer, Bristol, 1991.

[30] P.Beckmann and A.Spizzichino, "The scattering of electromagnetic waves from rough suifaces," Macmillan, New York, 1963.

[31] J. R.F.Wagner, S. W.Smith and H.Lopez, "Statistics of speckle in ultrasound b-scans," *IEEE Trans. Sonics Ultrason*, vol. 30, no. 3, pp. 156–163, May 1983.

[32] T.K.Stanton, "Sonar estimates of seafloor microroughness," *J. Acoust Soc. Am.*, vol. 3, no. 75, pp. 806–815, 1984.

[33] C. M. D.Alexandrou and G.Haralabus, "Evaluation and verification of bottom acoustic reverberation statistics predicted by a point scattering model," *J. Acoust Soc. Am.*, vol. 3, no. 91, pp. 1403–1413, Mar. 1992.

[34] NeilC.Mitchell, "Representing backscatter fluctuations with a pdf convolution equation and its application to study backscatter variability in side-scan sonar images," *IEEE Transactions on Geoscience and Remote sensing*, vol. 33, no. 6, pp. 1328–1331, Nov. 1995.

[35] H.H.Arsenault and M.Levesque, "Combined homomorphic and local-statistics processing for restoration of images degraded by signal dependent noise," *Appl. Opt.*, vol. 23, no. 6, pp. 845–850, Mar. 1984.

[36] A.K.Jain, "Fundamentals of digital image processing," Englewood Cliffs, NJ: Prentice-Hall, 1989.

[37] A. A.Achim and P.Tsakalides, "Novel bayesian multiscale method for speckle removal in medical ultrasound images," *IEEE trans. on Medical Imaging*, vol. 20, pp. 772–783, Aug. 2001.

[38] L. H.Xie and F.T.Ulaby, "Statistical properties of logarithmically transformed speckle," *IEEE Trans. Geosci. Remote Sensing*, vol. 40, no. 3, pp. 721–727, Mar. 2002.

[39] J.S.Lee, "Digital image enhancement and noise filtering by use of local statistics," *IEEE Trans. Pattern Anal. Mach. Intell.*, vol. PAMI-2, no. 2, pp. 165–168, Mar. 1980.

[40] K. V.S.Frost, J.A.Stiles and J.C.Holtzman, "A model for radar images and its application to adaptive digital filtering of multiplicative noise," *IEEE Trans. Pattern Anal. Mach.Intell.*, vol. PAMI-4, no. 2, pp. 157–166, Mar. 1982.

[41] T. D.T.Kuan, A.A.Sawchuk and P.Chavel, "Self-complimentary antennas," *IEEE Trans. Pattern Anal. Mach. Intell.*, vol. PAMI-7, no. 2, pp. 165–177, Feb. 1985.

[42] I. P. . J.Malik, "Scale-space and edge detection using anisotropic diffusion," *IEEE Trans. On Pattern Analysis and Machine Intelligence*, vol. 12, no. 7, pp. 629–639, Jul. 1990.

[43] I. . A.N.Venetsanopoulos, "Nonlinear digital filters- principles and applications," Kluwer Academic Publishers, 1990.

[44] D.Hillery, "Iterative wiener filters for images restoration," *IEEE Transaction on SP*, vol. 39, no. 8, pp. 1892–1899, Aug. 1991.

[45] P. Issa, "Adaptative weighted alpha filter," *Proc. EUSIPCO96, Trieste, Italy*, Sep. 1996.

[46] J.S.Lee, "Speckle analysis and smoothing of synthetic aperture radar images," *Comput.Graph. and Image Process. Elsevier*, vol. 17, no. 1, pp. 24–32, Sep. 1981.

[47] J.S.Lee, "Speckle suppression and analysis for synthetic aperture radar images," *Opt. Eng.*, vol. 25, no. 5, pp. 636–643, May 1986.

[48] T. D.T.Kuan, A.A.Sawchuk and P.Chavel, "Adaptive restoration of images with speckle," *IEEE Trans. Acoust.,Speech, Signal Process.*, vol. ASSP-35, no. 3, pp. 373–383, Mar. 1987.

[49] J. C. K. Yan and D. Hatzinakos, "Signal-dependent film grain noise removal and generation based on higher- order statistics generation," *In Proc. of IEEE Signal Processing workshop on Higher Order Statistics*, Jul. 1997.

[50] I.Daubechies, "Orthonormal bases of compactly supported wavelets," *Commun. Pure Appl. Math.*, vol. 41, no. 7, pp. 909–996, Oct. 1988.

[51] G. B. B. Samuel Foucher and J.-M. Boucher, "Multiscale map filtering of sar images," *IEEE Transactions on Image Processing*, vol. 10, no. 1, Jan. 2001.

[52] F. B.Aiazzi, L.Alparone and A.Lapini, "An experimental setup for multiresolution despeckling of cosmo-skymed image products," *In Proc. SPIE SAR Image Analysis, Modeling, and Techniques XII*, vol. 8536, pp. 603–606, Nov. 2012.

[53] R. P.Meer and K.Cho, "Multiresolution adaptive image smoothing," *Graph. Models Image Process.*, vol. 56, no. 2, pp. 140–148, Mar. 1994.

[54] O. B.-H. Serge Karabchevsky, David Kahana and H. Guterman, "Fpga-based adaptive speckle suppression filter for underwater imaging sonar," *IEEE Journal of Oceanic Engineering*, vol. 36, no. 4, pp. 646–657, Oct. 2011.

[55] D. L.Donoho, "Denoising via soft thresholding," *IEEE Transactions on Information Theory*, pp. 613–627, May. 1995.

[56] B. S.Grace Chang and M. Vetterli, "Spatially adaptive wavelet thresholding with context modeling for image denoising," *IEEE Trans. Image Processing*, vol. 9, no. 9, pp. 1522–1531, Jul. 1998.

[57] D.L.Donoho and I.M.Johnstone, "Adapting to unknown smoothness via wavelet shrinkage," *Journal American Statistical.Association*, vol. 90, no. 432, pp. 1200–1224, Dec. 1995.

[58] T. F.Abramovich and B.W.Silverman, "Wavelet thresholding via a bayesian approach," *J. R. Statist.Soc., ser. B, Pub. Wiley*, vol. 60, no. part 4, pp. 725–749, 1998.

[59] L.Gagnon and A.Jouan, "Speckle filtering of sar images: A comparative study between complex-wavelet-based and standard filters," *In Proc. SPIE, Wavelet Applications in Signal and Image processing V*, vol. 3169, pp. 80–91, 1997.

[60] P. E.Hervet, R.Fjortoft and A.Lopes, "Comparison of wavelet-based and statistical speckle filters," *In Proc. SPIESAR Image Analysis, Modelling, and Techniques III, F. Posa, Ed.*, vol. 3497, pp. 43–54, Nov. 1998.

[61] B. M.Simard, G.DeGrandi and G.B.Benie, "Analysis of speckle noise contribution on wavelet decomposition of sar images," *IEEE Trans. Geosci. Remote Sensing*, vol. 36, no. 6, pp. 1953–1962, Nov. 1998.

[62] J.R.Sveinsson and J.A.Benediktsson, "Almost translation invariant wavelet transformations for speckle reduction of sar images," *IEEE Trans. Geosci. Remote Sensing*, vol. 41, no. 510, pp. 2404–2408, Oct. 2003.

[63] B.Vidakovic, "Nonlinear wavelet shrinkage with bayes rules and bayes factors," *J. Amer. Statist. Assoc.*, vol. 93, no. 441, pp. 173–179, Mar. 1998.

[64] S.M.Kay, "Fundamentals of statistical processing," Englewood Cliffs, NJ: Prentice-Hall, 1993.

[65] P. C. Fabien Chaillan, Christophe Fraschini and M. Amate, "Multiresolution analysis of sas images," *In Proc IEEE OCEANS, Europe*, pp. 1127–1132, Jun. 2005.

[66] H. Yang and Y. Wang, "An improved method of wavelets basis image denoising using besov norm regularization," *Fourth International Conference on Image and Graphics*, pp. 81–85, Aug. 2007.

[67] F. T.Bianchi and L.Alparone, "Segmentation-based map despeckling of sar images in the undecimated wavelet domain," *IEEE Trans. Geosci. Remote Sensing*, vol. 46, no. 9, pp. 2728–2742, Jul. 2008.

[68] J.S.Lee, "Digital image smoothing and the sigma filter," *Comput. Vis. Graph. Image Process.*, vol. 24, no. 2, pp. 255–269, Nov. 1983.

[69] J.S.Lee, "A simple speckle smoothing algorithm for synthetic aperture radar images," *IEEE Trans. Syst., Man, Cybern.*, vol. SMC-13, no. 1, pp. 85–89, Jan. 1983.

[70] S. L.Alparone and A.Garzelli, "A hybrid sigma filter for unbiased and edge-preserving speckle reduction," *In Proc.IEEE Int. Geoscience and Remote Sensing Symp. (IGARSS)*, vol. 2, pp. 1409–1411, Mar. 1995.

[71] J. J.S.Lee and A.J.Chen, "Improved sigma filter for speckle filtering of sar imagery," *IEEE Trans. Geosci. Remote Sensing*, vol. 47, no. 1, pp. 202–213, Jan. 2009.

[72] G.S.Sudha and R.Sukanesh, "Speckle noise reduction in ultrasound images using context-based adaptive wavelet thresholding," *IETE J.Res.*, vol. 55, pp. 135–143, 2009.

[73] D. I. Ioana Firoiu, Corina Nafornita and A. Isar, "Bayesian hyperanalytic denoising of sonar images," *IEEE Geoscience and Remote Sensing Letters*, vol. 8, no. 6, pp. 1065–1069, Nov. 2011.

[74] C. Stolojescu-Crisan and A. Isar, "Denoising and inpainting sonar images," *In Proc. IEEE Telecommunication and Signal Processing (TSP)*, Jul. 2015.

[75] C. Stolojescu-Crisan and C. Botoca, "Sonar images restoration in the wavelets domain," *In Proc. of IEEE International Symposium on Electronics and Telecommunications (ISETC)*, Dec. 2016.

[76] T.R.Crimmins, "Geometric filter for speckle reduction," *Appl. Opt.*, vol. 24, no. 10, pp. 1438–1443, May. 1985.

[77] L. B.Aiazzi and S.Baronti, "Multiresolution local-statistics speckle filtering based on a ratio laplacian pyramid," *IEEE Trans.Geosci. Remote Sensing*, vol. 36, no. 5, pp. 1466–1476, Sep. 1998.

[78] R. A.Lopes, E.Nezry and H.Laur, "Structure detection and statistical adaptive speckle filtering in sar images," *Int. J.Remote Sensing*, vol. 14, no. 9, pp. 1735–1758, Jun. 1993.

[79] R.G.White, "A simulated annealing algorithm for sar and mti image cross section estimation," *In Proc. SPIE SAR Data Processing for Remote Sensing*, vol. 2316, no. 137, pp. 339–360, Dec. 1994.

[80] I.McConnell and C.Oliver, "Comparison of annealing and iterated filters for speckle reduction in sar," *In Proc. SPIE Microwave Sensing and Synthetic Aperture Radar*, vol. 2958, no. 74, pp. 74–85, Dec. 1996.

[81] C.Tomasi and R.Manduchi, "Bilateral filtering for gray and color images," *In Proc. 6th Int. Conf. Computer Vision (ICCV)*, pp. 839–846, Jan. 1998.

[82] Q. W.G.Zhang and C.S.Yang, "Improved bilateral filtering for sar image despeckling," *Electron.Lett.*, vol. 47, no. 4, pp. 286–288, Feb. 2011.

[83] P. G.T. Li, C.L.Wang and W. Yu, "Sar image despeckling using a space-domain filter with alterable window," *IEEE Geosci. Remote Sensing Lett.*, vol. 10, no. 2, pp. 263–267, Mar. 2013.

[84] Y.Yongjian and S.T.Acton, "Speckle reducing anisotropic diffusion," *IEEE Transactions on Image Processing*, vol. 11, pp. 1260–1270, Dec. 2002.

[85] S. H.Krim, D.Tucker and D.Donoho, "On denoising and best signal representation," *IEEE Trans.on Information Theory*, vol. 45, no. 7, pp. 2225–2237, Nov. 1999.

[86] C. P.Coupe, P.Hellier and C.Barillot, "Bayesian non-local means-based speckle filtering," *In Proc. 5th IEEE Int. Symp. Biomedical Imaging: From Nano to Macro*, pp. 1291–1294, May 2008.

[87] Y.Yu and S.T.Acton, "Speckle reducing anisotropic diffusion," *IEEE Trans. Image Process.*, vol. 11, no. 11, pp. 1260–1270, Nov. 2002.

[88] S. L.I.Rudin and E.Fatemi, "Nonlinear total variation based noise removal algorithms," *Physica D*, vol. 60, no. 14, pp. 259–268, Nov. 1992.

[89] P. L.I.Rudin and S.Osher, "Multiplicative denoising and deblurring: Theory and algorithms," *In Geometric Level Set Methods in Imaging, Vision, and Graphics. New York: Springer- Verlag*, pp. 103–119, 2003.

[90] G.Aubert and J.Aujol, "A variational approach to removing multiplicative noise," *SIAM J. Appl. Math.*, vol. 68, no. 4, pp. 925–946, Dec. 2008.

[91] J.Shi and S.Osher, "A nonlinear inverse scale space method for a convex multiplicative noise model," *SIAM J. Imaging Sci.*, vol. 1, no. 3, pp. 294–321, Sept. 2008.

[92] S.G.Mallat, "A theory for multiresolution signal decomposition: the wavelet representation," *IEEE Transactions on Pattern Analysis and Machine Intelligence*, vol. 41, no. 11, pp. 674–693, Jul. 1989.

[93] M.R.Azimi-Sadjadi and S.Bannour, "Two-dimensional adaptive block kalman filtering of sar imagery," *IEEE Trans. Geosci. And Remote Sensing*, vol. 29, pp. 742–753, Sep. 1991.

[94] R.E.Kalman, "A new approach to linear filtering and prediction problems," *Trans. ASME, J. Basic Eng.*, vol. 82 Series D, no. 1, pp. 35–46, 1960.

[95] S.J.Julier and J.K.Uhlmann, "A new extension of the kalman filter to nonlinear systems," *In Proc.of SPIE3068*, vol. 6, no. 182, Jul. 1997.

[96] S.J.Julier and J.K.Uhlmann, "Unscented filtering and nonlinear estimation," *Invited Paper, Proceedings of the IEEE*, vol. 92, no. 3, pp. 401–422, Mar. 2004.

[97] A. S.Subrahmanyam and R.Aravind, "Unscented kalman filter for image estimation in film grain noise," *IEEE ICIP*, Oct. 2007.

[98] D.L.Donoho, "Compressed sensing," *IEEE Trans. Inform. Theory*, vol. 52, no. 4, pp. 1289–1306, Apr. 2006.

[99] S.Foucher, "Sar image filtering via learned dictionaries and sparse representations," *In Proc. IEEE Int. Geoscience and Remote Sensing Symp. (IGARSS)*, vol. 1, pp. 229–232, Jul. 2008.

[100] M.Yang and G.Zhang, "Sar image despeckling using over complete dictionary," *Electron.Lett.*, vol. 48, no. 10, pp. 596–597, May 2012.

[101] X. Y.Hao and J.Xu, "Multiplicative noise removal via sparse and redundant representations over learned dictionaries and total variation," *Signal Process.*, vol. 92, no. 6, pp. 1536–1549, Jun. 2012.

[102] L. C.A.Deledalle and F.Tupin, "Iterative weighted maximum likelihood denoising with probabilistic patch based weights," *IEEE Trans. Image Process.*, vol. 18, no. 12, pp. 2661–2672, Dec. 2009.

[103] C. S.Parrilli, M.Poderico and L.Verdoliva, "A nonlocal sar image denoising algorithm based on llmmse wavelet shrinkage," *IEEE Trans. Geosci. Remote Sensing*, vol. 50, no. 2, pp. 606–616, Feb. 2012.

[104] B. A.Buades and J.M.Morel, "A non-local algorithm for image denoising," *In Proc. IEEE Conf. Computer Vision and Pattern Recognition (ICCVPR)*, vol. 2, pp. 60–65, 2005.

[105] V. K.Dabov, A.Foi and K.Egiazarian, "Image denoising by sparse 3-d transform-domain collaborative filtering," *IEEE Trans. Image Process.*, vol. 16, no. 8, pp. 2080–2095, Aug. 2007.

[106] T.Teuber and A.Lang, "A new similarity measure for nonlocal filtering in the presence of multiplicative noise," *Comput. Stat.Data Anal.*, vol. 56, no. 12, pp. 3821–3842, Dec. 2012.

[107] J. C.Kervrann and P.Coupe, "Bayesian nonlocal means filter, image redundancy and adaptive dictionaries for noise removal," *In Proc. 1st Int. Conf. on Scale Spaceand Variational Methods in Computer Vision (SSVM)*, pp. 520–532, May. 2007.

[108] Y. H.Zhong and L.Jiao, "Sar image despeckling using bayesian non-local means filter with sigma pre selection," *IEEE Geosci. Remote Sensing Lett.*, vol. 8, no. 4, pp. 809–813, Jul. 2011.

[109] G. D.Gragnaniello and L.Verdoliva, "Classification based non local sar despeckling," *In Proc. Tyrrhenian Workshopon Advances in Radar and Remote Sensing*, pp. 121–125, 2012.

[110] L. J. Cong Weihua, "An improved three-dimensional block matching image denoise algorithm and its application in a 3d imaging sonar," *Ocean Acoustics COA IEEE/OES*, Aug. 2016.

[111] M.Walessa and M.Datcu, "Side scan sonar object classification algoritanhms," *IEEE Trans. Geosci. RemoteSensing*, vol. 38, no. 5, pp. 2258–2269, Sep. 2000.

[112] E. A.Achim and J.Zerubia, "Sar image filtering based on the heavy-tailed rayleigh model," *IEEE Trans. Image Process.*, vol. 15, no. 9, pp. 2686–2693, Sep. 2006.

[113] C.Oliver and S.Quegan, "Understanding synthetic aperture radar images," *Boston, MA: Artech House*, 1998.

[114] J.C.Curlander and R.N.McDonough, "Synthetic aperture radar: Systems and signal processing," John Wiley and Sons, Inc., 1991.

[115] C.Oliver and S.Quegan, "Understanding synthetic aperture radar images. the scitech radar and defense series," *SciTech Publ.*, 2004.

[116] Shen and Z.G.Xia, "A comprehensive evaluation of filters for radar speckle suppression," *Geoscience and Remote SensingSymposium, 1996 IEEE International Proceedings, IGARSS'96*, vol. 3, pp. 1559–1561, May 1996.

[117] Shamsoddini and J.C.Trinder, "Image texture preservation in speckle noise suppression," *ISPRS TC VII Symposiu 100Years ISPR, W. Wagner and B. Szkely (eds.), Vol. XXXVIII, Part 7A,Vienna, Austria, July*, pp. 239–244, 2010.

[118] R.Touzi, "A review of speckle filtering in the context of estimation theory," *IEEE Trans. Geosci. Remote Sensing*, vol. 40, no. 11, pp. 2392–2404, Nov. 2002.

[119] P. C.Wille., "Sound images of the ocean in research and monitoring," Springer, 2005.

[120] a. J. Y.Xu, J.B.Weaver, "Wavelet transform domain filters: a spatially selective noise filtration technique," *IEEE Trans. Image Proc.*, vol. 3, no. 6, pp. 747–758, Nov. 1994.

[121] A. K. Amit Saurabh and U.Anitha, "Performance analysis of various wavelet thresholding techniques for despeckiling of sonar images," *In Proc. IEEE International Conference on Signal Processing, Communication and Networking (ICSCN)*, Mar. 2015.

[122] S.Theodoridis and K.Koutroumbas, "Pattern recognition," p. ch. 6, San Diego, CA: Academic, 2003.

[123] B. S.Grace Chang and M. Vetterli, "Spatially adaptive wavelet thresholding with context modeling for image denoising," *IEEE Trans. Image Processing*, vol. 9, no. 9, p. 15221531, 2000.

[124] D.D.Muresan and T.W.Parks, "Adaptive principal components and image denoising," *in Proc. Int. Conf. Image Process.*, vol. 1, pp. 101–104, Nov. 2003.

[125] W. C. Yanmin He, Tao Gan and H. Wang, "Adaptive denoising by singular value decomposition," *IEEE signal processing letters*, vol. 18, no. 4, pp. 215–218, pr. A2011.

[126] M. T. Xinhao Liu and M. Okutomi, "Single-image noise level estimation for blind denoising," *IEEE Transactions on Image Processing*, vol. 22, no. 12, pp. 5226–5237, Dec. 2013.

[127] C.M.Bishop, "Pattern recognition and machine learning," New York, NY, USA, Springer-Verlag, 2006.

[128] J.Lee and K.Hoppel, "Noise modeling and estimation of remotely sensed images," *In Proc. 12th Can. Symp. IGARSS*, pp. 1005–1008, Jul. 1989.

[129] J. S.Pyatykh and L.Zheng, "Image noise level estimation by principal component analysis," *IEEE Trans. Image Process.*, vol. 22, no. 2, pp. 687–699, Feb. 2013.

[130] X.Zhu and P.Milanfar, "Automatic parameter selection for denoising algorithms using a no-reference measure of image content," *IEEE Trans. Image Process.*, vol. 19, no. 12, pp. 3116–3132, Dec. 2010.

[131] K.B.Petersen and M.S.Pedersen, "The matrix cookbook," *Tech. Univ. Denmark, Kongens Lyngby*, Nov. 2005.

[132] G. J.Bigun and J.Wiklund, "Multidimensional orientation estimation with applications to texture analysis and optical flow," *IEEE Trans. Pattern Anal. Mach. Intell.*, vol. 13, no. 8, pp. 775–790, Aug. 1991.

[133] N. K.Kim and N.Intrator, "Mosaicing of acoustic camera images," *Radar, Sonar and Navigation, IEEE Proceedings*, vol. 152, pp. 263–270, Aug. 2005.

[134] G. Welch and G. Bishop, "An introduction to the kalman filter," 2004.

[135] R.E.Kalman and R.S.Bucy, "New results in linear filtering and prediction theory," *Trans. ASME, J. Basic Eng.*, vol. 83 Series D, no. 1, pp. 95–108, 1961.

[136] P. C.Kervrann and J.Boulanger, "Bayesian non-local means image redundancy and adaptive estimation for image representation and applications," *In SIAM Conf. on Imaging Science, San Diego, CA*, Jul. 2008.

[137] D. Cafagna, "Fractional calculus: A mathematical tool from the past for present engineers," *IEEE Industrial Electronics Magazine*, vol. 1, pp. 1932–4529, Summer, 2007.

[138] X. Y. Yi-fei Pu, Ji-Liu Zhou, "Fractional differential mask: A fractional differential-based approach for multiscale texture enhancement," *IEEE Transactions on Image Processing*, vol. 19, no. 2, pp. 491–511, Feb. 2010.

[139] M. D. Ortigueira, "Riesz potential operators and inverses via fractional centred derivatives," *International Journal of Mathematics and Mathematical Sciences*, pp. 1–12, Jan. 2006.

[140] Y.-f. P. Jinrong HU and J.-L. Zhou, "A novel image denoising algorithm based on riemann-liouville definition," *Journal of computers*, vol. 6, no. 7, pp. 1332–1338, Jul. 2011.

[141] Y.-f. P. YI zhang and J.-L. Zhou, "Construction of fractional differential masks based on riemann-liouville definition," *Journal of Computational Information Systems*, vol. 6, no. 10, pp. 3191–3199, Oct. 2010.

[142] J. W. Woods and V. K. Ingle, "Kalman filtering in two dimensions: Further results," *IEEE Transactions on Acoustics, Speech, and Signal Processing, ASSP*, vol. 29, no. 2, pp. 188–197, Apr. 1981.

[143] E. K.Reif, S.Gunther and R.Unbehauen, "Stochastic stability of the discrete-time extended kalman filter," *IEEE Trans.Automatic Control*, vol. 44, no. 4, Apr. 1999.

[144] S.J.Julier and J.K.Uhlmann, "A general method for approximating nonlinear transformations of probability distributions," *Technical report, RRG, Dept. of Engineering Science, University of Oxford*, Nov. 1996.

[145] F. C. C. M. Jocelyn Chanussot and A. Ctet, "Scalar image processing filters for speckle reduction on synthetic aperture sonar images," *In Proc. MTS/IEEE OCEANS*, pp. 2294–2301, Oct. 2002.

[146] S. Das and I. Pan, "Fractional order signal processing," Springer Briefs in Applied Science and Tehnology, 2012.

[147] I. Petras, "Fractional-order nonlinear systems," Springer Nonlinear Physical Science, 2011.

[148] B. Li and W. Xie, "Adaptive fractional differential algorithm based on otsu standard," *IEEE Proc. 26th Int. Conf. CCDC*, pp. 2020–2025, Jul. 2014.

[149] H.J.Vala and A. Baxi, "A review on otsu image segmentation algorithm," *International Journal of Advanced Research in Computer Engineering & Technology*, pp. 387–389, Feb. 2013.

[150] D. Z. Mengxing Huang, Wenjiao Yu, "An improved image segmentation algorithm based on the otsu method," *IEEE Proc. 13th ACIS Int. Conf. SNPD*, pp. 135–139, Aug. 2012.

Publications

1. Rithu James & Supriya M H, "Despeckling of Sonar Images Based on a Naive Homogeneity Index", OCEANS 2016 MTS/IEEE Monterey, IEEE, Pages 19-23 Sept. 2016.

2. Rithu James & Supriya M H, "Blind Estimation of Single Look Side Scan Sonar Image from the Observation Model" , Elsevier Procedia Computer Science Volume 93, 2016, Pages 336-343 Sept. 2016.

3. Rithu James & Supriya M H, "Spatial Resolution Enhancement of Sonar Images Using One Step Pixel Prediction", International Conference on Control Communication Computing India (ICCC), 2015, IEEE, Pages 19-21 Nov. 2015.

4. Rithu James, Anita Mariam Jolly, Anjali C & Dimple Michael, "Image Denoising using Adaptive PCA and SVD", Fifth International Conference on Advances in Computing and Communications (ICACC), 2015 IEEE, Pages 2-4 Sept. 2015.

5. Rithu James & Supriya M H, "Sonar Image Denoising using Adaptive Processing of Local Patches", in International Symposium on Ocean Electronics (SYMPOL 2015),IEEE,Pages 18-20 November 2015.

6. Rithu James & Supriya M H, "Speckle Reduction Based on Optimum Multi resolution Level", International Journal of Electronics and Communication Engineering (IJECE) ISSN: 2278-991x Vol. 3, Issue 1, pp. 1-8, Jan 2014.

7. Rithu James & Supriya M H, "Computationally Efficient Methods for Sonar Image Denoising using Fractional Mask", Image Process. Int. J. (IJIP) vol.10, Iss.5, pp. 239-258, Sep 2016.

8. Rithu James & Supriya M H, "Sonar Image Enhancement using Fractional Masks" International Symposium on Ocean Electronics, SYMPOL 2017.

9. Rithu James & Supriya M H, "Removal of Multiple Noises in Sonar Images by Processing of Patches", Sadhana Indian Academy of Sciences, Springer (in review-manuscript ID SADH-S-17-00306).

Subject Index